

**DEVELOPMENT OF TANDEM MASS SPECTROMETRIC
METHODS FOR CHARACTERIZING ASPHALTENES AND
DIFFERENTIATING SMALL ORGANIC ISOMERS**

by

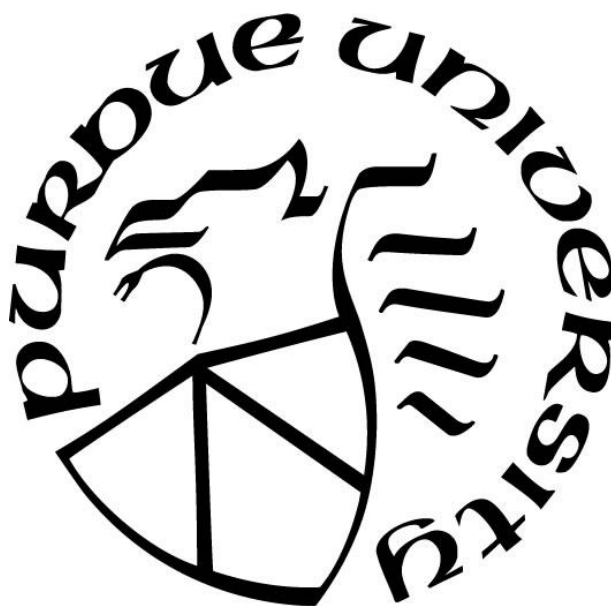
Xueming Dong

A Dissertation

Submitted to the Faculty of Purdue University

In Partial Fulfillment of the Requirements for the degree of

Doctor of Philosophy



Department of Chemistry

West Lafayette, Indiana

May 2019

THE PURDUE UNIVERSITY GRADUATE SCHOOL
STATEMENT OF COMMITTEE APPROVAL

Dr. Hilikka I. Kenttämäaa, Chair

Department of Chemistry

Dr. Chengde Mao

Department of Chemistry

Dr. Garth Simpson

Department of Chemistry

Dr. Gozdem Kilaz

School of Engineering Technology

Approved by:

Dr. Christine Hrycyna

Head of the Graduate Program

*To my parents and my friends,
This could not have been achieved without your emotional and intellectual support.*

ACKNOWLEDGMENTS

I would like to express my most sincere gratitude to my advisor, Frank Brown Distinguished Professor Hilkka I. Kenttämäa. Her unparalleled scientific insights, academic integrity, and dedication for comprehensive training of graduate students were of crucial importance for my success. My skills in advanced analytical chemistry, mass spectrometry, critical thinking, and communication tremendously improved thanks to her guidance. I would like to express my heartfelt appreciation to her for creating the wonderful group dynamic and laboratory environment, and I wish that I could always learn more from her.

In addition, I would like to express my appreciation to the members and collaborators from the Kenttämäa group for their support and help. I would like to thank Dr. Huaming Sheng, Dr. James Riedeman, Dr. Weijuan Tang, Dr. Ashley Wittrig, and Dr. Chunfen Jin for their help and mentorship. I would also like to express my gratitude to Dr. Jinshan Gao, Dr. Joann Max, Dr. Mckay Easton, Yuyang Zhang, Xin Ma, Mark Romanczyk, Edouard Niyonsaba, and Jeremy Manheim for bringing joy into my graduate experience and for offering critical insights to my research. During my research, I was also privileged to work with brilliant researchers from various fields: Dr. Ryan Hilger, Dr. Jeremy Holtsclaw, Dr. Rituraj Borgohain, Dr. Nathan Schultheiss, Dr. Cliff Johnston, Dr. Xin Fan, and Dr. Yishu Song. Their valuable insights and support were crucial for my research. Special thanks to Leah F. Easterling and Jacob Milton for their patience and expertise in editing both my manuscripts and this thesis. Dr. Shao Yu, Dr. Xin Lu, and Dr. Wan Li provided extremely insightful advice in statistics, machine learning, and advanced data analysis.

At last, my special thanks go to my parents and friends for their emotional support.

TABLE OF CONTENTS

TABLE OF CONTENTS.....	5
LIST OF TABLES	8
LIST OF FIGURES	9
ABSTRACT.....	15
CHAPTER 1. INTRODUCTION	16
1.1 Introduction.....	16
1.2 Thesis overview	17
1.3 References.....	19
CHAPTER 2. INSTRUMENTATION AND EXPERIMENTAL DETAILS CONCERNING HYBRID LINEAR QUADRUPOLE ION TRAP-ORBITRAP MASS SPECTROMETERS	20
2.1 Introduction.....	20
2.2 Ionization	21
2.2.1 Electrospray Ionization (ESI)	21
2.2.2 Atmospheric-Pressure Chemical Ionization (APCI)	23
2.3 Overview of the Linear Quadrupole Ion Trap (LQIT) Mass Spectrometer	25
2.4 The Atmospheric Pressure Ionization (API) Region	25
2.4.1 The Ion Optics Region.....	27
2.4.2 Ion Trap Region.....	30
2.5 Fundamental Aspects of Linear Quadrupole Ion Traps	30
2.5.1 Ion Trapping	30
2.5.2 Ion Ejection.....	35
2.5.3 Ion Detection with Electron Multipliers	38
2.6 Fundamental Aspects of Tandem Mass Spectrometry (MS/MS)	39
2.6.1 Ion Isolation.....	39
2.6.2 Collision-Activated Dissociation.....	41
2.7 Fundamental Aspects of the Orbitrap Mass Analyzer	47
2.7.1 C-Trap.....	48

2.7.2	Ion Motion in the Orbitrap.....	50
2.7.3	Ion Detection in the Orbitrap.....	51
2.7.4	Medium-Energy CAD (MCAD).....	51
2.8	References.....	53
CHAPTER 3. DEVELOPING TANDEM MASS SPECTROMETRY METHODS TO ADDRESS SAMPLING BIASES FOR DETERMINING THE RELATIVE ABUNDANCES OF SINGLE-CORE AND MULTICORE COMPOUNDS IN ASPHALTENES.....		
		57
3.1	Introduction.....	57
3.2	Materials and Methods.....	60
3.2.1	Reagents.....	60
3.2.2	Mass Spectrometry	61
3.3	Results and Discussion	62
3.3.1	Statistical Considerations for Sampling in MS/MS Analysis of Asphaltenes.....	62
3.3.2	MCAD Patterns of Molecular Ions Derived from Single-core and Multicore Model Compounds.....	64
3.3.3	MCAD Patterns Measured for Molecular Ions Derived from Mixtures of Single-core and Multicore Model Compounds.....	65
3.3.4	MCAD Patterns of Molecular Ions Derived from Asphaltenes.....	71
3.3.5	ISCAD Patterns Measured for Molecular Ions Derived from Mixtures of Single-core and Multicore Model Compounds.....	83
3.3.6	ISCAD Patterns of Molecular Ions Derived from Asphaltenes.....	86
3.4	Conclusions.....	88
3.5	References.....	90
CHAPTER 4. DETERMINATION OF AROMATIC CORE SIZES AND THE NUMBER OF CARBONS IN ALKYL CHAINS FOR ISOBARIC IONS DERIVED FROM ASPHALTENES BY USING HIGH-RESOLUTION TANDEM MASS SPECTROMETRY.....		
		94
4.1	Introduction.....	94
4.2	Materials and Methods.....	96
4.3	Results and Discussion	98

4.3.1	Conventional Methods for Analysis of an MS/MS Spectra	98
4.3.2	MCAD Fragmentation Patterns of Molecular Ions of Single-core and Multicore Model Compounds.....	100
4.3.3	Interpretation of MS Data via the Reconstructed Mass Spectrum	104
4.3.4	Investigation of Ions of m/z 400 ± 0.5 , 500 ± 0.5 , 600 ± 0.5 , and 700 ± 0.5 Derived from an Asphaltene Sample.....	108
4.4	Conclusions.....	117
4.5	References.....	119
CHAPTER 5. COMPARING ENERGY-RESOLVED MEDIUM-ENERGY COLLISION-ACTIVATED DISSOCIATION AND ENERGY-RESOLVED ION-TRAP COLLISION-ACTIVATED DISSOCIATION FOR DIFFERENTIATING AROMATIC ISOMERIC IONS		122
5.1	Introduction.....	122
5.2	Materials and Methods.....	124
5.3	Results and Discussion	125
5.3.1	ERMS ITCAD and ERMS MCAD of the Molecular Ions of 1,6-Hexylpyrene 125	
5.3.2	ERMS ITCAD and ERMS MCAD of the Molecular Ions of 1-Methylfluorene and 9,10-Dihydroanthracene.....	128
5.3.3	ERMS ITCAD and ERMS MCAD of the Molecular Ions of 9,10- Dihydrophenanthrene and <i>Trans</i> -Stilbene.....	130
5.3.4	ERMS ITCAD and ERMS MCAD of the Molecular Ions of 3-, 6- and 8- Pentylquinolines	133
5.3.5	Comparison of Ion Loss for ERMS MCAD and ERMS ITCAD	139
5.4	Conclusions.....	140
5.5	References.....	141
PUBLICATIONS.....		143

LIST OF TABLES

Table 3.1 Molar concentrations of model compounds in each mixture.....	61
Table 3.2 Single-core and multicore model compounds studied.....	66
Table 4.1 List of isobaric model compounds.....	97
Table 4.2 Comparison of the size of the smallest aromatic cores, maximum numbers of carbons in alkyl chains, and relative abundances of single-core and multicore compounds in ions of different m/z derived from the asphaltene sample.	116
Table 5.1 Names and structures of the four isomeric sets of compounds studied.....	123

LIST OF FIGURES

- Figure 2.1 Schematic of an ESI process. The formation of charged droplets, generation of smaller charged droplets via evaporation of solvent molecules (S), and subsequent production of gas-phase analyte ions (MH^+) between the ESI needle and the MS inlet.22
- Figure 2.2 Schematics of the region between the ESI tip and the MS inlet. The sheath gas, auxiliary gas and sweep gas are indicated.23
- Figure 2.3 Schematic of the APCI process in positive ion mode.24
- Figure 2.4 A schematic of the components of a linear quadrupole ion trap (LQIT) mass spectrometer. The atmospheric pressure ionization region, the ion optics region, and the LQIT and detector region are highlighted in different colors. The operational pressures for each region are indicated beneath the diagram.26
- Figure 2.5 The RF voltages applied to the quadrupole present in the ion optics. RF voltages with the same frequency and amplitude are applied to opposite poles (P1) to control the ion motion in x direction. The same RF voltages, but 180 out-of-phase, are applied between neighboring poles (P2) to control ion motion in y direction.....28
- Figure 2.6 Typical DC offset voltage settings applied to the ion optics in the LQIT mass spectrometer to control ion motion in the z-direction.....29
- Figure 2.7 Schematics of an LQIT mass analyzer.30
- Figure 2.8 A typical Mathieu stability diagram. The circles represent ions of different m/z values. Larger circles represent the ions of larger m/z and vice versa. Ions located in the grey area have stable trajectories in the ion trap while ions located outside the grey area have unstable trajectories in the ion trap.33
- Figure 2.9 A schematic of the LQIT. The ion motion in the z-direction is controlled by applying higher DC potentials to the front and back sections of the LQIT and lower DC potentials to the center section. This creates a DC potential well (shown below) that restricts the ion motion in the z-direction. The colored dots indicate ions trapped in the potential well.....34
- Figure 2.10 The effect of helium on cooling the ions. The cooled ions have less kinetic energy and exist as a tighter group.35
- Figure 2.11 Mathieu stability diagram. In axial instability scanningfigure, ions are ejected at $q = 0.908$. In x-electrode bipolar resonance ejection, the q value of the ions is increased to 0.88 and a supplemental RF voltage is applied to eject the ions.37
- Figure 2.12 A schematic of ion detection by using electron multipliers in an LQIT.38

- Figure 2.13 a) The q value of the ion of interest is increased to 0.803. The ions of lower m/z values than the ions of interest are ejected from the ion trap. b) Application of a tailored broadband waveform results in the ejection of ions of greater m/z values than that of the ions of interest.....40
- Figure 2.14 The three different types of CAD techniques available in the commercial Thermo LTQ-Orbitrap XL mass spectrometer. Ion-source CAD occurs near the tube lens region in the ion source. Ion trap CAD occurs in the LQIT. Medium-energy CAD occurs in the multipole collision cell located behind the C-trap.41
- Figure 2.15 Schematic of ITCAD in the Thermo LTQ-Orbitrap XL mass spectrometer. The ions of interest are first isolated in the LQIT. The isolated ions are accelerated and undergo activating collisions with the helium buffer gas. The fragmenting ions are indicated by solid lines and the fragment ions are indicated using dashed lines...42
- Figure 2.16 Schematic of the ITCAD process. A) The q -value of the isolated ions is reduced to 0.25 by decreasing the RF amplitude. B) A supplementary RF voltage with the same frequency as that of the ions is applied to the x-electrode to increase the kinetic energy of the ions. Fragment ions are produced upon collisions between the accelerated ions with helium buffer gas.....44
- Figure 2.17 Schematic of ITCAD in the Thermo LTQ-Orbitrap XL mass spectrometer. A decrease in the DC voltage accelerates ions in the ion source region where they collide with nitrogen molecules. The fragmenting ions are indicated by solid lines and the fragment ions are indicated by dashed lines. The normal DC voltages and the ion-source CAD DC voltages are shown as solid and dashed lines, respectively.46
- Figure 2.18 A schematic of a Thermo Scientific LTQ Orbitrap XL mass spectrometer. The red lines indicate ion trajectories during injection from the C-trap into the orbitrap.47
- Figure 2.19 Injection of ions from the C-trap into the orbitrap. The red arrows indicate ion trajectories. The image current is produced due to the axial oscillation of the ions. The cylindrical coordinates r , z , and φ are indicated in the orbitrap.....49
- Figure 2.20 Schematic of the MCAD process in a Thermo LTQ-Orbitrap XL mass spectrometer. The ions of interest are isolated in the LQIT and then transported into the octopole collision cell. The ions are accelerated using a supplementary DC voltage and then collide with nitrogen in the octopole.52
- Figure 3.1 Changes in the RDBE values following CAD of an ionized single- and multicore compounds.59
- Figure 3.2 (+)APCI CS_2 mass spectra showing molecular ions of compounds in asphaltenes (a) Rose and (b) Montana. * Indicate instrument or chemical noise.63

- Figure 3.3 (a) A mass spectrum of the isolated molecular ions of 1,6-dipentylpyrene. (b) A MCAD mass spectrum measured for the molecular ions of 1,6-dipentylpyrene at a collision energy of 41 eV. (c) A mass spectrum of the isolated molecular ions of 1,4-di(pyren-1-yl)butane. (d) A MCAD mass spectrum measured for the molecular ions of 1,4-di(pyren-1-yl)butane at a collision energy of 41 eV.....65
- Figure 3.4 (+)APCI CS₂ mass spectrum showing molecular ions derived from the model compound mixture containing equimolar concentrations of six multicore and single-core compounds shown in Table 3.1 and Table S3.2. The red numbers indicate multicore ions and the black numbers indicate single-core ions. * Instrument or chemical noise.....67
- Figure 3.5 Plots of RDBE values as a function of the number of carbons in the molecular ions of model compounds and their fragment ions after MCAD at a collision energy of 12 eV. (a, b) the 0 % multicore mixture, (c, d) the 17 % multicore mixture, (e, f) the 50 % multicore mixture, (g, h) the 83% multicore mixture, and (i, j) the 100 % multicore mixture. Ions are represented by dots in the plot, with the ions' relative abundances indicated by the color of the dots. The weighted average RDBE values were calculated according to equation 1.....68
- Figure 3.6 (a) Percent changes in the weighted average RDBE values as a function of collision energy for MCAD for the five ionized model compound mixtures containing different multicore molar percentages (0 %, 17 %, 50 %, 83 %, and 100 %, indicated by lines of different colors; the %RDBE_{min} values are indicated) and (b) %RDBE_{min} values as a function of the molar ratio of multicore compound in the mixture.70
- Figure 3.7 (a) (+)APCI CS₂ mass spectrum showing molecular ions of m/z 350±10 derived from Montana asphaltenes and MCAD mass spectra of the molecular ions of m/z 350±10 measured at collision energies of (b) 20 eV, (c) 40 eV and (d) 60 eV. * Instrument or chemical noise.....72
- Figure 3.8 (a) (+)APCI CS₂ mass spectrum showing molecular ions of m/z 450±10 derived from Montana asphaltenes and MCAD mass spectra of the molecular ions of m/z 450±10 measured at collision energies of (b) 20 eV, (c) 40 eV and (d) 60 eV. * Instrument or chemical noise.....73
- Figure 3.9 (a) (+)APCI CS₂ mass spectrum showing molecular ions of m/z 550±10 derived from Montana asphaltenes and MCAD mass spectra of the molecular ions of m/z 550±10 measured at collision energies of (a) 20 eV, (c) 40 eV and (d) 60 eV. *Instrument or chemical noise.....74
- Figure 3.10 (a) (+)APCI CS₂ mass spectrum showing molecular ions of m/z 650±10 derived from Montana asphaltenes and MCAD mass spectra of the molecular ions of m/z 650±10 measured at collision energies of (b) 20 eV, (c) 40 eV and (d) 60 eV. *Instrument or chemical noise.75

- Figure 3.11 (a) (+)APCI CS₂ mass spectrum showing molecular ions of m/z 350±10 derived from Rose asphaltenes and MCAD mass spectra of the molecular ions of m/z 350±10 measured at collision energies of (b) 20 eV, (c) 40 eV and (d) 60 eV. *Instrument or chemical noise.76
- Figure 3.12 (a) (+)APCI CS₂ mass spectrum showing molecular ions of m/z 450±10 derived from Rose asphaltenes and MCAD mass spectra of the molecular ions of m/z 450±10 measured at collision energies of (b) 20 eV, (c) 40 eV and (d) 60 eV. *Instrument or chemical noise.77
- Figure 3.13 (a) (+)APCI CS₂ mass spectrum showing molecular ions of m/z 550±10 derived from Rose asphaltenes and MCAD mass spectra of the molecular ions of m/z 550±10 measured at collision energies of (b) 20 eV, (c) 40 eV and (d) 60 eV. *Instrument or chemical noise.78
- Figure 3.14 (a) (+)APCI CS₂ mass spectrum of molecular ions of m/z 650±10 derived from Rose asphaltenes and MCAD mass spectra of the molecular ions of m/z 650±10 measured at collision energies of (b) 20 eV, (c) 40 eV and (d) 60 eV. *Instrument or chemical noise.79
- Figure 3.15 The weighted average RDBE values as a function of collision energy upon MCAD for five groups of ions (molecular ions of m/z 350±10, 450±10, 550±10, 650±10, and all of these ions combined, indicated by lines of different colors) derived from (a) Rose asphaltenes and (b) Montana asphaltenes.80
- Figure 3.16 Percent change in the weighted average RDBE values as a function of collision energy after MCAD for five groups of ions (molecular ions of m/z 350±10, 450±10, 550±10, 650±10, and total, indicated by different colors) derived from (a) Rose asphaltenes and (b) Montana asphaltenes. The %RDBE_{min} values are indicated below the curve.81
- Figure 3.17 (a) Percent changes in the weighted average RDBE values upon ISCAD as a function of collision energy for the five ionized model compound mixtures with different multicore molar percentages (0 %, 17 %, 50 %, 83 %, and 100 %, indicated by lines of different colors) and (b) %RDBE_{min} values as proportions (mol/mol) of multicore compounds in the mixture.85
- Figure 3.18 Percent changes in the weighted average RDBE values as a function of collision energy after ISCAD for ionized Rose and Montana asphaltene samples. %RDBE_{min} values are labeled.87
- Figure 4.1 A mass spectrum of molecular ions of m/z 400±0.5 derived from the asphaltene sample (a), and a MS/MS spectrum of ions of ions of m/z 400±0.5 derived from the asphaltene sample measured at a MCAD collision energy of 30 eV (b). * indicates instrumental noise.99

- Figure 4.2 An MCAD spectrum (a) and a plot of RDBE values as a function of the number of carbons (b) of an ionized single-core compound measured at MCAD at a collision energy of 30 eV. An MCAD spectrum (c) and a plot of RDBE values as a function of the number of carbons (d) of an ionized multicore compound measured at MCAD at a collision energy of 60 eV. The ions are represented by the dots in the RDBE plot. The ions' relative signal intensities are indicated by the color of the dots.....101
- Figure 4.3 Plots of RDBE values as a function of the number of carbons in the molecular ions of three isobaric model compounds (a) and their fragment ions obtained upon MCAD at a collision energy of 30 eV (b) with the "horizontal streaks" 1 and 2 labeled. Reconstructed spectra of ions in "horizontal streak" 1 and 2 are shown in (c) and (d), respectively. The ions are represented by the dots in the RDBE plot. The ions' relative signal intensities are indicated by the color of the dots. The horizontal and diagonal streaks are indicated by red arrow and blue arrows.103
- Figure 4.4. Plots of RDBE values as a function of the number of carbons in molecular ions of m/z 400 ± 0.5 derived from the asphaltene sample (a) and their fragment ions obtained upon MCAD at a collision energy of 32 eV (b). The ions are represented by the dots in the RDBE plot. The ions' relative signal intensities are indicated by the color of the dots.....105
- Figure 4.5 The re-constructed spectra that correspond to ions in fragmentation series 1 (a), fragmentation series 2 (b), and fragmentation series 3 (c) that are highlighted in figure 4b, respectively.....107
- Figure 4.6 Plots of RDBE values as a function of the number of carbons in molecular ions of m/z 400 ± 0.5 (a), 500 ± 0.5 (b), 600 ± 0.5 (c), and 700 ± 0.5 (d) derived from the asphaltene sample. The ions are clustered into 5 groups and is indicated by the numbers next to the circle. The ions are represented by the dots in the RDBE plot. The ions' relative signal intensities are indicated by the color of the dots.109
- Figure 4.7 Plots of RDBE values as a function of the number of carbons in molecular ions of m/z 400 ± 0.5 (a), 500 ± 0.5 (b), 600 ± 0.5 (c), and 700 ± 0.5 (d) derived from the asphaltene sample measured at MCAD collision energy 32 eV, 40 eV, 48 eV, and 56 eV, respectively. The ions are clustered into 5 groups, indicated by the numbers next to each cluster. The ions are represented by the dots in the RDBE plot and the relative signal intensities are indicated by the color of the dots.110
- Figure 4.8 Re-constructed spectra that correspond to ions in fragmentation series 1 (a), fragmentation series 2 (b), fragmentation series 3 (c), and fragmentation series 4 (d) that are highlighted in figure 7b, respectively112
- Figure 4.9 Re-constructed spectra that correspond to ions in fragmentation series 1 (a), fragmentation series 2 (b), fragmentation series 3 (c), fragmentation series 4 (d) and fragmentation series 5 (e) that are highlighted in figure 7c, respectively.....113

- Figure 4.10 Re-constructed spectra that correspond to ions in fragmentation series 1 (a), fragmentation series 2 (b), fragmentation series 3(c), fragmentation series 4(d), fragmentation series 5 (e), and fragmentation series 6 (f) that are highlighted in figure 7d, respectively.....114
- Figure 4.11 A summary of the sizes of smallest aromatic core (a) and maximum numbers of carbon in alkyl chains (b) in the ions of m/z 400, 500, and 600 derived from the asphaltene samples.....118
- Figure 5.1. ITCAD spectra measured for the molecular ions of 1,6-hexylpyrene (MW 370 Da) at collision energies of (a) 30, (b) 60 and (c) 100 (arbitrary units).....126
- Figure 5.2. MCAD mass spectrum measured for the molecular ions of 1,6-hexylpyrene (MW 370 Da) at a collision energy of (a) 22 eV, (b) 44 eV, and (c) 74 eV.....127
- Figure 5.3 ERMS ITCAD mass spectra of the isomeric molecular ions of (a) 1-methylfluorene and (b) 9,10-dihydroanthracene (m/z 180). ERMS MCAD mass spectra of the molecular ions of (c) 1-methylfluorene and (d) 9,10-dihydroanthracene (m/z 180).129
- Figure 5.4 ERMS ITCAD mass spectra of the molecular ions of (a) 9,10-dihydrophenanthrene and (b) *trans*-stilbene. The ERMS MCAD mass spectra of the molecular ions of (c) 9,10-dihydrophenanthrene and (d) *trans*-stilbene.131
- Figure 5.5 ERMS ITCAD mass spectra of the isomeric molecular ions of (a) 9,10-dihydroanthracene and (b) 9,10-dihydrophenanthrene (m/z 180). ERMS MCAD mass spectra of the molecular ions of (c) 9,10-dihydroanthracene and (d) 9,10-dihydrophenanthrene.....132
- Figure 5.6 ERMS ITCAD mass spectra of the molecular ions of (a) 3-pentylquinoline, (b) 6-pentylquinoline, and (c) 8-pentylquinoline. ERMS MCAD mass spectra of the molecular ions of (d) 3-pentylquinoline, (e) 6-pentylquinoline, and (f) 8-pentylquinoline.134
- Figure 5.7 MCAD MS/MS spectra of the molecular ions of (a) 8-pentylquinoline, (b) 6-pentylquinoline, and (c) 3-pentylquinoline at a normalized collision energy of 28 eV.135
- Figure 5.8 MCAD MS/MS spectra of the molecular ions of (a) 8-pentylquinoline, (b) 6-pentylquinoline, and (c) 3-pentylquinoline at a collision energy of 40 eV.136
- Figure 5.9 Proposed fragmentation pathways for MCAD of the molecular ions of a) 3-pentylquinoline, (b) 6-pentylquinoline, and (c) 8-pentylquinoline.....138
- Figure 5.10 The total ion abundance versus the collision energy during ERMS ITCAD and ERMS MCAD. Ion loss during ITCAD-ERMS of molecular ions of (a) 1-methylfluorene, (c) 9,10-dihydroanthracene. Ion loss during ERMS MCAD of molecular ions of (b) 1-methylfluorene, (d) 9,10-dihydroanthracene.139

ABSTRACT

Author: Dong, Xueming. PhD

Institution: Purdue University

Degree Received: May 2019

Title: The Development of Tandem Mass Spectrometric Methods for Characterization of Asphaltenes and Differentiation of Small Organic Isomers

Committee Chair: Hilikka I. Kenttämäa

High-resolution mass spectrometry (MS) and tandem mass spectrometry (MS/MS) are powerful tools for the characterization of the molecular structures of components of both simple and complex mixtures. MS and MS/MS have played key roles in many fields, including proteomics, metabolomics, and petroleomics. This thesis focuses on the development of tandem mass spectrometric methods for the structural characterization of asphaltenes and small isomeric molecules. In addition, this thesis also presents a method to address a sampling bias in asphaltene analysis.

Chapter 2 describes the fundamental aspects of the mass spectrometer used for the research discussed in this thesis. Chapter 3 presents an in-depth study on the determination of the relative abundances of single-core and multicore compounds in asphaltenes. A statistical sampling bias in many earlier asphaltene studies is discussed and a rapid and simple alternative method is introduced to address this sampling bias. Chapter 4 presents an investigation of the sizes of aromatic cores and lengths of alkyl chains in isobaric ions derived from asphaltenes by using an improved data analysis method. Chapter 5 presents a fundamental study on utilization of energy-resolved collision-activated dissociation (CAD) for the differentiation of isomeric ions. Energy-resolved CAD was used to compare the ability of two different activation methods to differentiate four sets of isomeric ions of aromatic hydrocarbons. The comparison suggests that medium-energy CAD (MCAD; commercially known as higher-energy collision dissociation, HCD) is more powerful in differentiation of the four sets of isomers than conventional ion trap CAD (ITCAD).

CHAPTER 1. INTRODUCTION

1.1 Introduction

The first mass spectrometer was developed by J.J. Thompson and F.W. Aston during the 1910s.¹ After over a century of development, mass spectrometry (MS) is currently one of the most powerful and popular methods in analytical chemistry and plays key roles in a wide range of research areas.²⁻⁴

A typical MS experiment is composed of three events: evaporation and ionization, ion separation, and ion detection.⁵ During evaporation and ionization, gas-phase ions are generated from analytes. During ion separation, ions with different mass-to-charge ratios (m/z) are separated in the mass analyzer. Finally, the abundances of separated ions are measured by the ion detector. The resulting mass spectrum shows the ions' m/z values on the x-axis and their relative abundances on the y-axis.

The development of high-resolution mass spectrometers has allowed for the very accurate determination of ion m/z values, therefore providing information on the elemental compositions of ions.⁶ Structural information for the ionized compounds is obtained by using tandem mass spectrometry (MS/MS) experiments. In the most common MS/MS experiments, the ions of interest are isolated and then fragmented using one of several different activation methods. Collision-activated dissociation (CAD) is arguably the most popular method. In a CAD experiment, isolated ions are accelerated and allowed to collide with neutral atoms (e.g., helium or argon) or molecules (e.g., nitrogen). During the collisions, part of the kinetic energy of the ions is converted into their internal energy, ultimately inducing fragmentation. The m/z values and relative abundances of the fragment ions can provide structural information for the fragmenting ion.

1.2 Thesis overview

This thesis focuses on the development of tandem mass spectrometric methods for the elucidation of the structures of asphaltenes and differentiation of small aromatic hydrocarbon isomers, such as 3-, 6-, and 8-pentylquinolines. Chapter 2 introduces fundamental aspects of tandem mass spectrometry, in addition to detailed operation principles relevant to the techniques employed in this thesis.

Chapter 3 discusses an MS/MS investigation based on CAD of the relative abundances of single-core and multicore compounds in asphaltenes. The relative abundances of these compounds have been debated for decades without a consensus. In many earlier CAD investigations, conclusions were made on the relative abundances based on examination of only a limited number of ions. This approach is essentially based on the assumption that the relative abundances of single- and multicore compounds are uniform within the entire sample regardless of the molecular weights of the compounds. In this study, medium-energy collision-activated dissociation (MCAD) in a linear quadrupole ion trap/orbitrap high-resolution mass spectrometer was employed to explore and compare the relative abundances of single-core and multicore compounds in two different asphaltene samples. To increase the representative sample size and improve on previous methods, ions with m/z values in the ranges of 350 ± 10 , 450 ± 10 , 550 ± 10 and 650 ± 10 were studied for each asphaltene sample. These groups of ions were isolated and subjected to MCAD. The ions displayed different relative decreases in their weighted average ring and double bond equivalents (RDBE), suggesting that the abundances of single-core and multicore compounds are not uniform within the entire asphaltene samples. Therefore, traditional mass spectrometry approaches used to determine these relative abundances are likely to suffer from a sampling bias. As opposed to MCAD, ion-source collision-activated dissociation (ISCAD) is not susceptible to sampling bias because no ion selection is involved. Thus, ISCAD can be used for a relatively unbiased evaluation of the relative abundances of single-core and multicore compounds in different asphaltenes.

Chapter 4 presents an investigation of the sizes of the aromatic cores and lengths of the alkyl chains in isobaric ions derived from asphaltenes by using MCAD and an improved data analysis method. One of the major challenges in MS-based elucidation of the structures of asphaltenes is that the fragmenting ions cannot be easily correlated to their

fragment ions as asphaltenes are very complex mixtures. It has been demonstrated in the literature that single-core ions generate fragment ions with similar ring and double bond equivalence (RDBE) values. As a result, fragmenting ions and fragment ions derived from a single-core compound can be correlated based on their similar RDBE values. A mass spectrum of measured for ions of m/z 400 ± 0.5 derive from an asphaltene sample showed three clusters of fragmenting ions with RDBE values ~ 12 , 18, and 24, respectively. A CAD mass spectrum of these ions showed three clusters of fragment ions with RDBE values ~ 12 , 18, and 24, respectively. These three clusters fragment ions are likely derived from the fragmenting ions of similar RDBE values and are referred to as ion clusters from hereon. A CAD mass spectrum for each ion cluster was reconstructed for characterization of the ions' structure. The structures of ion clusters of m/z 400 ± 0.5 , 500 ± 0.5 , 600 ± 0.5 , and 700 ± 0.5 derived from an asphaltene sample were explored using this approach. Overall, the study revealed that ions with a greater m/z value and a larger RDBE value tend to have larger aromatic cores. Additionally, ions with a larger m/z value and a lower RDBE value tend to have the largest alkyl chains.

Chapter 5 compares the ability of two energy-resolved CAD methods to differentiate challenging isomeric ions. CAD can be performed in the ion trap of the linear quadrupole ion trap (LQIT)/orbitrap mass spectrometer. This CAD method is referred to as ion-trap CAD (ITCAD). ITCAD is demonstrated here to fail to differentiate specific classes of isomeric hydrocarbon ions. An alternate approach, medium-energy CAD (MCAD, commercially known as higher-energy collision dissociation or HCD) performed in the octupole collision cell of the mass spectrometer, is an alternative approach for differentiation of isomeric ions. The isomeric hydrocarbon ions that could not be differentiated using energy-resolved ITCAD were differentiated by using energy-resolved MCAD. In addition, at high collision energies, energy-resolved MCAD showed minimal ion loss compared to energy-resolved ITCAD, a potential advantage when the sample concentration is low.

1.3 References

- (1) Thomson, J. J. *Rays of Positive Electricity and Their Application to Chemical Analyses*; Longmans, Green and Company, 1921; Vol. 1.
- (2) Dettmer, K.; Aronov, P. A.; Hammock, B. D. Mass Spectrometry - Based Metabolomics. *Mass Spectrom. Rev.* **2007**, *26*, 51-78.
- (3) Wales, T. E.; Engen, J. R. Hydrogen Exchange Mass Spectrometry for the Analysis of Protein Dynamics. *Mass Spectrom. Rev.* **2006**, *25*, 158-170.
- (4) Bantscheff, M.; Schirle, M.; Sweetman, G.; Rick, J.; Kuster, B. Quantitative Mass Spectrometry in Proteomics: A Critical Review. *Anal. Bioanal. Chem.* **2007**, *389*, 1017-1031.
- (5) Bruins, A. Mass Spectrometry with Ion Sources Operating at Atmospheric Pressure. *Mass Spectrom. Rev.* **1991**, *10*, 53-77.
- (6) Xian, F.; Hendrickson, C. L.; Marshall, A. G. High Resolution Mass Spectrometry. *Anal. Chem.* **2012**, *84*, 708-719.

CHAPTER 2. INSTRUMENTATION AND EXPERIMENTAL DETAILS CONCERNING HYBRID LINEAR QUADRUPOLE ION TRAP-ORBITRAP MASS SPECTROMETERS

2.1 Introduction

MS analysis typically involves three stages: 1) evaporation of the sample, 2) ionization of the compounds, 3) separation of the gas-phase ions based on their mass-to-charge ratios (m/z) and measurement of the ion abundances. All of the studies discussed in this thesis were performed using a Thermo LQIT/orbitrap mass spectrometer (Thermo LTQ/Orbitrap XL). This chapter will describe the theory underlying the desorption, ionization, separation and abundance measurement steps outlined above. Tandem mass spectrometry based on CAD was used extensively to reveal information about ion structures.

Evaporation and ionization of compounds is the prerequisite for most MS analysis. Significant efforts have been devoted to the development of desorption/ionization techniques. In the early stages of MS, evaporation was accomplished by thermal heating and the gas-phase molecules were ionized by electron ionization¹ (EI) and chemical ionization (CI).² EI and CI can only be used to ionize compounds in the gas phase, thus limiting the analysis to thermally stable and volatile compounds. This limitation was addressed with the development of fast-atom bombardment (FAB),³ field desorption/field ionization (FD/FI),^{4,5} electrospray ionization (ESI),⁶ matrix-assisted laser desorption ionization (MALDI),⁷ atmospheric-pressure chemical ionization (APCI),⁸ atmospheric-pressure photoionization (APPI),⁹ desorption electrospray ionization (DESI),¹⁰ desorption atmospheric-pressure chemical ionization (DAPCI),¹¹ and direct analysis in real-time (DART).¹² The ionization methods employed in this thesis, ESI and APCI, are discussed in detail in this section.

2.2 Ionization

2.2.1 Electrospray Ionization (ESI)

ESI is a soft ionization method first reported in 1989.^{13,14} ESI can be used to ionize large and thermally labile polar compounds without significant fragmentation. Several mechanisms have been proposed for ESI. One of them is as follows: 1) Charged droplets are generated at a capillary tip that has high voltage applied to it. 2) The droplets travel towards the MS inlet and shrink as the solvent molecules evaporate. 3) Gas-phase ions are produced from the small charged droplets via several possible mechanisms that will be discussed below. An overview of the ionization process is provided in Figure 2.1 and discussed in detail in the following paragraphs.

When the analyte solution exits the capillary under a high electric potential (e.g., 3-5 kV during ESI), a Taylor cone is formed.^{15,16} A plume of charged droplets are ejected from the Taylor cone and travels toward the electrically-grounded MS inlet. The structural integrity of the charged droplets is affected by the balance between the surface tension of the solvent and Coulombic repulsion between the charged particles on the surface of the droplet. As the charged droplets travel towards the MS inlet, solvent molecules evaporate, and the increased charge density on the surface of the droplet causes an increase in the Coulombic repulsion. When the Coulombic repulsion exceeds the surface tension, the droplet becomes unstable at a point known as the Rayleigh instability limit.^{17,18} The unstable charged droplets undergo a series of Coulombic explosions, producing increasingly smaller droplets. Eventually, gas-phase ions are produced from the droplets, and these ions enter the MS inlet via the ion transfer capillary. To facilitate solvent evaporation and ion desolvation, a nebulization gas such as nitrogen is generally used.¹⁹ Three types of nebulization gases can be used during a typical ESI process: a sheath gas, an auxiliary gas, and a sweep gas. The sheath gas flows from near the capillary tip, the auxiliary gas flows from near the spray nozzle, and the sweep gas flows from the opening of the sweep cone (Figure 2.2). At low solution flow rates, sheath gas and auxiliary gases are often used to stabilize the spray and facilitate desolvation. Sweep gas is usually required for very high solution flow rates. However, nebulization gases are normally not employed when the flow rate is very low, as is the case with nanospray ESI.²⁰

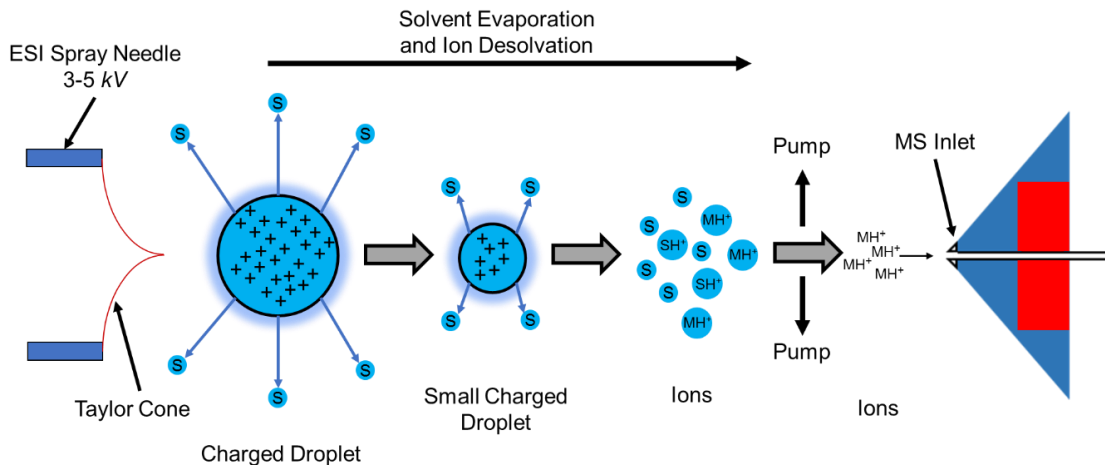


Figure 2.1 Schematic of an ESI process. The formation of charged droplets, generation of smaller charged droplets via evaporation of solvent molecules (S), and subsequent production of gas-phase analyte ions (MH^+) between the ESI needle and the MS inlet.

The underlying mechanism(s) for the generation of gas-phase ions from the liquid droplets upon ESI remain uncertain. Currently, there are two main models to explain the gas-phase ion generation process.²¹⁻²⁴ Based on the charged residue model²⁵ (CRM), gas-phase ions are generated from the charged droplets when all of the solvent molecules in the droplet evaporate. The analyte molecules receive most of the charges carried by the droplet. However, according to the ion evaporation model²⁶ (IEM), as the charge density on the surface of the droplet becomes increasingly high, gas-phase ions are released from the surface of the droplet via a mechanism similar to field desorption/ionization.²⁶ Currently, it is believed that the CRM better describes the formation of gas-phase ions from large analytes, such as proteins, while the IEM better describes the formation of gas-phase ions from small analytes.^{27,28}

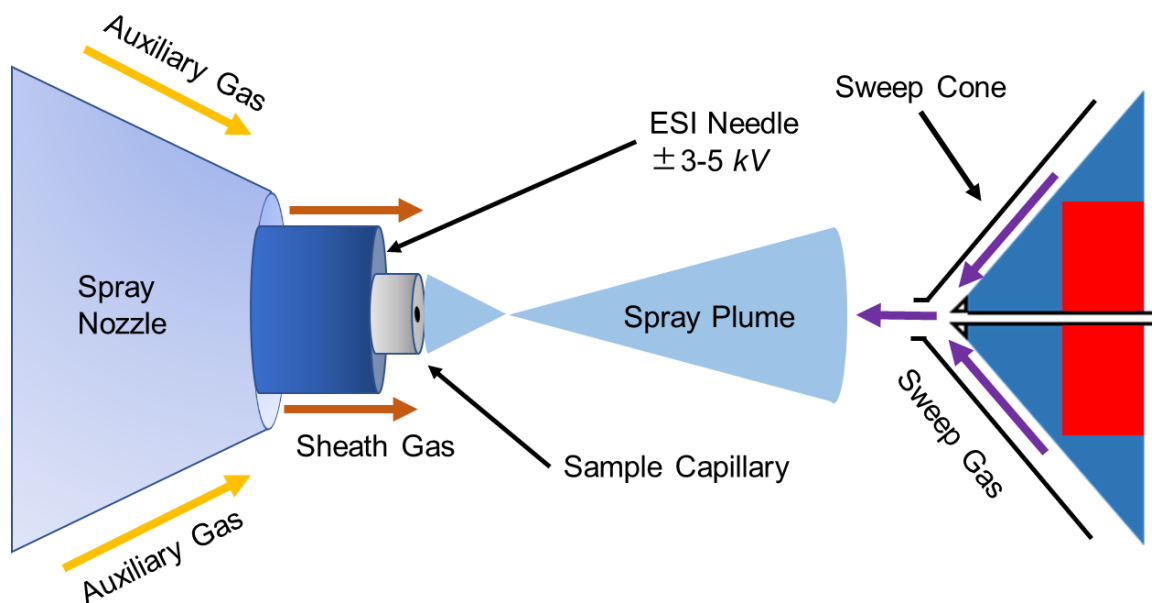


Figure 2.2 Schematics of the region between the ESI tip and the MS inlet. The sheath gas, auxiliary gas and sweep gas are indicated.

2.2.2 Atmospheric-Pressure Chemical Ionization (APCI)

APCI is a soft ambient ionization technique developed to ionize analytes with medium to low polarities and molecular weights.⁸ The hypothesized mechanism of APCI is illustrated in Figure 2.3. During APCI, the analyte solution is introduced into the ion source through a transfer capillary that is heated by a ceramic heater to 300-500 °C while nitrogen acts as a nebulization gas to facilitate solvent evaporation. The analyte solution leaves the transfer capillary as small droplets and eventually becomes a vapor composed of solvent and analyte molecules. A corona discharge needle with an applied voltage of 2-4 kV ionizes the nebulization gas to produce primary ions. The primary ions then react with solvent molecules in the gas phase to generate solvent ions. Finally, the solvent ions react with the analyte molecules to form analyte ions. The chemical reactions that have been hypothesized to occur during APCI is illustrated in Scheme 2.1. Although the ESI and APCI sources in the Thermo LTQ-Orbitrap XL mass spectrometer share the same atmospheric pressure ionization platform, the two ionization processes may be

fundamentally different because it is hypothesized that ionization in APCI occurs in the gas phase while that of ESI occurs in the liquid phase.

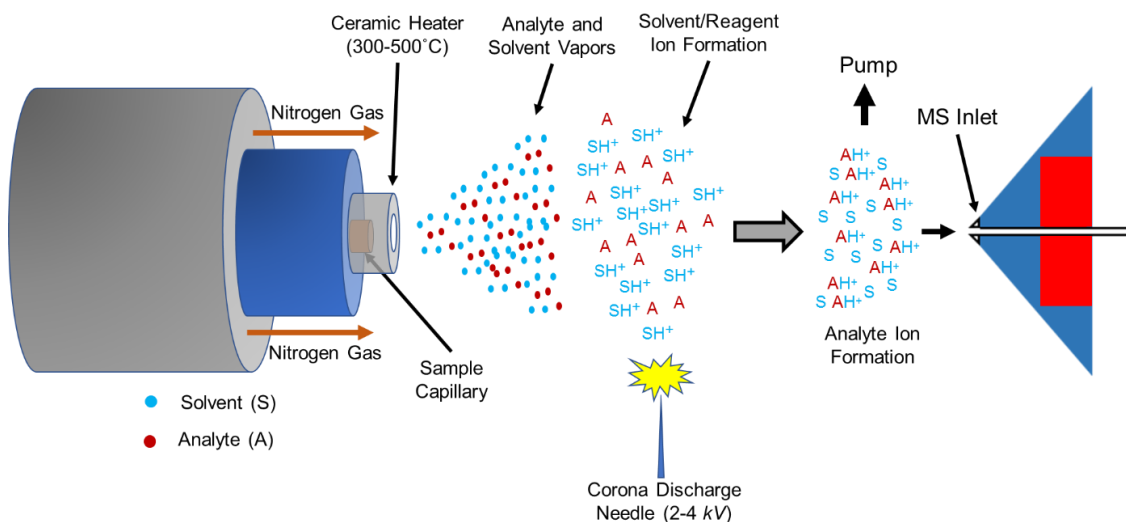
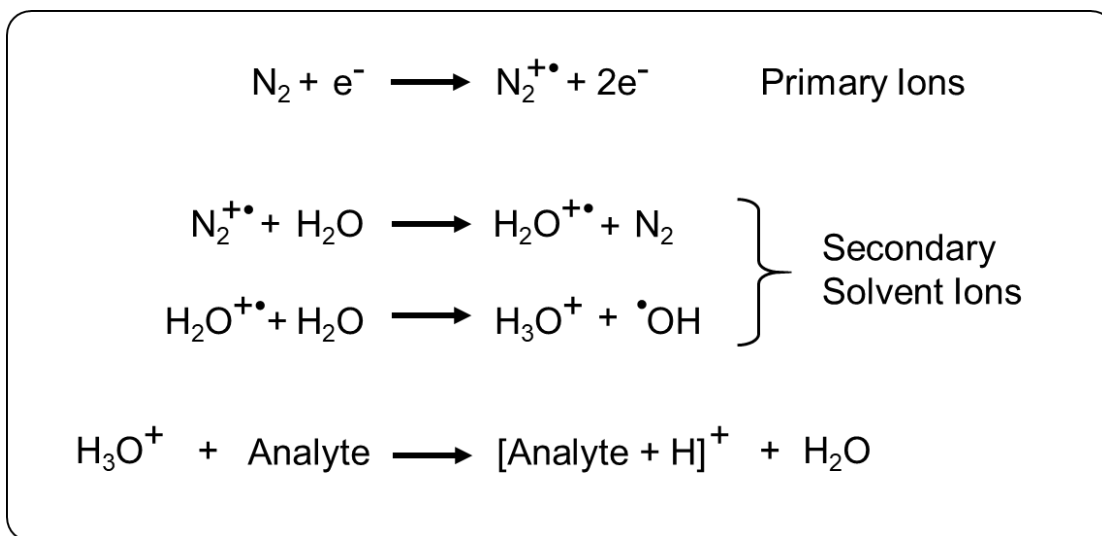


Figure 2.3 Schematic of the APCI process in positive ion mode.



Scheme 2.1 Mechanism of APCI ionization in positive ion mode for the generation of protonated analytes when using water solvent.

2.3 Overview of the Linear Quadrupole Ion Trap (LQIT) Mass Spectrometer

A schematic of a commercial LQIT mass spectrometer (Thermo LTQ) is shown in Figure 2.4. The LQIT mass spectrometer can be divided into three regions: 1) the atmospheric-pressure ionization (API) region, 2) the ion optics region, and 3) the mass analyzer and ion detection region. Each of these regions is discussed in detail in the following sections.

2.4 The Atmospheric Pressure Ionization (API) Region

The API region can be subdivided into the API source region (operated at atmospheric pressure) and the API stack region (operated at ~ 1 Torr). The vacuum was generated with two Edwards E2M30 mechanical pumps, each operated at 650 L/min.

In the API source, gaseous ions are commonly generated using electrospray ionization (ESI), atmospheric pressure photoionization (APPI) or atmospheric pressure chemical ionization (APCI). In the API stack, the ions from the API source are drawn into the ion transfer capillary via an electric field. In positive ionization mode, a positive DC voltage is applied to prevent gaseous cations from colliding with the capillary. A positive voltage is applied to the tube lens to focus the ions towards the opening of the skimmer in positive ionization mode. A negative voltage is applied to the tube lens in negative ionization mode. The skimmer acts as a vacuum baffle between the API stack region (~ 1 Torr) and the multipole 00 compartment (Figure 2.4, top) (~ 0.05 Torr). The skimmer cone orifice is located off-center to the ion transfer capillary tube. The voltage applied to the tube lens does not affect neutral molecules. Thus, the neutral molecules collide with the surface of the skimmer cone (Figure 2.4). This is done to prevent neutral molecules from entering the mass spectrometer.

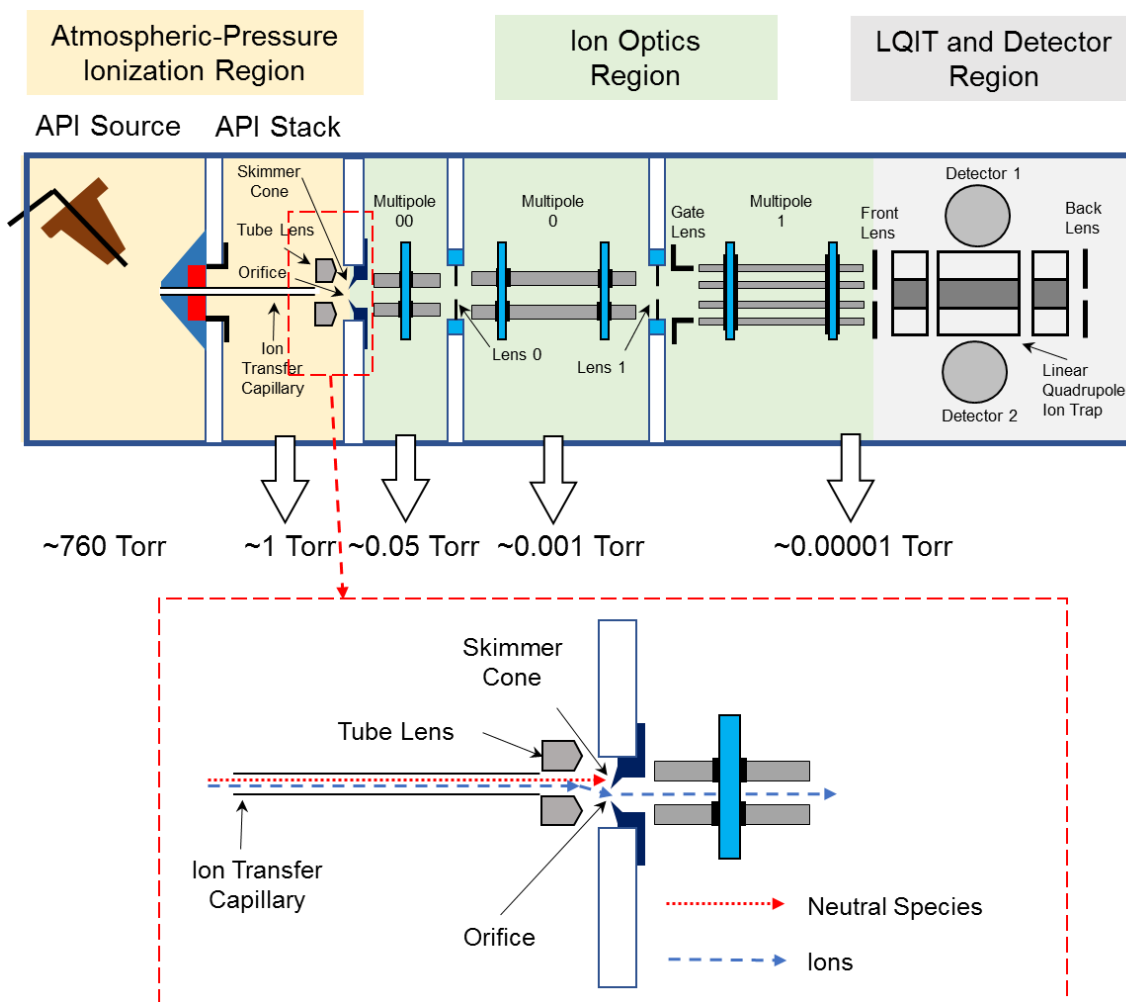


Figure 2.4 A schematic of the components of a linear quadrupole ion trap (LQIT) mass spectrometer. The atmospheric pressure ionization region, the ion optics region, and the LQIT and detector region are highlighted in different colors. The operational pressures for each region are indicated beneath the diagram.

2.4.1 The Ion Optics Region

The ion optics region contains three multipoles. These multipoles are referred to as multipole 00, multipole 0, and multipole 1, and each is located in a different compartment (Figure 2.4). These compartments are differentially pumped by a Leybold TW turbo molecular pump. The multipole 00, 0, and 1 compartments are pumped at rates of 1,500 L/min, 18,000 L/min, and 24,000 L/min, respectively, generating a vacuum of ~0.5 Torr, ~0.001 Torr, and 0.00001 Torr, respectively.

The gaseous ions generated in the API region are transported via ion optics into the mass analyzer. The ion optics region also serves as a buffer zone between the higher pressure API region (1 Torr to 0.001 Torr) and the low pressure ion trap region (0.00001 Torr). Transportation of the ions is achieved with two quadrupoles (multipole 00 and multipole 0) followed by an octopole (multipole 1) (Figure 2.4).²⁹ The multipoles restrict ion motion in the x direction by applying identical repulsive RF voltages on opposing electrodes (P1, Figure 2.5). Ion motion in the y direction is controlled in a similar manner. The applied frequency is the same for all rods but the amplitude is 180° out of phase for adjacent rods (P2, Figure 2.5). As a result, the ions follow a circular, oscillating trajectory when travelling through the multipoles.

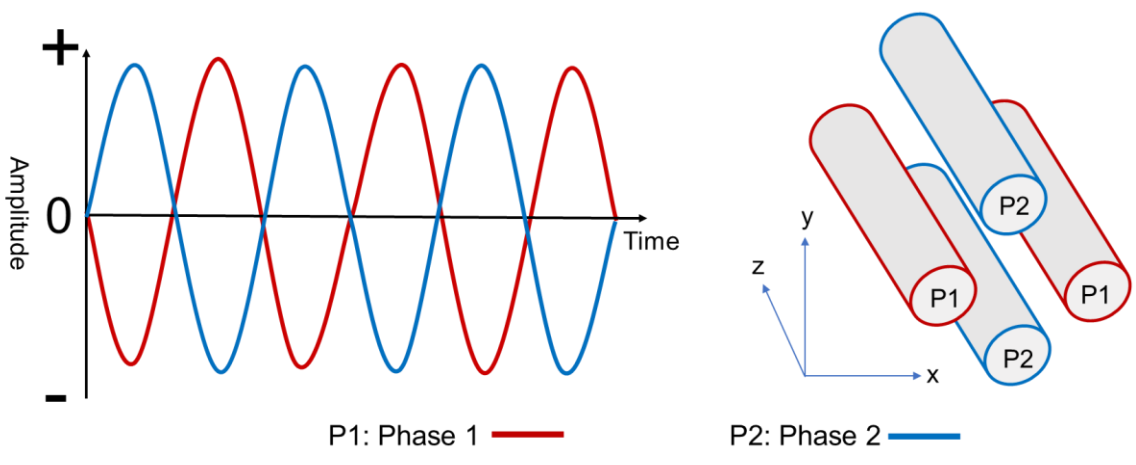


Figure 2.5 The RF voltages applied to the quadrupole present in the ion optics. RF voltages with the same frequency and amplitude are applied to opposite poles (P1) to control the ion motion in x direction. The same RF voltages, but 180 out-of-phase, are applied between neighboring poles (P2) to control ion motion in y direction.

Ion motion in the z direction is controlled by DC voltages applied to lenses in the mass spectrometer (Figure 2.3). Throughout the ion optics, a lower (i.e., more negative) potential is applied to each of the lenses, which attracts the positive ions. This DC potential accelerates and guides the ions towards the ion trap.

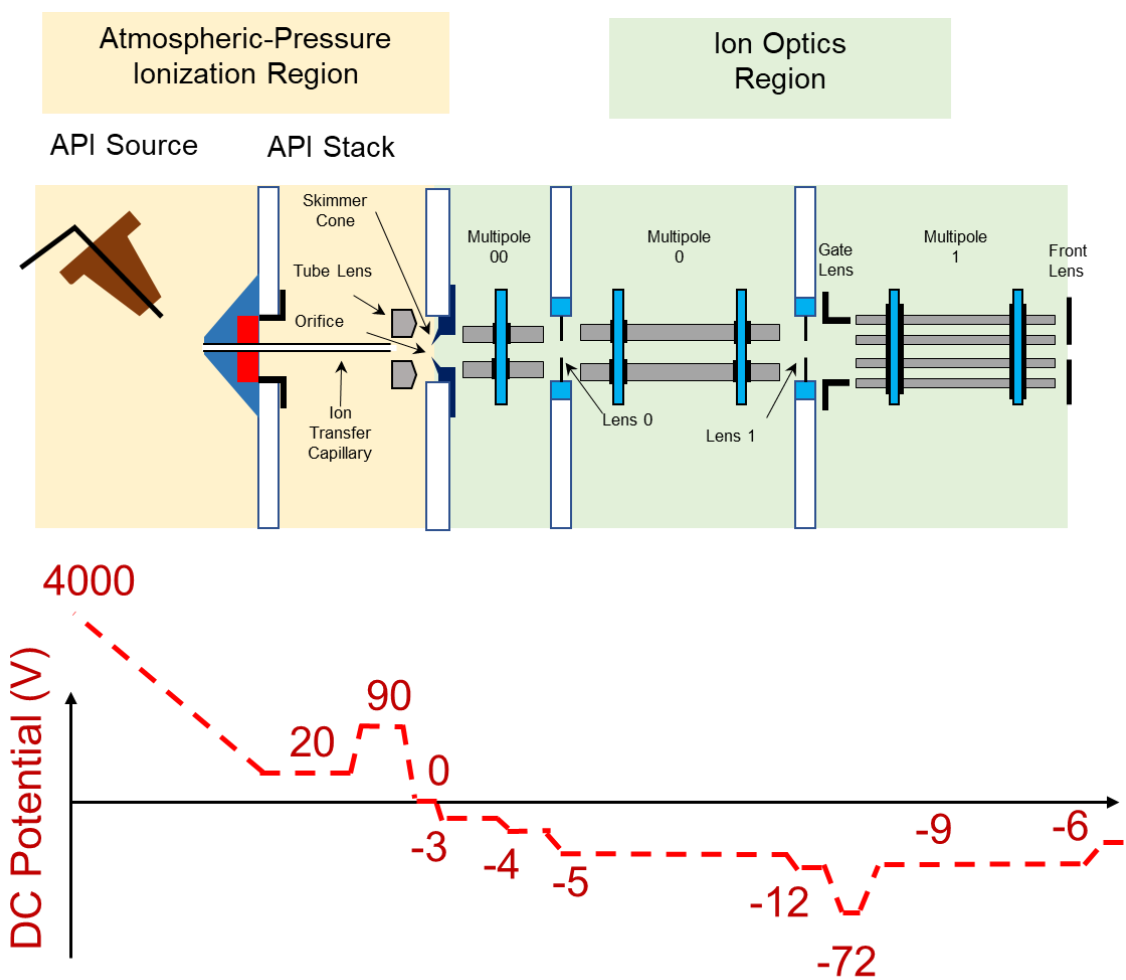


Figure 2.6 Typical DC offset voltage settings applied to the ion optics in the LQIT mass spectrometer to control ion motion in the z -direction.

2.4.2 Ion Trap Region

A typical LQIT consists of a front section, a center section, and a back section (Figure 2.7).

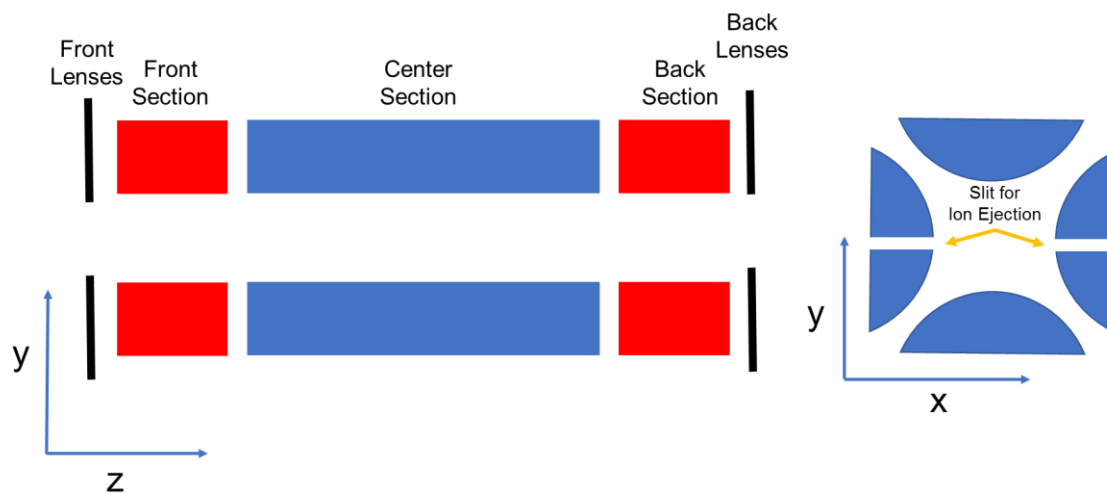


Figure 2.7 Schematics of an LQIT mass analyzer.

2.5 Fundamental Aspects of Linear Quadrupole Ion Traps

The main functions of the ion trap include ion trapping, isolation, excitation, and ejection. These functions are discussed in this section.

2.5.1 Ion Trapping

Ion trapping in the LQIT is achieved using DC and RF voltages applied to the four ion trap electrodes.³⁰ The ion motion in the x and y directions is controlled by the RF voltage and the ion motion in the z-direction is controlled by the DC voltages. In addition, helium is often used to collisionally cool the ions in the LQIT. The RF voltages have a fixed amplitude and frequency. Similar to the ion optics quadrupoles, RF voltages of the same amplitude but with a frequency 180° out of phase are applied to adjacent electrodes. The ions' motion in the z-direction is controlled by DC voltages applied to the front section and the back section. For ion detection, two of the center section electrodes (x direction, Figure 2.7 right) contain slits for ion ejection. Ion excitation, isolation, and ejection are

achieved by applying supplemental RF voltages with different frequencies and amplitudes to the electrodes in the x direction. The principles for ion isolation, excitation, and ejection will be discussed in detail in Section 2.5.

2.5.1.1 Ion Motion in x- and y-Directions

The two-dimensional RF-field Φ_0 can be described by the following equation:

$$\pm\Phi_0 = \pm(U - V \cos \Omega t) \quad (2.1)$$

where U is the applied DC voltage, V is the amplitude of the RF voltage, and Ω is the angular frequency. The potentials experienced by the ions in the LQIT in the x- and y-directions ($\Phi_{x,y}$) can be described by the following equation:

$$\Phi_{x,y} = \frac{\Phi_0(x^2 - y^2)}{r_0^2} = \frac{(U - V \cos \Omega t)(x^2 - y^2)}{r_0^2} \quad (2.2)$$

where r_0 is the radius of the circles inscribed by the four electrodes in LQIT.

The force experienced by the ions inside the LQIT in the x (F_x) and y (F_y) direction can be expressed as:

$$F_x = m \frac{d^2x}{dt^2} = -ze \frac{d\Phi}{dx} \quad (2.3)$$

$$F_y = m \frac{d^2y}{dt^2} = -ze \frac{d\Phi}{dy} \quad (2.4)$$

where m is the mass of the ion, z is the number of charges of the ion, and e is the charge of an electron (1.6×10^{-19} Coulombs).

Based on the force experienced by the ions in the x- and y-directions (equations 2.3 and 2.4), the motion of the ions in the x- and y-directions can be expressed by using the following equations:³⁰

$$\frac{d^2x}{dt^2} + \frac{2ze}{mr_0^2} (U - V \cos \Omega t)x = 0 \quad (2.5)$$

$$\frac{d^2y}{dt^2} + \frac{2ze}{mr_0^2} (U - V \cos \Omega t)y = 0 \quad (2.6)$$

Equations 2.5 and 2.6 are similar to the general form of the Mathieu equation developed in the 1860s:³⁰

$$\frac{d^2u}{d\xi^2} + (a_u + 2q_u \cos 2\xi)u = 0 \quad (2.7)$$

When $\xi = \frac{\Omega t}{2}$, equations 2.5 and 2.6 can be re-arranged as the Mathieu equations:

$$q_u = q_x = \frac{4zeV}{mr_0^2\Omega^2} \quad (2.8)$$

$$a_u = a_x = \frac{8zeU}{mr_0^2\Omega^2} \quad (2.9)$$

where a_u (or a) and q_u (or q) are the Mathieu stability parameters shown in the Mathieu stability diagram in Figure 2.8.

The Mathieu stability diagram describes the stability of ion trajectories in the ion trap based on the parameters a and q defined in equations 2.8 and 2.9, respectively. As Figure 2.8 indicates, the ion trajectories can be stable in the x-direction but not the y-direction, stable in the y-direction but not the x-direction, stable in both the x- and y-directions, or unstable in both the x- and y-directions. Only ions with a and q values corresponding to stable trajectories in both the x- and y-directions (grey area, Figure 2.8) can be trapped. According to equation 2.8, ions of larger m/z values have smaller q values.

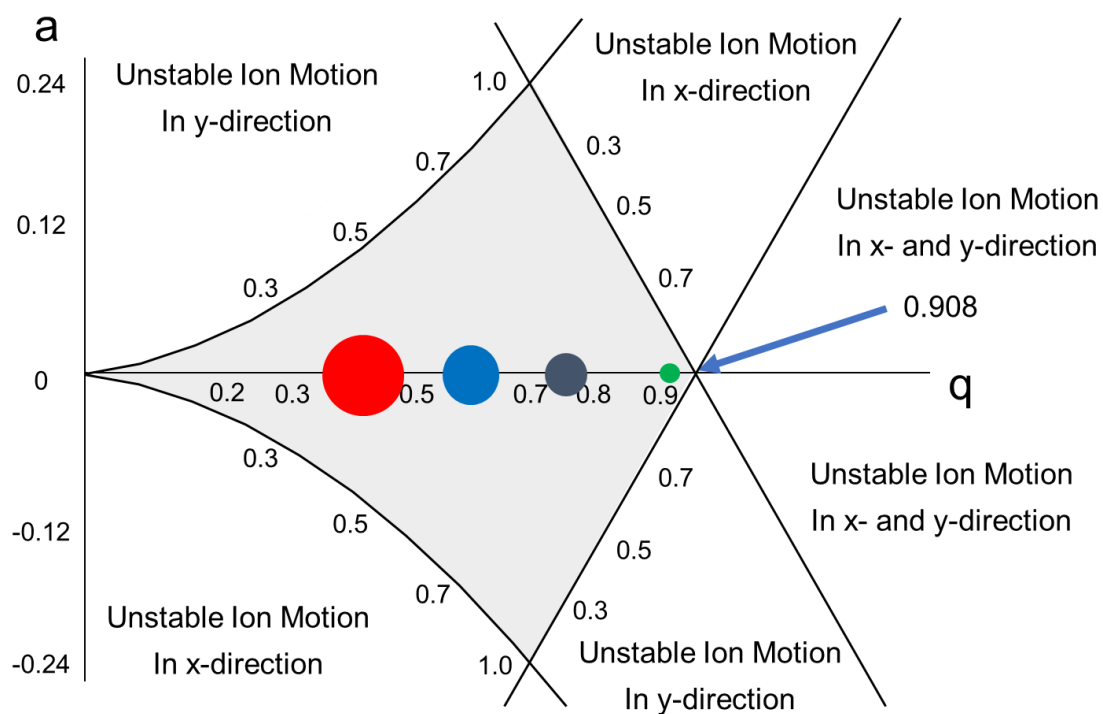


Figure 2.8 A typical Mathieu stability diagram. The circles represent ions of different m/z values. Larger circles represent the ions of larger m/z and vice versa. Ions located in the grey area have stable trajectories in the ion trap while ions located outside the grey area have unstable trajectories in the ion trap.

2.5.1.2 Ion Motion in the z-Direction

Different DC voltages can be applied to each of the three sections of the LQIT (Figure 2.7). A low DC voltage is applied in the center section to attract the ions, while a higher DC voltage is applied on the back and front sections to prevent the ions from escaping the ion trap. This creates a potential well that restricts the ion motion in the z-direction in the LQIT (Figure 2.9).

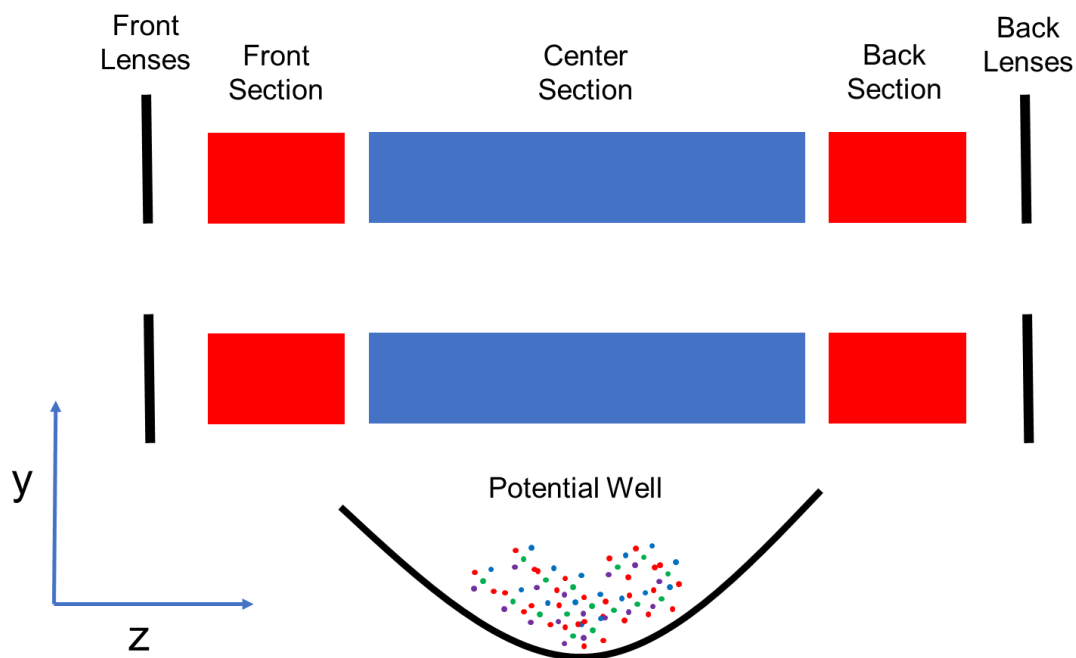


Figure 2.9 A schematic of the LQIT. The ion motion in the z-direction is controlled by applying higher DC potentials to the front and back sections of the LQIT and lower DC potentials to the center section. This creates a DC potential well (shown below) that restricts the ion motion in the z-direction. The colored dots indicate ions trapped in the potential well.

2.5.1.3 Helium as a Buffer Gas

Helium is employed in the LQIT to kinetically cool the ions so that they reside in the center of the central region. Helium reduces the kinetic energy of the ions by frictional cooling without causing collisional activation because it has a low atomic mass (Figure 2.10). This improves detection sensitivity as the cooled ions reside in the center region as a “tight pack” and can be ejected as a tight pack into the external electron multipliers.

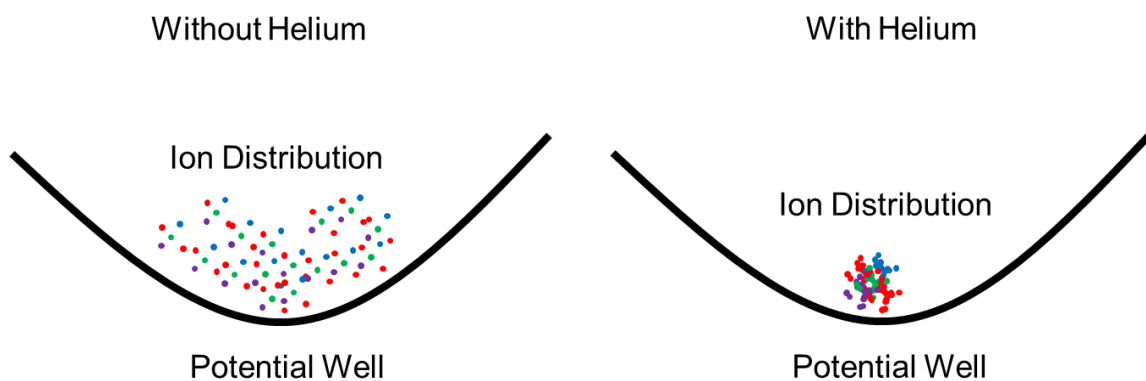


Figure 2.10 The effect of helium on cooling the ions. The cooled ions have less kinetic energy and exist as a tighter group.

2.5.2 Ion Ejection

The ions must be ejected from the ion trap for detection. Ion ejection can be accomplished by a method referred to as “axial instability scan”. This is achieved by increasing the q value of the ions by increasing the RF amplitude. As the ion q value increases to 0.908 (Figure 2.11), the ions no longer have a stable trajectory in the x -direction and they exit the ion trap. However, not all ions exit the ion trap through the slits in the two electrodes. Consequently, sensitivity is compromised.³¹

To address the drawback of axial instability scanning, the ions in commercial LQIT mass spectrometers are ejected via the “ x -electrode bipolar resonance ejection” method.³² This method involves increasing the q value of the ion to 0.88 by increasing the RF amplitude (Figure 2.11). Then, a supplementary RF voltage that is in resonance with the

ion's oscillation frequency is applied to the x-electrodes. The ion's oscillation frequency is described by the following equation:

$$\omega_{\mu} = \frac{\beta_{\mu}\Omega}{2} \quad (2.10)$$

where Ω is the angular frequency of the RF field applied to the electrodes of the ion trap and β_{μ} is the Dehmelt approximation for the Mathieu stability parameter q_{μ} when q_{μ} is less than 0.4.³³ β_{μ} can be expressed by the following equation:

$$\beta_{\mu} = \sqrt{(\alpha_{\mu} + 0.5q_{\mu}^2)} \quad (2.11)$$

Where α_{μ} and q_{μ} are Mathieu stability parameters described earlier.

The supplementary RF voltage increases the ion kinetic energy and therefore the oscillation amplitude in the x direction. As a result, most of the ejected ions leave the ion trap through the slits in the x-direction electrodes. This approach has better sensitivity and resolution compared to ion ejection via axial instability scanning.³⁴

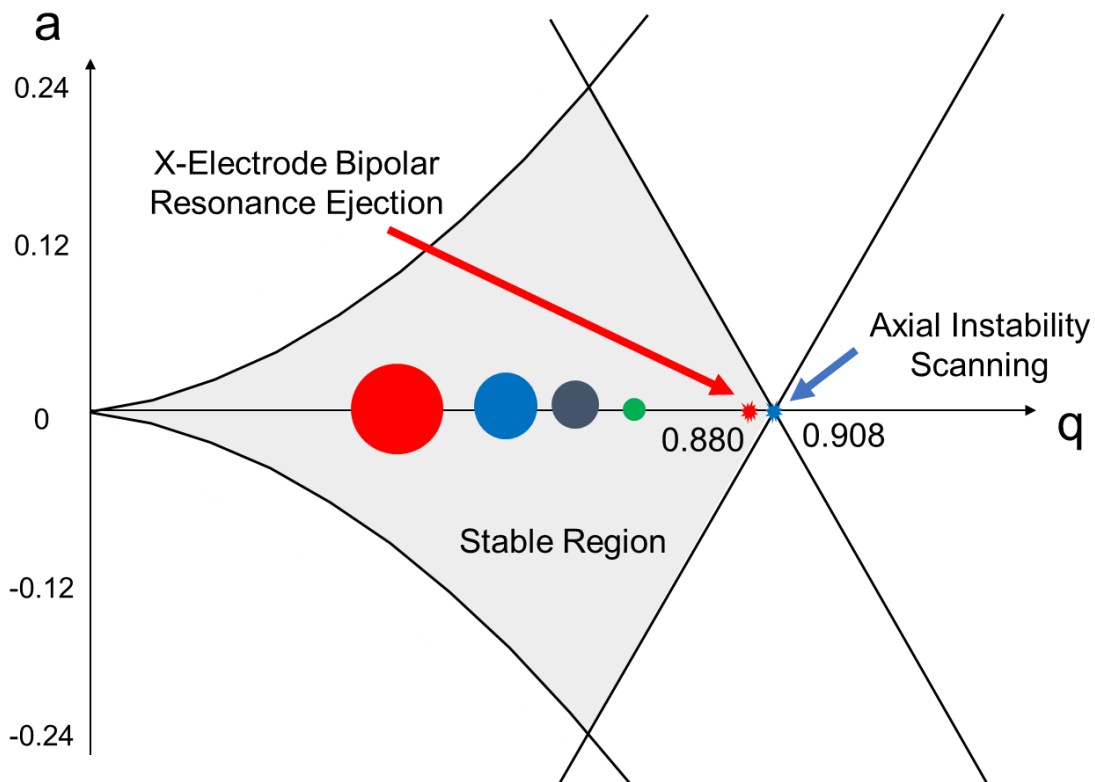


Figure 2.11 Mathieu stability diagram. In axial instability scanning figure, ions are ejected at $q = 0.908$. In x-electrode bipolar resonance ejection, the q value of the ions is increased to 0.88 and a supplemental RF voltage is applied to eject the ions.

2.5.3 Ion Detection with Electron Multipliers

Ion detection can be achieved through two electron multipliers (Figure 2.12) located in the x-direction on both sides of the ion trap. A voltage is applied to a conversion dynode located near the slit in an x-electrode to attract ions towards the dynode. The ions collide with the surface of the conversion dynode and generate electrons.³⁵ The electrons then travel towards the electron multiplier due to the electric potential difference between the conversion dynode and the electron multiplier. The electrons collide with the surface of the electron multiplier and generate several electrons. The surface of the cathode in the electron multiplier is funnel-shaped. This results in a cascade of collisions for each electron generated by the secondary particles. Upon collisions with the surface, these electrons generate many more electrons. The number of electrons generated upon each collision is controlled by the amplification factor (gain). As a result, for each analyte ion that strikes the conversion dynode, a very large number of electrons is generated in the electron multiplier, creating a measurable electric current that is proportional to the numbers of ions ejected from the LQIT. The measured electric current is reported as the relative abundance of the ejected ions.

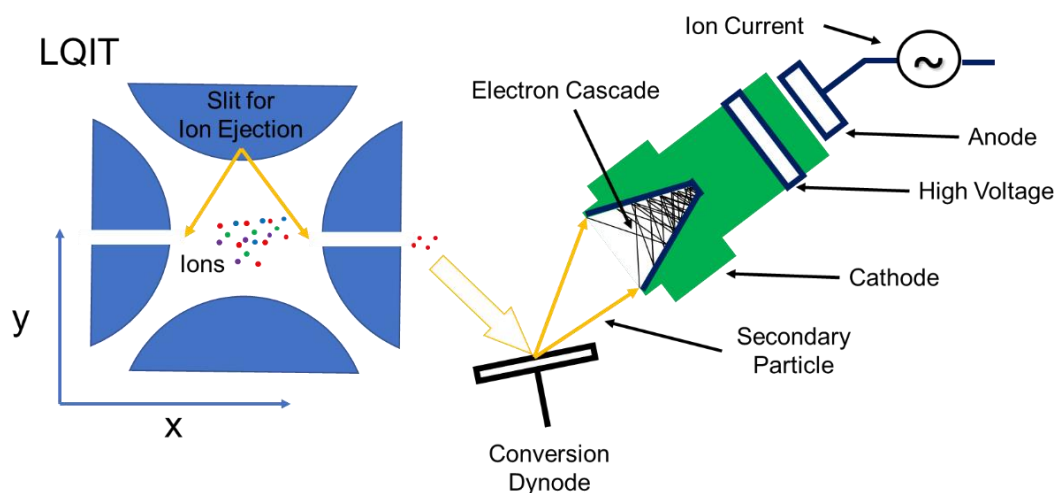


Figure 2.12 A schematic of ion detection by using electron multipliers in an LQIT.

2.6 Fundamental Aspects of Tandem Mass Spectrometry (MS/MS)

Tandem mass spectrometry (MS/MS) experiments are often employed for structural elucidation of unknown ions. In these experiments, the ions of interest are first isolated by ejecting unwanted ions from the ion trap and then subjected to reactions. Collision-activated dissociation (CAD) is one of the most commonly used reactions in tandem mass spectrometry experiments and can be performed in the LQIT-orbitrap mass spectrometer used in the studies discussed in this thesis. These events are discussed in detail below.

2.6.1 Ion Isolation

The first step in a typical MS/MS experiment is isolation of the ions of interest by ejection of all other ions. Ions with m/z values lower than that of the ions of interest are ejected by increasing the RF voltage amplitude, thus increasing the q values of the ions to 0.803. This destabilizes the trajectories of the smaller ions, ejecting them from the trap (Figure 2.13). After this, the ions with m/z -values larger than that of the ions of interest are ejected by applying a broad-band excitation waveform to the x -electrodes at all oscillatory frequencies (5-500 kHz, all q values) except for the frequency of the ions of interest at $q = 0.803$. This increases the oscillatory amplitude of all ions except for the ions of interest in the x -direction. As a result, all ions except the ions of interest are ejected from the ion trap.

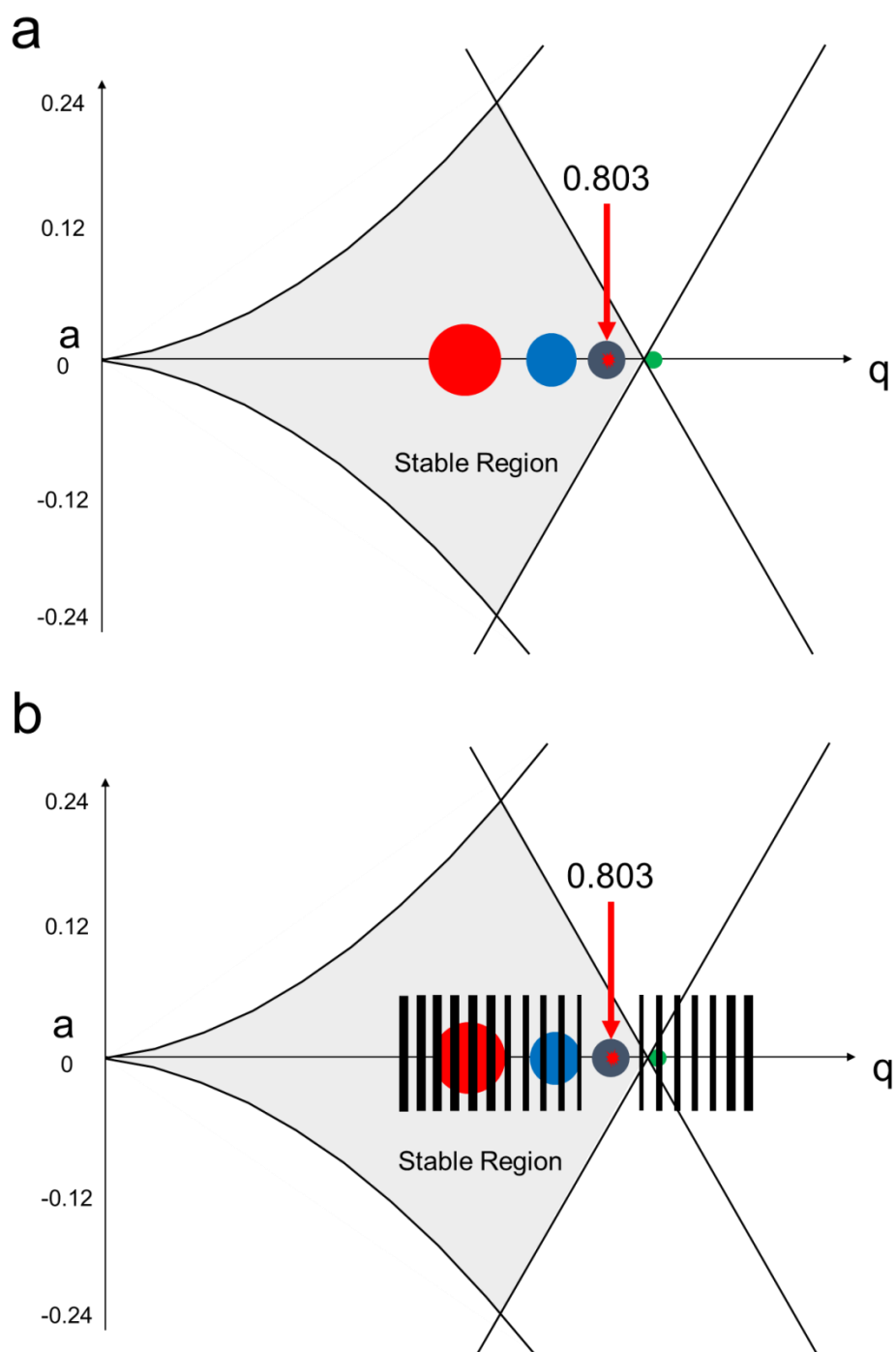


Figure 2.13 a) The q value of the ion of interest is increased to 0.803. The ions of lower m/z values than the ions of interest are ejected from the ion trap. b) Application of a tailored broadband waveform results in the ejection of ions of greater m/z values than that of the ions of interest.

2.6.2 Collision-Activated Dissociation

After the ions of interest have been isolated, they can be activated by CAD in the instrument employed in this research. Three different types of CAD experiments can be performed in different regions of the Thermo LTQ-Orbitrap XL mass spectrometer (Figure 2.14): ion-source CAD (ISCAD), ion trap CAD (ITCAD), and medium-energy CAD (MCAD, commercially known as higher-energy collision dissociation). In the research discussed in this thesis, all three CAD techniques were employed. Each CAD technique has its unique advantages and thus unique potential applications.

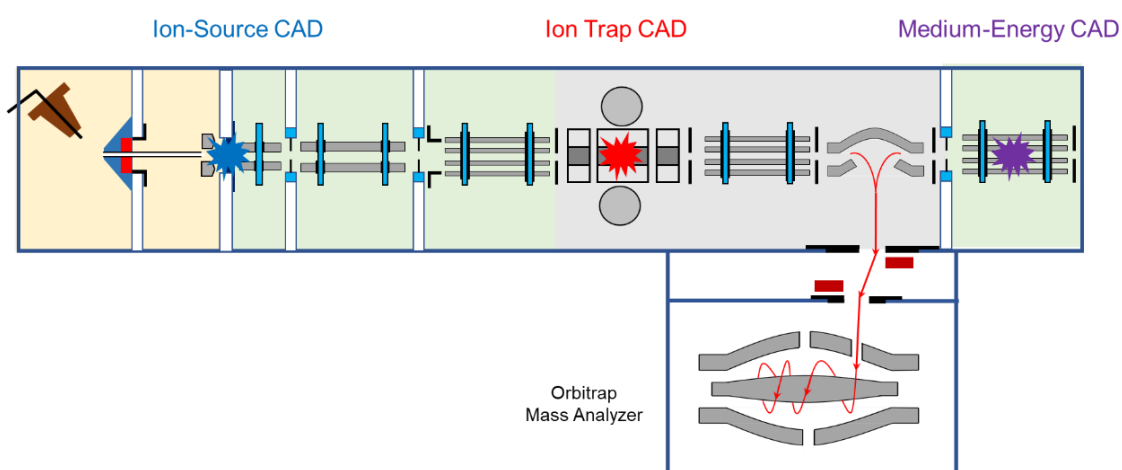


Figure 2.14 The three different types of CAD techniques available in the commercial Thermo LTQ-Orbitrap XL mass spectrometer. Ion-source CAD occurs near the tube lens region in the ion source. Ion trap CAD occurs in the LQIT. Medium-energy CAD occurs in the multipole collision cell located behind the C-trap.

2.6.2.1 Ion-Trap CAD (ITCAD)

In ITCAD, the ions of interest are first isolated in the ion trap as discussed above. Then the isolated ions are accelerated and undergo activating collisions with the helium buffer gas. Part of the kinetic energy of the ions is converted into internal energy during the collisions, which results in ion fragmentation.³⁶ The overall instrumental aspect of the ITCAD process is illustrated in Figure 2.15.

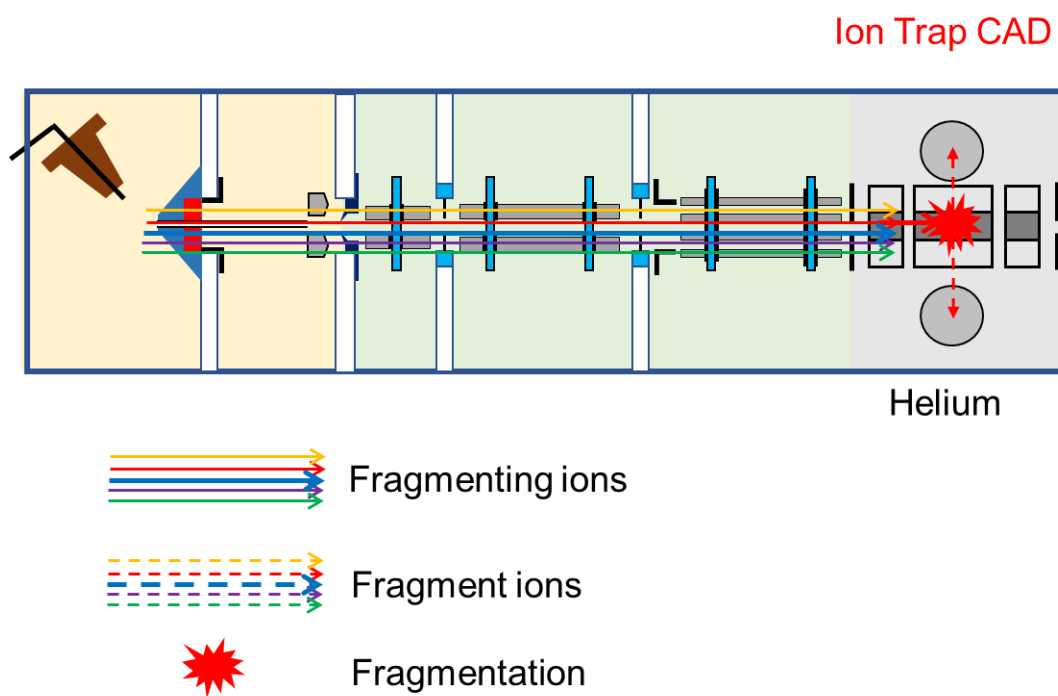


Figure 2.15 Schematic of ITCAD in the Thermo LTQ-Orbitrap XL mass spectrometer. The ions of interest are first isolated in the LQIT. The isolated ions are accelerated and undergo activating collisions with the helium buffer gas. The fragmenting ions are indicated by solid lines and the fragment ions are indicated using dashed lines.

In the LQIT, ion activation usually starts by decreasing the RF amplitude until the q value of the isolated ions is decreased to 0.25. Then, the isolated ions are accelerated by applying a supplementary RF voltage to the x-electrodes. The supplementary voltage has a small amplitude and a frequency equal to the ion resonance frequency. This pulse is typically applied for a user-defined time (typically 30 milliseconds). The accelerated ions collide with helium in the ion trap. During the collisions, part of the ion kinetic energy is converted into internal energy until the energy barrier for fragmentation is overcome and fragmentation ensues. Figure 2.16 illustrates the ITCAD process in the Mathieu stability diagram.

In ITCAD, only the ions of interest (fragmenting ions) are activated because the supplementary voltage has the same frequency as the fragmenting ions. Therefore, the fragment ions are not accelerated. The collisions between the fragmenting ions and helium atoms are not efficient in converting the ion kinetic energy into internal energy. Therefore, the increase in the ion internal energy during ITCAD is a slow process and the fragment ions are mainly generated via low-energy fragmentation pathways.

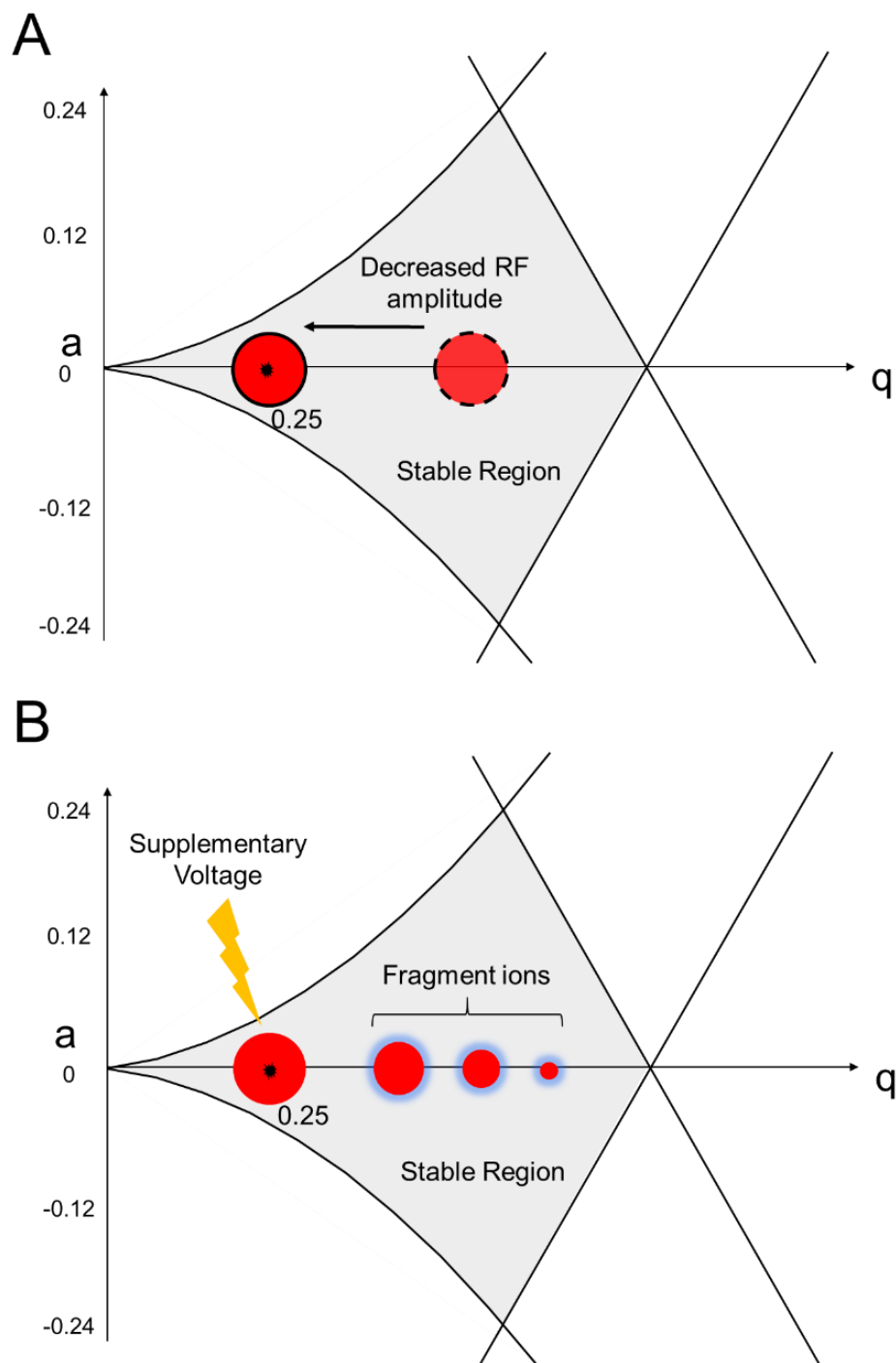


Figure 2.16 Schematic of the ITCAD process. A) The q -value of the isolated ions is reduced to 0.25 by decreasing the RF amplitude. B) A supplementary RF voltage with the same frequency as that of the ions is applied to the x -electrode to increase the kinetic energy of the ions. Fragment ions are produced upon collisions between the accelerated ions with helium buffer gas.

2.6.2.2 Ion-Source CAD (ISCAD)

ISCAD was initially developed to de-cluster ionized proteins in triple-quadrupole mass spectrometers.³⁷ In the experiments described in this thesis, ISCAD was performed in the ion source region of the mass spectrometer. The instrumental aspects of ISCAD and the DC voltages for normal ion transfer and for ISCAD are shown in Figure 2.17. During ISCAD, all ions were accelerated by the same supplementary DC voltage (Figure 2.17 top, ISCAD DC voltage) applied to the orifice located in the ion source region (indicated by an arrow). High-purity nitrogen gas is normally used as sheath and auxiliary gases in the Thermo LQIT/Orbitrap XL mass spectrometer. Therefore, the orifice region is filled with high purity nitrogen gas in the experiments discussed in this thesis. The accelerated ions collided with the nitrogen molecules present in the orifice region inside the ion source before being transferred to the LQIT. It needs to be highlighted that during ISCAD, ions are fragmented before being transferred to the LQIT (Figure 2.17) and hence no ion isolation is involved during ISCAD.

ITCAD and ISCAD have several major differences. The collisions between the ions and nitrogen molecules more efficiently convert the ion kinetic energy into internal energy. This makes ISCAD a “harder” fragmentation method than ITCAD, resulting in fragment ions derived from higher-energy fragmentation pathways. In addition, as discussed above, fragmenting ions are not isolated prior to fragmentation during ISCAD, and thus all ions formed in the ion source are activated and dissociate.

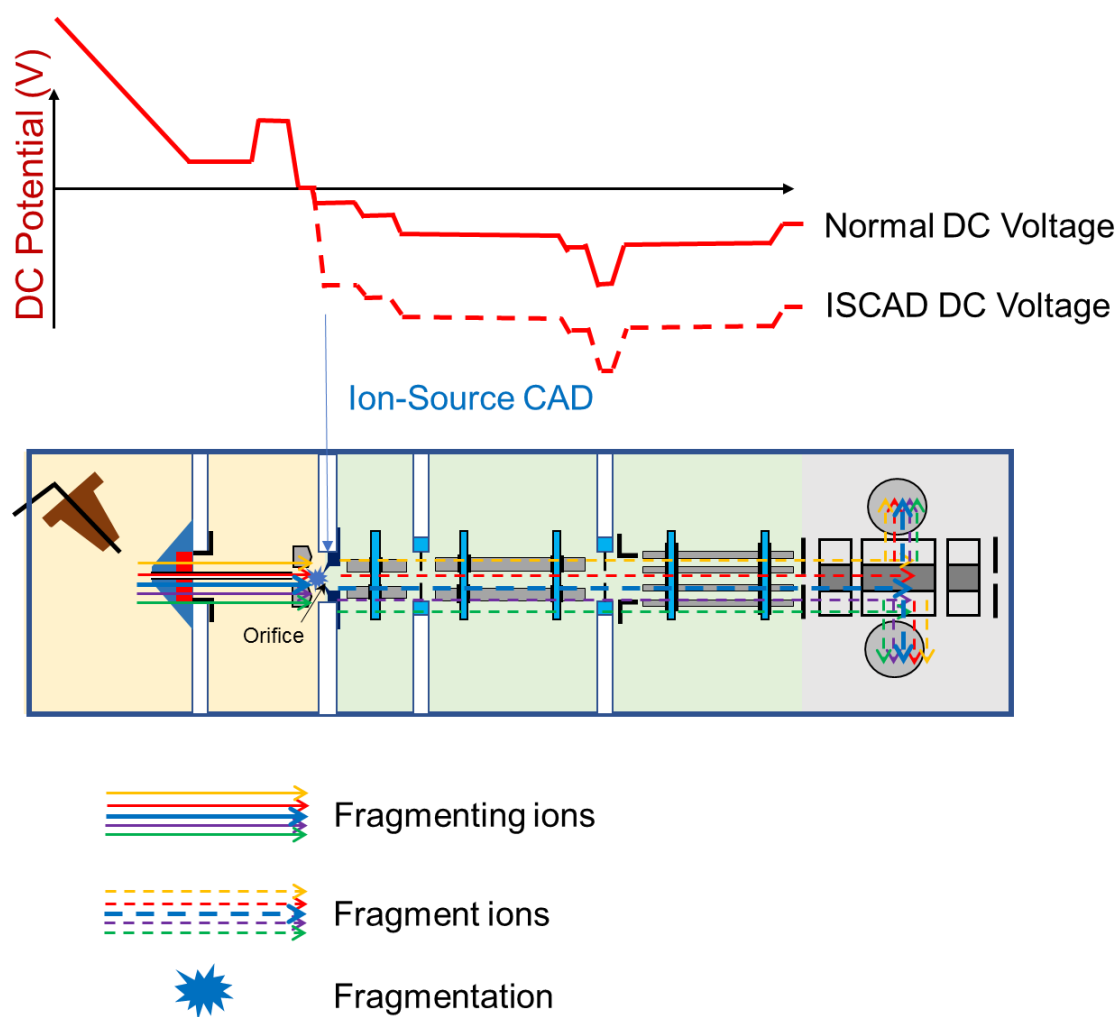


Figure 2.17 Schematic of ITCAD in the Thermo LTQ-Orbitrap XL mass spectrometer. A decrease in the DC voltage accelerates ions in the ion source region where they collide with nitrogen molecules. The fragmenting ions are indicated by solid lines and the fragment ions are indicated by dashed lines. The normal DC voltages and the ion-source CAD DC voltages are shown as solid and dashed lines, respectively.

2.7 Fundamental Aspects of the Orbitrap Mass Analyzer

The orbitrap mass analyzer was developed by Alexander Makarov at Thermo Fisher Scientific in 2000.³⁸ This mass analyzer is based on an earlier ion trap developed by Kingdon,³⁹ which is composed of a metal wire stretched along the axis of a cylindrical electrode. This device is only capable of storing ions, not analyzing them. The orbitrap is composed of an inner spindle-shaped electrode positioned along the axis of an outer barrel-shaped electrode.⁴⁰ The orbitrap can both store ions and determine their m/z values at relatively high resolution.⁴⁰ A schematic of a commercial hybrid mass spectrometer, the Thermo Scientific LTQ Orbitrap XL, is shown in Figure 2.18. The LQIT part of the instrument is operated as discussed above. The operation of the C-trap, orbitrap and octupole collision cell are discussed in detail below.

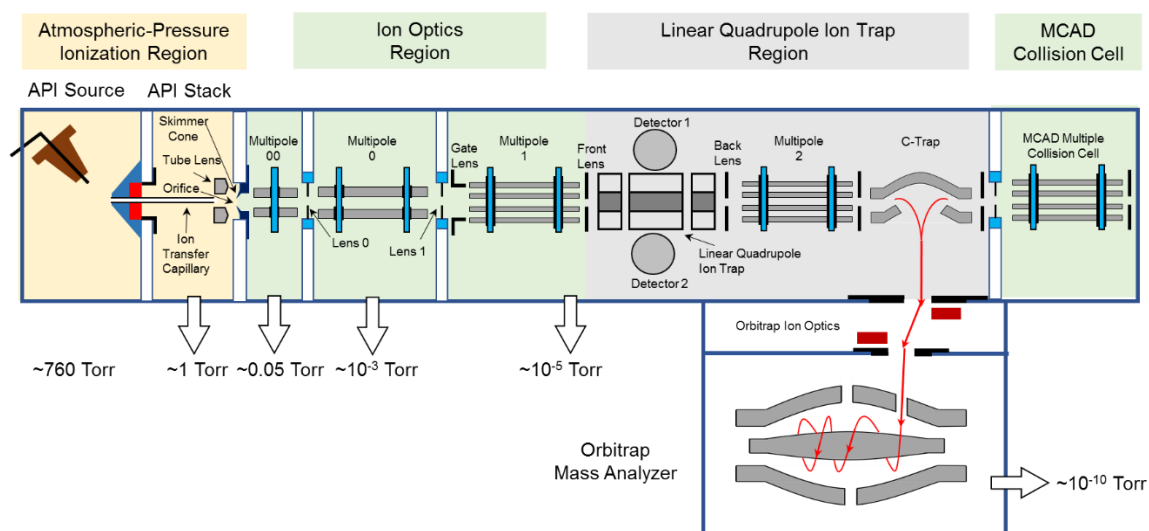


Figure 2.18 A schematic of a Thermo Scientific LTQ Orbitrap XL mass spectrometer. The red lines indicate ion trajectories during injection from the C-trap into the orbitrap.

2.7.1 C-Trap

A C-trap is employed to eject ions into the orbitrap as a cohesive packet to obtain high-resolution measurements. In the LQIT orbitrap mass spectrometer illustrated in Figure 2.18, the ions isolated in the LQIT are first delivered into the C-trap, which is filled with nitrogen gas to kinetically cool the ions via collisions. Nitrogen is employed as the buffer gas because collisions with the larger nitrogen molecules can more efficiently cool the ions compared to the smaller helium atoms used in the linear quadrupole ion trap.⁴¹ After ions are transferred into the C-trap, a high DC voltage is applied to the C-trap which ejects the ions as a spatially and temporally tight packet. In the Thermo LQIT orbitrap mass spectrometer employed here, the ion beam traveling from the C-trap into the orbitrap is deflected by a set of transfer lenses to prevent the nitrogen gas in the C-trap from entering the orbitrap. The ions are injected off-center into the orbitrap to allow the ions to start axial oscillations immediately after entering the orbitrap.⁴² The overall ion injection process is illustrated in Figure 2.19.

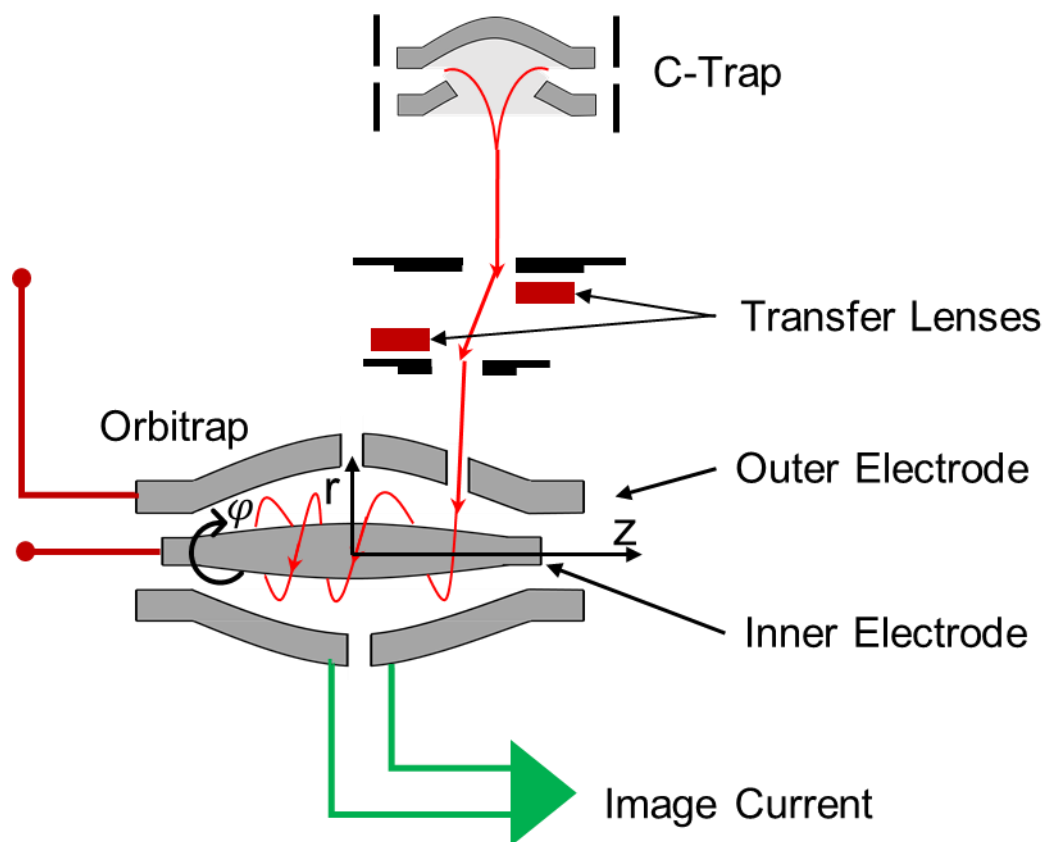


Figure 2.19 Injection of ions from the C-trap into the orbitrap. The red arrows indicate ion trajectories. The image current is produced due to the axial oscillation of the ions. The cylindrical coordinates r , z , and φ are indicated in the orbitrap.

2.7.2 Ion Motion in the Orbitrap

To achieve the desired cycling motion of ions along and around the inner electrode in the orbitrap without collisions with the electrodes, the electric field in the orbitrap needs to have a quadro-logarithmic distribution, U .⁴⁰ The electric field, U , can be described as shown in equation 2.12:

$$U_{(r,z)} = \frac{k}{2} \left(z^2 - \frac{r^2}{2} \right) + \frac{k}{2} (R_m)^2 \ln\left(\frac{r}{R_m}\right) + C \quad (2.12)$$

where r and z are the cylindrical coordinates indicated in Figure 2.19, k is a term related to the field curvature, R_m is the characteristic radius of the orbiting trajectory of an ion, and C is a constant.

The ions have three motions in the orbitrap, each with a specific frequency: ion rotation around the inner electrode (frequency ω_ϕ), ion oscillation in the radial direction (frequency ω_r) and ion oscillation along the axial direction (frequency ω_z). The motions in the orbitrap coordinates (ϕ, r, z) for an ion of mass m and charge q can be expressed as follows:

$$\frac{\partial^2 r}{\partial t^2} - r \left(\frac{\partial \phi}{\partial t} \right) = -\frac{qk}{2m} \left(\frac{R_m^2}{r} - r \right) \quad (2.13)$$

$$\frac{d}{dt} \left(r^2 \frac{\partial \phi}{\partial t} \right) = 0 \quad (2.14)$$

$$\frac{\partial^2 z}{\partial t^2} = -kz \frac{q}{m} \quad (2.15)$$

As shown in above equations, only the axial frequency ω_z (equation 2.15) is related to the m/z ratio of the ion and is independent of the position and kinetic energy of the ion. Consequently, out of the three frequencies (ω_ϕ , ω_r , and ω_z), only the axial frequency ω_z can be used to determine the ion mass-to-charge ratio in the orbitrap. The axial frequency can be expressed by the following equation:

$$\omega_z = \sqrt{\left(\frac{q}{m}\right)k} \quad (2.16)$$

where k is a constant that is derived from equation 2.15 and is proportional to the voltage applied between the two electrodes.

2.7.3 Ion Detection in the Orbitrap

As previously discussed, only the frequencies in the axial direction are related to the ions' mass to charge ratio. Therefore, only the image current produced by the ion motion in the axial direction is measured. The measured image current is Fourier transformed to obtain the ions' m/z values.⁴³ Unlike the LQIT, the orbitrap is a non-destructive mass analyzer. In the orbitrap, high mass resolution is achieved by simply measuring the frequency for longer periods of time.⁴⁴

2.7.4 Medium-Energy CAD (MCAD)

In a Thermo LQIT-Orbitrap mass spectrometer, medium-energy CAD (MCAD, commercially known as higher-energy collision dissociation) is performed in the octopole collision cell located behind the C-trap.⁴⁵ The octopole collision cell is typically filled with nitrogen as the collision gas. The schematic for the MCAD process is illustrated in Figure 2.20.

During MCAD, the ions of interest are first isolated in the quadrupole ion trap as discussed above and then transferred into the C-trap. The ions are then accelerated into the octopole collision cell by a supplementary DC voltage. The collision energy is determined by the voltage difference between the C-trap (0 V) and the octopole (-10 V ~ -250 V). The ions are fragmented upon collisions with nitrogen gas in the octopole collision cell. The fragment ions are trapped in the octopole by a DC potential well before being transferred back into the C-trap by increasing the DC voltage of the octopole. Typical DC potentials employed in MCAD experiments are shown in Figure 2.20 (top).

MCAD is a beam-type fragmentation method and thus the generated fragment ions can be further fragmented during MCAD. In addition, the collisions between the fragmenting ions and nitrogen gas more efficiently convert the ion kinetic energy into internal energy compared to collisions with helium in the linear quadrupole ion trap. As a result, fragment ions from both low- and high-energy fragmentation pathways can be observed upon MCAD.

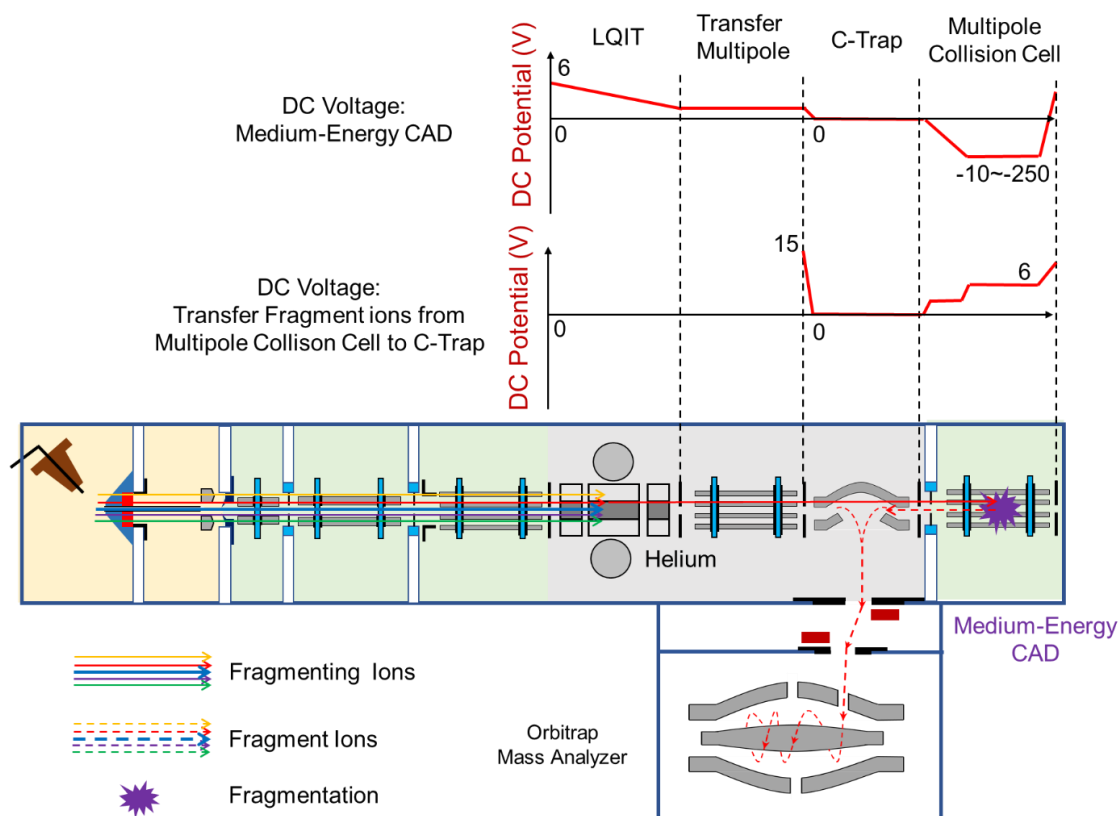


Figure 2.20 Schematic of the MCAD process in a Thermo LTQ-Orbitrap XL mass spectrometer. The ions of interest are isolated in the LQIT and then transported into the octopole collision cell. The ions are accelerated using a supplementary DC voltage and then collide with nitrogen in the octopole.

2.8 References

- (1) Dempster, A. A New Method of Positive Ray Analysis. *Phys. Rev.* **1918**, *11*, 316.
- (2) Fales, H.; Milne, G.; Pisano, J.; Brewer Jr, H.; Blum, M.; MacConnell, J.; Brand, J.; Law, N. Biological Applications of Electron Ionization and Chemical Ionization Mass Spectrometry. *Recent Prog. Horm. Res.* **1972**, *28*, 591.
- (3) Barber, M.; Bordoli, R. S.; Sedgwick, R. D.; Tyler, A. N. Fast Atom Bombardment of Solids (Fab): A New Ion Source for Mass Spectrometry. *ChemComm.* **1981**, 325-327.
- (4) Beckey, H. Field Desorption Mass Spectrometry: A Technique for the Study of Thermally Unstable Substances of Low Volatility. *Int. J. Mass Spectrom. Ion Physic.* **1969**, *2*, 500-502.
- (5) Gomer, R.; Inghram, M. G. Applications of Field Ionization to Mass Spectrometry. *J. Am. Chem. Soc.* **1955**, *77*, 500-500.
- (6) Fenn, J. B.; Mann, M.; Meng, C. K.; Wong, S. F.; Whitehouse, C. M. Electrospray Ionization for Mass Spectrometry of Large Biomolecules. *Science.* **1989**, *246*, 64-71.
- (7) Karas, M.; Bachmann, D.; Hillenkamp, F. Influence of the Wavelength in High-Irradiance Ultraviolet Laser Desorption Mass Spectrometry of Organic Molecules. *Anal. Chem.* **1985**, *57*, 2935-2939.
- (8) Carroll, D.; Dzidic, I.; Stillwell, R.; Haegele, K.; Horning, E. Atmospheric Pressure Ionization Mass Spectrometry. Corona Discharge Ion Source for Use in a Liquid Chromatograph-Mass Spectrometer-Computer Analytical System. *Anal. Chem.* **1975**, *47*, 2369-2373.
- (9) Robb, D. B.; Covey, T. R.; Bruins, A. P. Atmospheric Pressure Photoionization: An Ionization Method for Liquid Chromatography- Mass Spectrometry. *Anal. Chem.* **2000**, *72*, 3653-3659.
- (10) Takats, Z.; Wiseman, J. M.; Gologan, B.; Cooks, R. G. Mass Spectrometry Sampling under Ambient Conditions with Desorption Electrospray Ionization. *Science.* **2004**, *306*, 471-473.
- (11) Cotte-Rodríguez, I.; Takáts, Z.; Talaty, N.; Chen, H.; Cooks, R. G. Desorption Electrospray Ionization of Explosives on Surfaces: Sensitivity and Selectivity Enhancement by Reactive Desorption Electrospray Ionization. *Anal. Chem.* **2005**, *77*, 6755-6764.

- (12) Cody, R. B.; Laramée, J. A.; Durst, H. D. Versatile New Ion Source for the Analysis of Materials in Open Air under Ambient Conditions. *Anal. Chem.* **2005**, *77*, 2297-2302.
- (13) Fenn, J. Electrospray Ionization Mass Spectrometry: How It All Began. *J. Biomol. Tech.* **2002**, *13*, 101.
- (14) Yamashita, M.; Fenn, J. B. Electrospray Ion Source. Another Variation on the Free-Jet Theme. *J. Phys. Chem.* **1984**, *88*, 4451-4459.
- (15) Taylor, G. I. Disintegration of Water Drops in an Electric Field. *Proc. Royal Soc. Lond.* **1964**, *280*, 383-397.
- (16) Taylor, G. I. The Force Exerted by an Electric Field on a Long Cylindrical Conductor. *Proc. Royal Soc. Lond.* **1966**, *291*, 145-158.
- (17) Rayleigh, L. Xx. On the Equilibrium of Liquid Conducting Masses Charged with Electricity. *Philos. Mag.* **1882**, *14*, 184-186.
- (18) Gomez, A.; Tang, K. Charge and Fission of Droplets in Electrostatic Sprays. *Phys. Fluids.* **1994**, *6*, 404-414.
- (19) Bruins, A. P.; Covey, T. R.; Henion, J. D. Ion Spray Interface for Combined Liquid Chromatography/Atmospheric Pressure Ionization Mass Spectrometry. *Anal. Chem.* **1987**, *59*, 2642-2646.
- (20) Gatlin, C. L.; Kleemann, G. R.; Hays, L. G.; Link, A. J.; Yates III, J. R. Protein Identification at the Low Femtomole Level from Silver-Stained Gels Using a New Fritless Electrospray Interface for Liquid Chromatography-Microspray and Nanospray Mass Spectrometry. *Anal. Biochem.* **1998**, *263*, 93-101.
- (21) Kebarle, P.; Peschke, M. On the Mechanisms by Which the Charged Droplets Produced by Electrospray Lead to Gas Phase Ions. *Anal. Chim. Acta.* **2000**, *406*, 11-35.
- (22) Kebarle, P.; Tang, L. From Ions in Solution to Ions in the Gas Phase-the Mechanism of Electrospray Mass Spectrometry. *Anal. Chem.* **1993**, *65*, 972A-986A.
- (23) Cole, R. B. Some Tenets Pertaining to Electrospray Ionization Mass Spectrometry. *Int. J. Mass Spectrom.* **2000**, *35*, 763-772.
- (24) Cech, N. B.; Enke, C. G. Practical Implications of Some Recent Studies in Electrospray Ionization Fundamentals. *Mass Spectrom. Rev.* **2001**, *20*, 362-387.
- (25) Nguyen, S.; Fenn, J. B. Gas-Phase Ions of Solute Species from Charged Droplets of Solutions. *Proc. Natl. Acad. Sci.* **2007**, *104*, 1111-1117.

- (26) Iribarne, J.; Thomson, B. On the Evaporation of Small Ions from Charged Droplets. *J. Chem. Phys.* **1976**, *64*, 2287-2294.
- (27) Fenn, J. B.; Mann, M.; Meng, C. K.; Wong, S. F.; Whitehouse, C. M. Electrospray Ionization—Principles and Practice. *Mass Spectrom. Rev.* **1990**, *9*, 37-70.
- (28) Konermann, L.; Ahadi, E.; Rodriguez, A. D.; Vahidi, S.; ACS Publications, 2012.
- (29) Schwartz, J. C.; Senko, M. W.; Syka, J. E. A Two-Dimensional Quadrupole Ion Trap Mass Spectrometer. *J. Am. Soc. Mass Spectrom.* **2002**, *13*, 659-669.
- (30) March, R. E. An Introduction to Quadrupole Ion Trap Mass Spectrometry. *Int. J. Mass Spectrom.* **1997**, *32*, 351-369.
- (31) Kaiser Jr, R. E.; Cooks, R. G.; Stafford Jr, G. C.; Syka, J. E.; Hemberger, P. H. Operation of a Quadrupole Ion Trap Mass Spectrometer to Achieve High Mass/Charge Ratios. *Int. J. Mass Spectrom. Ion Process.* **1991**, *106*, 79-115.
- (32) Stafford Jr, G.; Kelley, P.; Syka, J.; Reynolds, W.; Todd, J. Recent Improvements in and Analytical Applications of Advanced Ion Trap Technology. *Int. J. Mass Spectrom. Ion Process.* **1984**, *60*, 85-98.
- (33) Douglas, D. Linear Quadrupoles in Mass Spectrometry. *Mass Spectrom. Rev.* **2009**, *28*, 937-960.
- (34) Schwartz, J. C.; Syka, J. E.; Jardine, I. High Resolution on a Quadrupole Ion Trap Mass Spectrometer. *J. Am. Soc. Mass Spectrom.* **1991**, *2*, 198-204.
- (35) Stanton, H. E.; Chupka, W. A.; Inghram, M. G. Electron Multipliers in Mass Spectrometry; Effect of Molecular Structure. *Rev. Sci. Instrum.* **1956**, *27*, 109-109.
- (36) McLuckey, S. A. Principles of Collisional Activation in Analytical Mass Spectrometry. *J. Am. Soc. Mass Spectrom.* **1992**, *3*, 599-614.
- (37) Thomson, B. A. Declustering and Fragmentation of Protein Ions from an Electrospray Ion Source. *J. Am. Soc. Mass Spectrom.* **1997**, *8*, 1053-1058.
- (38) Makarov, A.; Hardman, M. E.; Schwartz, J. C.; Senko, M. W.; Google Patents, 2005.
- (39) Kingdon, K. A Method for the Neutralization of Electron Space Charge by Positive Ionization at Very Low Gas Pressures. *Phys. Rev.* **1923**, *21*, 408.
- (40) Makarov, A. Electrostatic Axially Harmonic Orbital Trapping: A High-Performance Technique of Mass Analysis. *Anal. Chem.* **2000**, *72*, 1156-1162.
- (41) Makarov, A.; Denisov, E.; Kholomeev, A.; Balschun, W.; Lange, O.; Strupat, K.; Horning, S. Performance Evaluation of a Hybrid Linear Ion Trap/Orbitrap Mass Spectrometer. *Anal. Chem.* **2006**, *78*, 2113-2120.

- (42) Perry, R. H.; Cooks, R. G.; Noll, R. J. Orbitrap Mass Spectrometry: Instrumentation, Ion Motion and Applications. *Mass Spectrom. Rev.* **2008**, *27*, 661-699.
- (43) Hu, Q.; Noll, R. J.; Li, H.; Makarov, A.; Hardman, M.; Graham Cooks, R. The Orbitrap: A New Mass Spectrometer. *Int. J. Mass Spectrom.* **2005**, *40*, 430-443.
- (44) Badman, E. R.; Patterson, G. E.; Wells, J. M.; Santini, R. E.; Cooks, R. G. Differential Non-Destructive Image Current Detection in a Fourier Transform Quadrupole Ion Trap. *Int. J. Mass Spectrom.* **1999**, *34*, 889-894.
- (45) Olsen, J. V.; Macek, B.; Lange, O.; Makarov, A.; Horning, S.; Mann, M. Higher-Energy C-Trap Dissociation for Peptide Modification Analysis. *Nat. Methods.* **2007**, *4*, 709.

CHAPTER 3. DEVELOPING TANDEM MASS SPECTROMETRY METHODS TO ADDRESS SAMPLING BIASES FOR DETERMINING THE RELATIVE ABUNDANCES OF SINGLE-CORE AND MULTICORE COMPOUNDS IN ASPHALTENES

3.1 Introduction

Asphaltenes are the heaviest compounds in crude oil defined by their solubility in toluene and insolubility in n-alkanes.¹ Currently, heavy petroleum feedstocks are increasingly used in the petroleum industry because light crude oil reserves are being exhausted.¹ These heavier feed stocks usually contain high levels of asphaltenes, meaning that asphaltenes are becoming increasingly important in the petroleum industry.¹ Unfortunately, asphaltenes have limited economical uses beyond road paving. Furthermore, asphaltenes cause problems for petroleum industries by clogging crude oil transportation pipes and poisoning the catalysts used to upgrade the crude oil.² To better utilize asphaltenes and to alleviate the problems associated with them, it is critical to understand the structures of the compounds in asphaltenes.^{2,3}

Multiple investigations have proposed that the molecular structures of asphaltenes mainly fall into two categories: island (single-core) structures and archipelago (multicore) structures.^{2,4-6} Single-core structures contain a single polyaromatic core with attached alkyl chains, while the multicore structures contain several such units connected by alkyl chains.^{2,4-6} The relative abundance of single-core and multicore compounds in asphaltenes and other petroleum samples is one of the important parameters for accurate compositional modeling predictions of the heavy petroleum upgrading process⁷⁻⁹ However, despite decades of research, no consensus has been reached on the relative abundances of single- and multicore compounds in asphaltenes.¹⁰⁻²⁰

The Yen-Mullins model proposes that single-core compounds predominate in asphaltenes.^{11,12} In agreement, recent studies employing atomic force microscopy and high-resolution transmission electron microscopy have determined the aromatic core structures of a few hundred individual asphaltene molecules whose aromatic core structures suggest that they are single-core compounds.^{21,22} However, this observation cannot explain the formation of aromatic liquids, that cannot be formed from single-core compounds, during

thermal pyrolysis of asphaltenes.^{13,14} Recently, a few studies involving thin-film pyrolysis and high-resolution MS/MS have suggested that the abundances of multicore compounds vary between different asphaltenes and that, while they are likely not the predominant structures in asphaltenes, their abundance can be significant.^{13,14}

High-resolution MS/MS can provide structural information for a large number of individual compounds in asphaltenes, and therefore is arguably the best method for studying asphaltene structures.²³⁻²⁷ During typical high-resolution MS/MS studies, ionized asphaltene samples are isolated and then fragmented by CAD to identify structural characteristics of the isolated ions.²³⁻²⁷ Multiple studies have investigated the fragmentation patterns of ionized asphaltene model compounds via high-resolution MS/MS.^{23,28,29} These studies have provided important information for differentiating single-core and multicore compounds. One of the possible ways to differentiate ionized single-core and multicore compounds is to measure the difference in the RDBE values of the unfragmented fragmenting ions and their respective fragment ions. As illustrated in Figure 3.1, fragmentation of an ionized single-core compound results in losses of alkyl chains and thus a minor change in RDBE values. In contrast, fragmentation of an ionized multicore compound results in losses of aromatic cores and thus a significant decrease in RDBE. This approach has already been employed in studies to determine the relative abundances of single-core and multicore compounds in asphaltenes.^{13,23-27,30,31}

Unfortunately, these studies have generated contradictory and inconclusive results. Several studies have suggested that the abundances of multicore compounds are insignificant while others have suggested that the abundances of multicore compounds can be relatively high.^{13,23-27,30,31} After careful analysis of these studies, it came to my attention that the abundances of the single-core and multicore compounds were determined based on the fragmentation patterns of ions isolated from only one or a few m/z values.^{13,23-27,30-32} Consequently, these studies inevitably assumed that the abundances of single-core and multicore compounds are the same throughout the entire asphaltene sample. This assumption has never been investigated nor validated. Consequently, it is likely that all these studies measured the abundances of single- and multicore compounds in asphaltenes based on biased, non-representative samples.

In this study, eight model compounds and two asphaltene samples were ionized with APCI in the positive ion mode ((+)APCI) with CS₂ as the solvent and APCI reagent to generate stable molecular ions³³ in a LQIT/orbitrap high-resolution mass spectrometer. The structures of the ionized compounds were explored with MCAD and ISCAD.

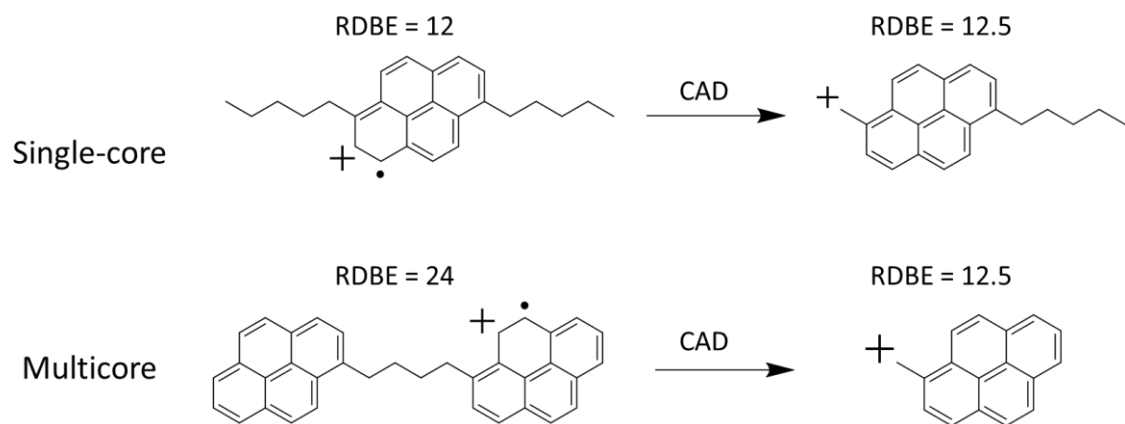


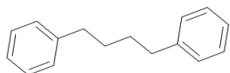
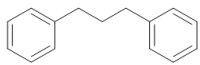
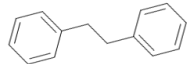
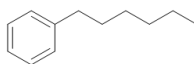
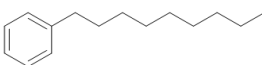
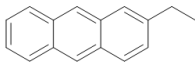
Figure 3.1 Changes in the RDBE values following CAD of an ionized single- and multicore compounds.

3.2 Materials and Methods

3.2.1 Reagents

1,4-Di(pyren-1-yl)butane and 1,6-dipentylpyrene were synthesized according to published protocols.³⁴ n-Nonylbenzene (purity $\geq 96\%$), n-hexylbenzene (purity $\geq 97\%$), 2-ethylanthracene (purity $\geq 98\%$), and 1,2-diphenylethane (purity $\geq 99\%$) were purchased from Sigma Aldrich. 1,4-Diphenylbutane (purity $\geq 96\%$) was purchased from Alfa Chemistry. 1,3-Diphenylpropane (purity $\geq 98\%$) and carbon disulfide (purity $\geq 99\%$) were purchased from Alfa Aesar. All chemicals were used as received. Multi- and single-core model compound solutions were prepared by dissolving 10 mg of 1,4-di(pyren-1-yl)butane or 10 mg of 1,6-dipentylpyrene in 1 mL of CS₂. Five model compound mixtures containing 0 %, 17 %, 50 %, 83 %, and 100 % molar percentages of multicore compounds were prepared by dissolving n-nonylbenzene, n-hexylbenzene, 2-ethylanthracene, 1,2-diphenylethane, 1,3-diphenylpropane, and 1,4-diphenylbutane in CS₂. These mixtures are referred to as 0, 17, 50, 83, and 100 % multicore mixtures, respectively. The molar concentrations of each compound in the model compound mixtures are shown in Table 3.1. The asphaltene sample obtained from ConocoPhillips was generated via residuum oil supercritical extraction (ROSE) from crude oil.³⁵ This sample was reprecipitated in heptane and is referred to herein as the Rose asphaltenes. The other asphaltene sample, Montana asphaltenes, was provided by ConocoPhillips and precipitated in heptane.

Table 3.1 Molar concentrations of model compounds in each mixture.

Model Compound Mixture Name	Molar Concentration (M)				
	100%	83%	50%	17%	0%
	0.06 M	0.05 M	0.03 M	0.01 M	0 M
	0.06 M	0.05 M	0.03 M	0.01 M	0 M
	0.06 M	0.05 M	0.03 M	0.01 M	0 M
	0 M	0.01 M	0.03 M	0.05 M	0.06 M
	0 M	0.01 M	0.03 M	0.05 M	0.06 M
	0 M	0.01 M	0.03 M	0.05 M	0.06 M

3.2.2 Mass Spectrometry

Sample solutions were introduced into a LQIT/orbitrap mass spectrometer (Thermo Scientific) via direct infusion at a flow rate of 5 $\mu\text{L}/\text{min}$. The compounds were ionized via positive ion mode APCI with CS_2 as the ionization reagent to generate stable molecular ions.³³ Nitrogen gas was used as the auxiliary and sheath gas (flow rates set to 5 and 10 arbitrary units, respectively). The vaporizer and capillary temperatures were set to 300 $^\circ\text{C}$ and 275 $^\circ\text{C}$, respectively. Ionized model compounds as well as ions of m/z 350 ± 10 , 450 ± 10 , 550 ± 10 , and 650 ± 10 from the asphaltene samples were isolated in the linear quadrupole ion trap for MCAD in the octopole collision cell located behind the C-trap. Because larger ions require more internal energy to fragment at an equal extent compared to smaller ions, greater collision energies were employed for larger ions. The ionized model compound mixtures (Table 3.2, MW ~ 200 Da) were fragmented at collision energies ranging from 0 - 20 eV at 3 eV intervals. The ionized model compounds 1,6-dipentylpyrene (MW 342 Da) and 1,4-di(pyren-1-yl)butane (MW 458 Da) were fragmented at a collision energy of ~ 40

eV. The ions from the asphaltene samples (m/z 350 ± 10 , 450 ± 10 , 550 ± 10 , and 650 ± 10) were fragmented at collision energies ranging from 0 - 60 eV at 10 eV intervals. All ions were also subjected to ISCAD at nominal collision energies ranging from 0 - 60 eV at 10 eV intervals. All ions were detected with the high-resolution orbitrap mass analyzer at a resolution of 100,000 or with two electron multipliers at unit resolution. RDBE values were obtained using Thermo XcaliburTM Software, and RDBE plots were generated with Origin Software.

3.3 Results and Discussion

3.3.1 Statistical Considerations for Sampling in MS/MS Analysis of Asphaltenes

Asphaltenes are composed of tens of thousands of different compounds and are arguably one of the most complicated known mixtures.^{36,37} As a result, in an ionized asphaltene sample, ions with the same nominal mass are composed of different numbers of isobaric and isomeric ions.^{36,37} This suggests that isolating the ions of interest in the MS/MS analysis of asphaltenes should be statistically considered cluster sampling with different cluster sizes. This sampling method is highly susceptible to sampling errors.³⁸ The most common way to address these errors is to include a sufficient number of samples and to carefully design the sampling method.³⁸

High-resolution Fourier transform ion cyclotron resonance MS analysis of ionized asphaltenes has previously identified the elemental compositions of as many as 100,000 compounds.^{36,37} Adding to the complexity, the compounds with a given elemental composition may have isomeric structures, increasing the number of compounds to substantially larger than 100,000. According to the principles of population sampling, to achieve a representative sampling of an asphaltene containing 100,000 compounds at a ~99% confidence level and ~1% confidence interval, at least 16,000 different compounds must be sampled. The APCI(+) CS₂ mass spectra measured for Rose and Montana asphaltenes suggests that the compounds in both asphaltene samples have a MW distribution ranging from approximately 200 -700 Da (Figure 3.2). Assuming that both Rose and Montana contain 100,000 compounds within their MW distribution ranges, each isolated m/z value corresponds to ~200 compounds. Thus, several groups of molecular ions (i.e., ions of m/z

350±10, 450±10, 550±10 and 650±10) from each ionized asphaltene sample were investigated to study a total of roughly 16,000 ions.

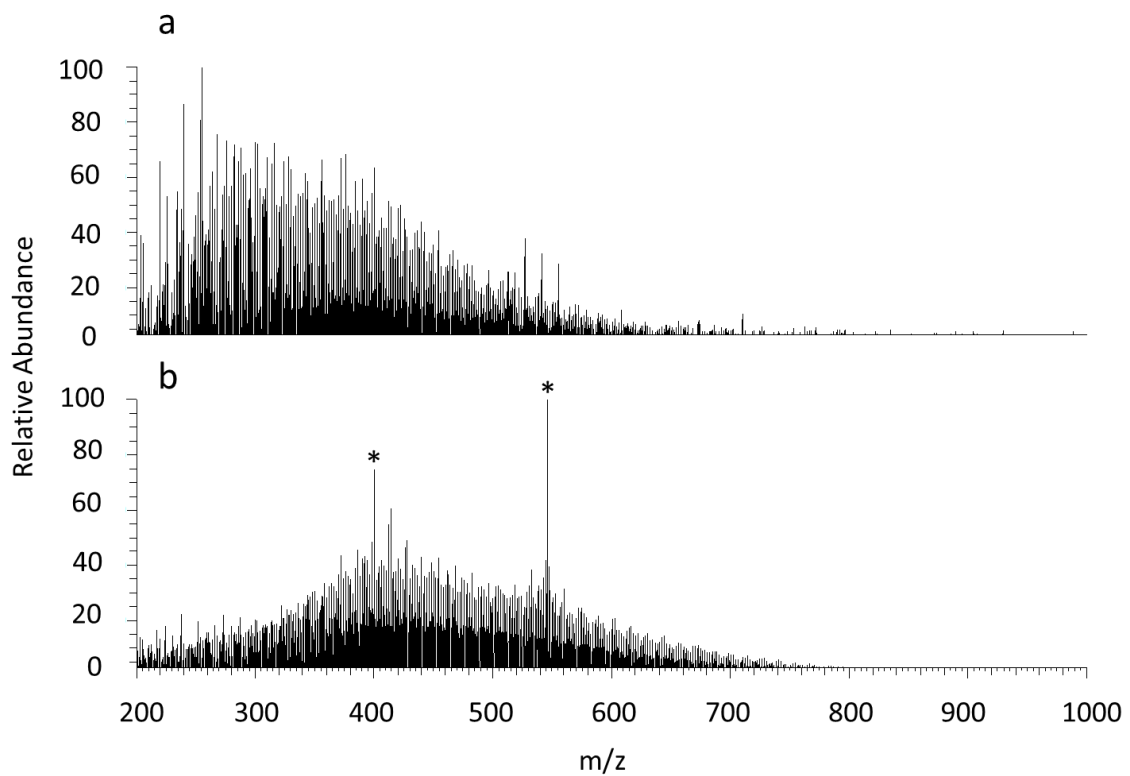


Figure 3.2 (+)APCI CS₂ mass spectra showing molecular ions of compounds in asphaltenes (a) Rose and (b) Montana. * Indicate instrument or chemical noise.

3.3.2 MCAD Patterns of Molecular Ions Derived from Single-core and Multicore Model Compounds

As mentioned previously, earlier studies have employed CAD and MCAD methods to study the fragmentation patterns of a wide range of asphaltene model compounds.^{23,29,32} These studies suggest that ions derived from single- and multicore compounds fragment to yield ions of similar or decreased RDBE values, respectively. To demonstrate this, the MCAD fragmentation patterns of ions derived from two model compounds are discussed here. MCAD of single-core (1,6-dipentylpyrene) ions resulted in the loss of either one or both alkyl chains to generate fragment ions with a similar RDBE but decreased m/z -values compared to the molecular ions (Figures 3.3a and 3.3b). In contrast, MCAD of multicore (1,4-di(pyren-1-yl)butane) ions resulted in the loss of an aromatic core and an alkyl chain, generating fragment ions with both a lower RDBE and lower m/z -value than the molecular ions (Figures 3.3c and 3.3d). Overall, these data suggest that the molecular ions of single- and multicore compounds can be differentiated based on the RDBE values of their fragment ions generated upon MCAD.

It must be mentioned that conventional resonance-type ITCAD is not suitable for this analysis. During beam-type MCAD, fragment ions are accelerated and collided with nitrogen molecules, resulting in further fragmentation. By comparison, ITCAD only activates precursor ions.²³ Therefore, multiple ion isolation/CAD processes are required to cleave all of the alkyl chains attached to the aromatic cores of ionized asphaltene model compounds, a step necessary for accurately determining the abundance of single- and multicore compounds in asphaltenes.^{24,30} Consequently, an ITCAD-based investigation of asphaltenes sample would require hundreds or thousands of isolation/fragmentation steps and thus is extremely complicated if not impossible. Therefore, this study uses MCAD to fragment the ionized asphaltenes rather than ITCAD.

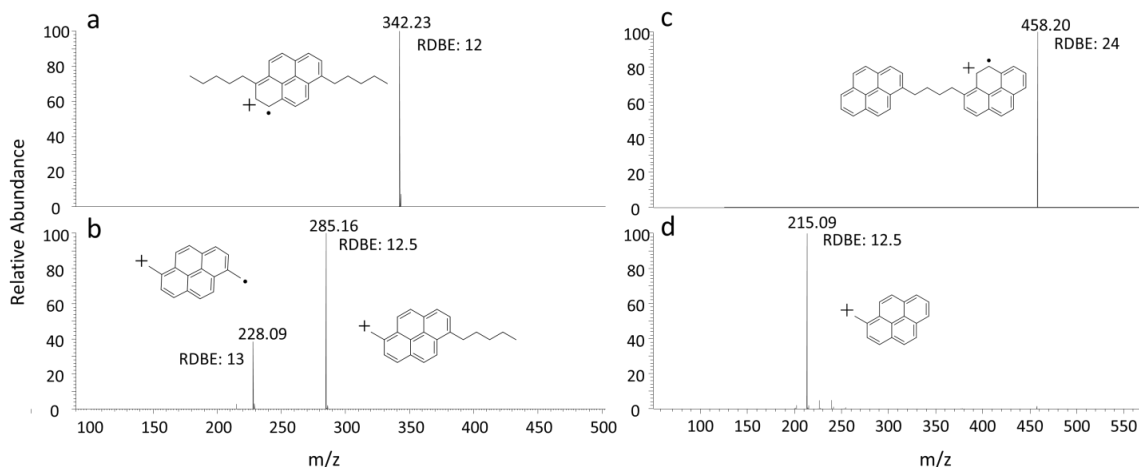
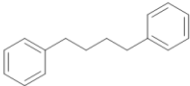
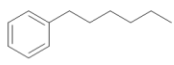
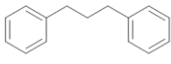
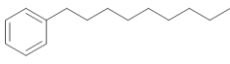
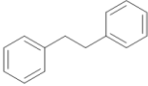
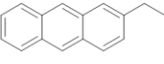


Figure 3.3 (a) A mass spectrum of the isolated molecular ions of 1,6-dipentylpyrene. (b) A MCAD mass spectrum measured for the molecular ions of 1,6-dipentylpyrene at a collision energy of 41 eV. (c) A mass spectrum of the isolated molecular ions of 1,4-di(pyren-1-yl)butane. (d) A MCAD mass spectrum measured for the molecular ions of 1,4-di(pyren-1-yl)butane at a collision energy of 41 eV.

3.3.3 MCAD Patterns Measured for Molecular Ions Derived from Mixtures of Single-core and Multicore Model Compounds

The model compound study implied that it may be possible to qualitatively determine the relative abundances of single- and multicore compounds in asphaltenes based on the difference between the RD BE of an asphaltene molecular ion and its fragment ion following MCAD. To demonstrate this, first I needed to show that the decrease in RD BE value upon MCAD fragmentation can be used to determine the multicore compound abundances in simple mixtures. Six model compounds included in this study, including three single-core and three multicore compounds, are shown in Table 3.2. Five mixtures, each with a different molar percent of multicore compounds were made: 0 %, 17 %, 50 %, 83 %, and 100 % multicore mixtures; the exact concentrations of these mixtures are shown in Table 3.1.

Table 3.2 Single-core and multicore model compounds studied.

Multicore		Single-core	
	1,4-Diphenylbutane $C_{16}H_{18}$ 210.32 Da		n-Hexylbenzene $C_{12}H_{18}$ 162.28 Da
	1,3-Diphenylpropane $C_{15}H_{16}$ 196.29 Da		n-Nonylbenzene $C_{15}H_{24}$ 204.36 Da
	1,2-Diphenylethane $C_{14}H_{14}$ 182.27 Da		2-Ethylantracene $C_{16}H_{14}$ 206.29 Da

The (+)APCI/CS₂ high-resolution mass spectrum measured for the 50 % multicore mixture is shown in Figure 3.4. The ionized single-core compounds showed approximately twice the abundance compared to the ionized multicore compounds, suggesting that single-core compounds ionize approximately two times more efficiently than multicore compounds when this ionization method is used. Therefore, the quantitation of multicore compounds is affected by a considerable ionization bias that favors single-core compounds.

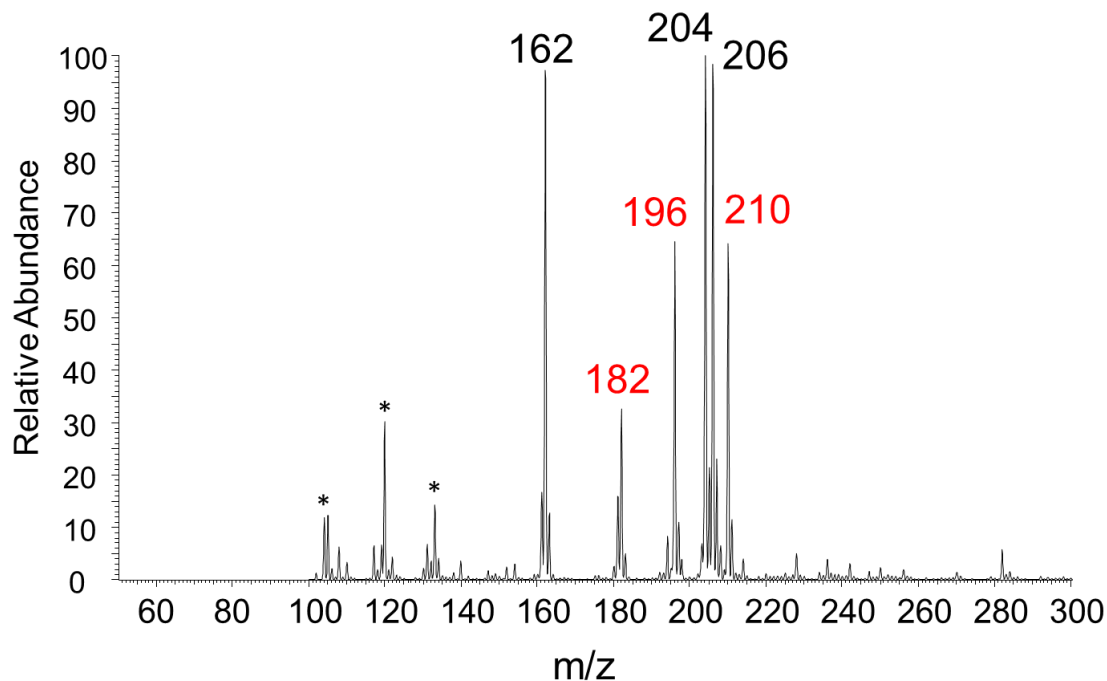


Figure 3.4 (+)APCI CS₂ mass spectrum showing molecular ions derived from the model compound mixture containing equimolar concentrations of six multicore and single-core compounds shown in Table 3.1 and Table S3.2. The red numbers indicate multicore ions and the black numbers indicate single-core ions. * Instrument or chemical noise.

Figure 3.5 shows RDBE plots for the molecular ions derived from each multicore mixture and those for their fragment ions after MCAD at a collision energy of 12 eV. MCAD mass spectra measured for ionized mixtures containing more multicore compounds should have a greater decrease in RDBE value following fragmentation because multicore molecular ions generate fragment ions with decreased RDBE values. Overall, the decrease in RDBE values correlated well with the abundance of multicore compounds in the mixtures (Figure 3.5). For a simple demonstration, the weighted average RDBE values for all detected ions were calculated from the data shown in Figure 3.5. The weighted average RDBE values were calculated based on equation 1:

$$\text{Weighted average RDBE value} = \frac{\sum RDBE \times Abundance}{\sum Abundance} \quad (1)$$

Where RDBE is the RDBE value of the ion.

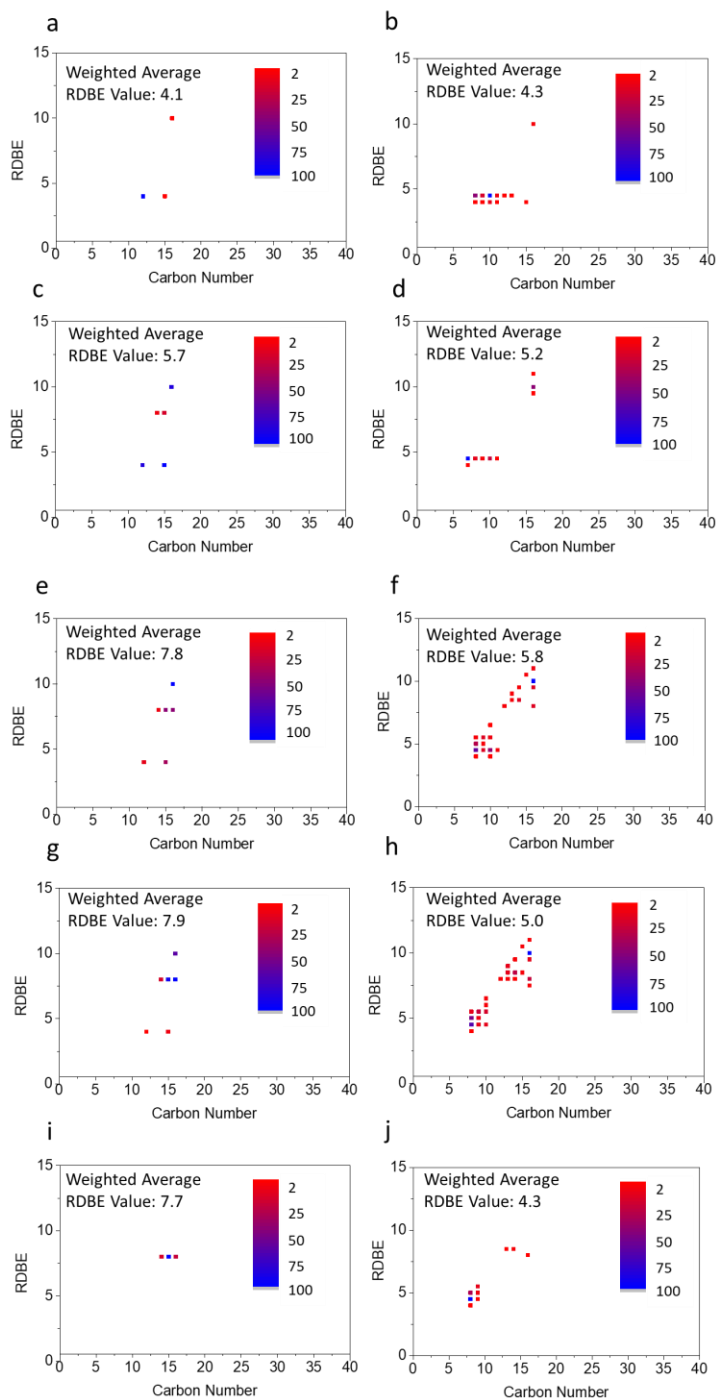


Figure 3.5 Plots of RDBE values as a function of the number of carbons in the molecular ions of model compounds and their fragment ions after MCAD at a collision energy of 12 eV. (a, b) the 0 % multicore mixture, (c, d) the 17 % multicore mixture, (e, f) the 50 % multicore mixture, (g, h) the 83% multicore mixture, and (i, j) the 100 % multicore mixture. Ions are represented by dots in the plot, with the ions' relative abundances indicated by the color of the dots. The weighted average RDBE values were calculated according to equation 1.

Following MCAD, the ions derived from the 0 %, 17 %, 50 %, 83 %, and 100 % multicore mixtures showed the following changes in their weighted average RDBE values: +0.2, -0.5, -2.0, -2.9, and -3.3, respectively (Figure 3.5). This finding suggests that the decrease in the weighted average RDBE value following MCAD is positively correlated with the relative abundances of the multicore compounds in a mixture.

Furthermore, when the weighted average RDBE values of the mixtures were plotted as a function of collision energy (Figure 3.6a), the RDBE values increased at the highest collision energies was due to the loss of hydrogen atoms. This implies that the optimal collision energy for semi-quantitative evaluation is the energy which produces the greatest decrease in the weighted average RDBE value and not the greatest collision energy. Therefore, the percent decrease in RDBE at the optimal energy (referred to as %RDBE_{min} from now on) was used here for quantitation of multicore compound abundance. Figure 3.6b plots the %RDBE_{min} versus the concentration of the multicore compounds in the mixture. Overall, the %RDBE_{min} values correlate well with concentration ($R^2=0.9944$).

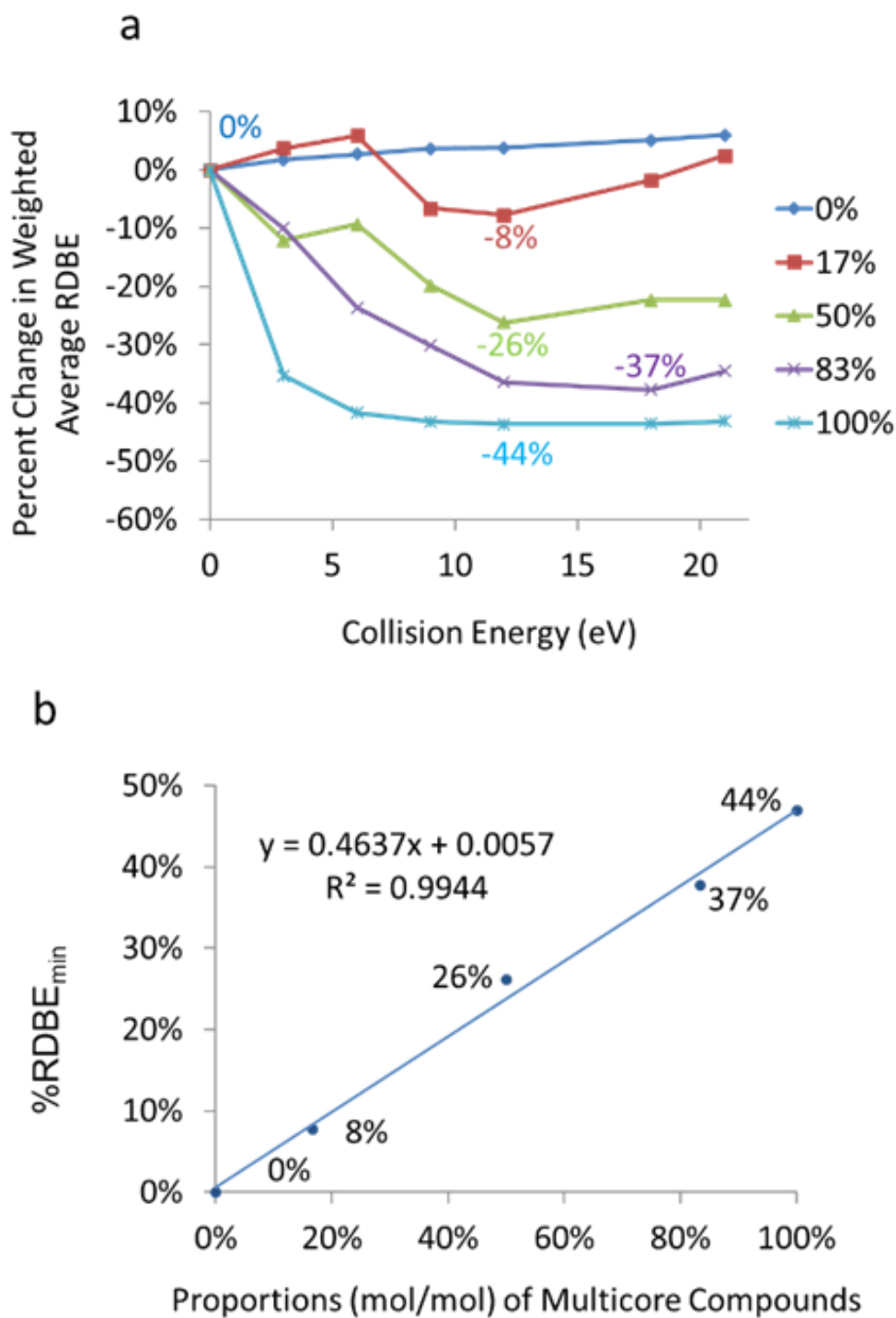


Figure 3.6 (a) Percent changes in the weighted average RDBE values as a function of collision energy for MCAD for the five ionized model compound mixtures containing different multicore molar percentages (0 %, 17 %, 50 %, 83 %, and 100 %, indicated by lines of different colors; the %RDBE_{min} values are indicated) and (b) %RDBE_{min} values as a function of the molar ratio of multicore compound in the mixture.

3.3.4 MCAD Patterns of Molecular Ions Derived from Asphaltenes

After demonstrating that the abundances of the multicore compounds in a mixture can be semi-quantitatively determined based on the %RDBE_{min} after MCAD, I employed this approach to determine the multicore compound abundances in molecular ions of m/z 350 ± 10 , 450 ± 10 , 550 ± 10 , and 650 ± 10 derived from two asphaltene samples to examine the unvalidated assumption in earlier studies discussed above. If the multicore compound abundances are different in these ions, these studies are likely susceptible to statistical sampling bias. The MCAD mass spectra used to determine the %RDBE_{min} are shown in Figures 3.7 to 3.14, and the weighted average RDBE values of all detected ions as a function of collision energy are shown in Figure 3.15. The percent change in the weighted average RDBE values as a function of collision energy and the %RDBE_{min} values are shown in Figure 3.16.

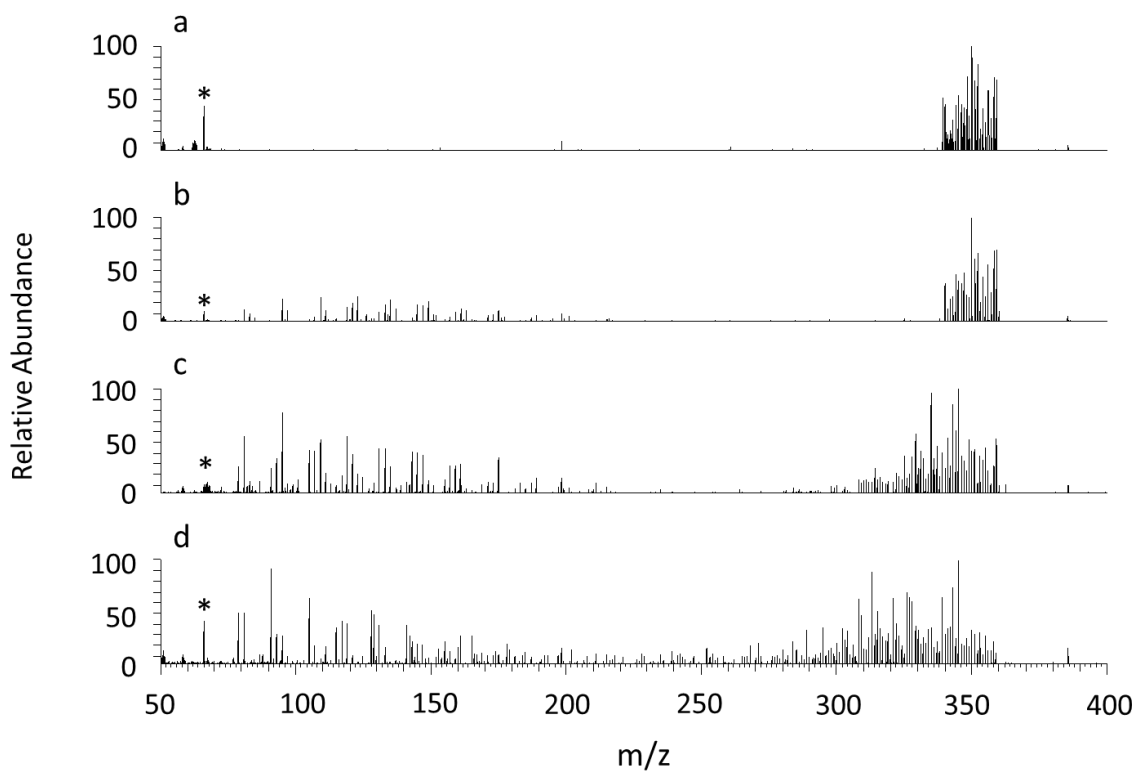


Figure 3.7 (a) (+)APCI CS_2 mass spectrum showing molecular ions of $m/z 350 \pm 10$ derived from Montana asphaltenes and MCAD mass spectra of the molecular ions of $m/z 350 \pm 10$ measured at collision energies of (b) 20 eV, (c) 40 eV and (d) 60 eV. * Instrument or chemical noise.

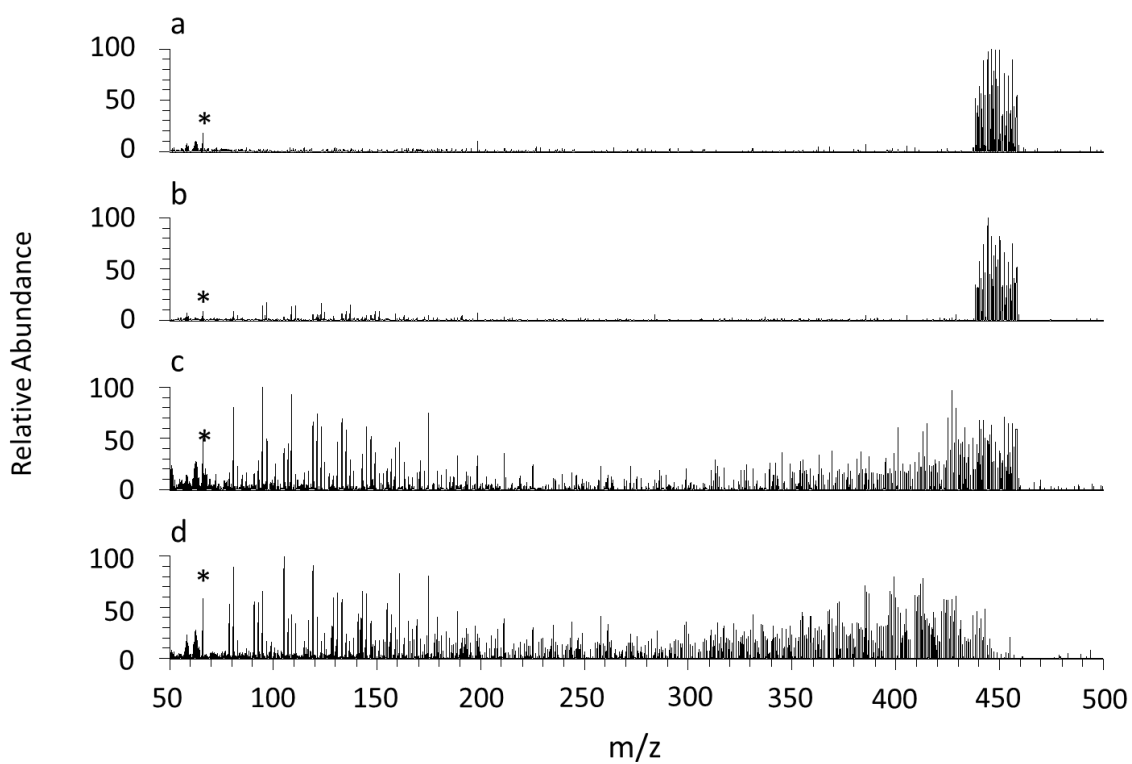


Figure 3.8 (a) (+)APCI CS₂ mass spectrum showing molecular ions of m/z 450 ± 10 derived from Montana asphaltenes and MCAD mass spectra of the molecular ions of m/z 450 ± 10 measured at collision energies of (b) 20 eV, (c) 40 eV and (d) 60 eV. * Instrument or chemical noise.

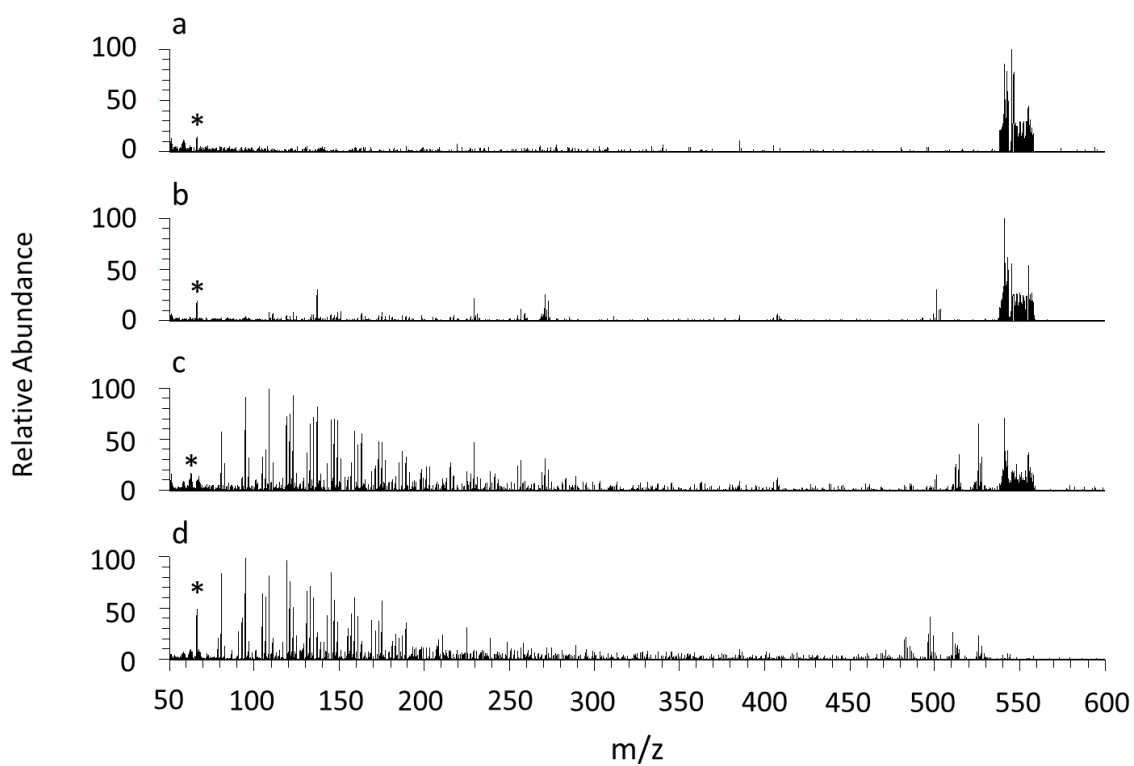


Figure 3.9 (a) (+)APCI CS₂ mass spectrum showing molecular ions of m/z 550 ± 10 derived from Montana asphaltenes and MCAD mass spectra of the molecular ions of m/z 550 ± 10 measured at collision energies of (a) 20 eV, (c) 40 eV and (d) 60 eV. *Instrument or chemical noise.

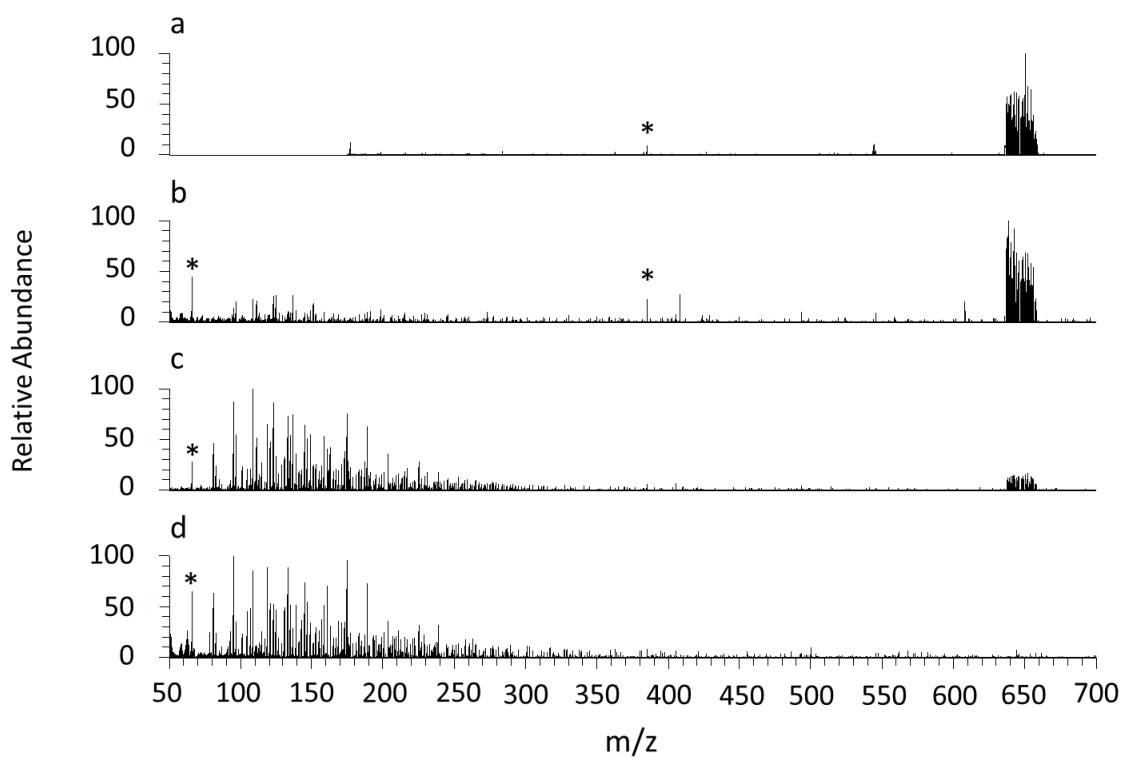


Figure 3.10 (a) (+)APCI CS₂ mass spectrum showing molecular ions of m/z 650 ± 10 derived from Montana asphaltenes and MCAD mass spectra of the molecular ions of m/z 650 ± 10 measured at collision energies of (b) 20 eV, (c) 40 eV and (d) 60 eV. *Instrument or chemical noise.

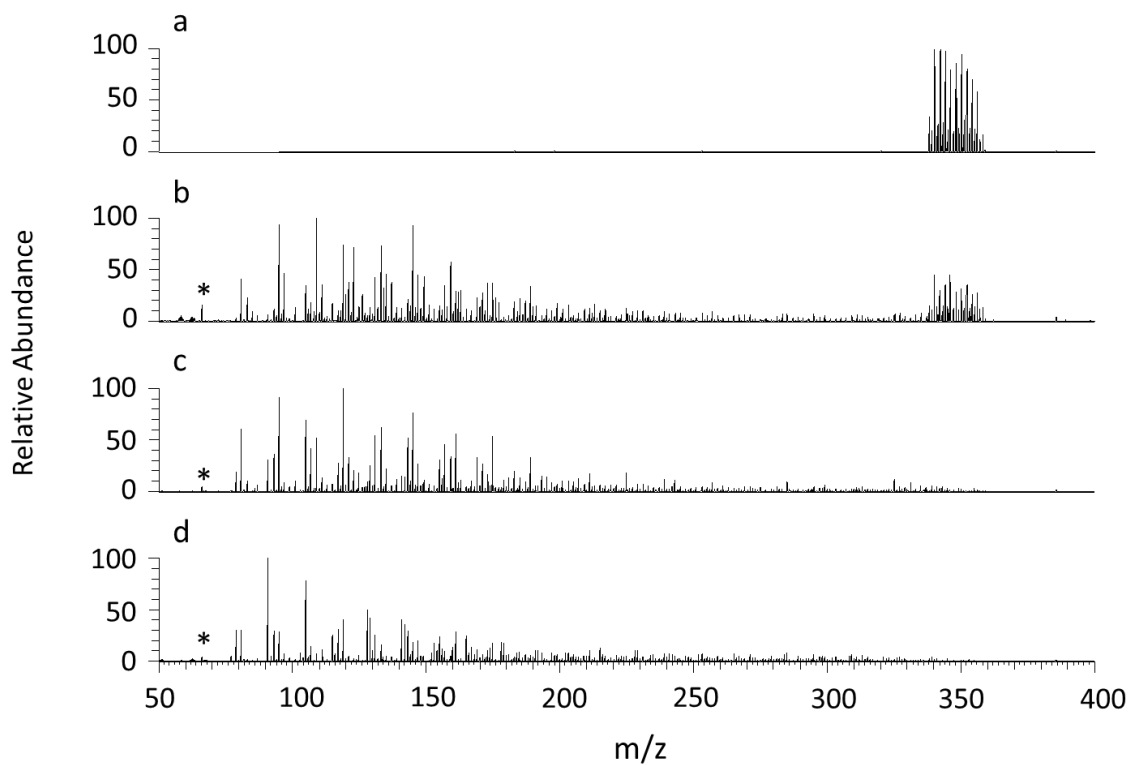


Figure 3.11 (a) (+)APCI CS₂ mass spectrum showing molecular ions of m/z 350 ± 10 derived from Rose asphaltenes and MCAD mass spectra of the molecular ions of m/z 350 ± 10 measured at collision energies of (b) 20 eV, (c) 40 eV and (d) 60 eV. *Instrument or chemical noise.

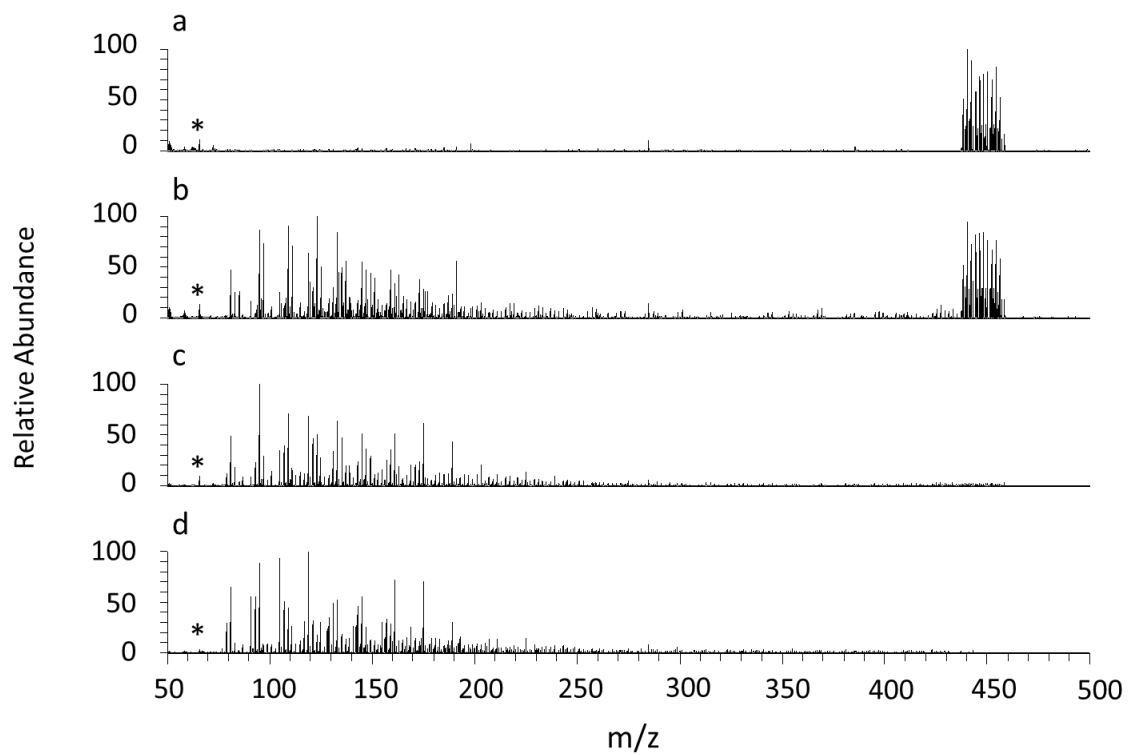


Figure 3.12 (a) (+)APCI CS₂ mass spectrum showing molecular ions of m/z 450 ± 10 derived from Rose asphaltenes and MCAD mass spectra of the molecular ions of m/z 450 ± 10 measured at collision energies of (b) 20 eV, (c) 40 eV and (d) 60 eV. *Instrument or chemical noise.

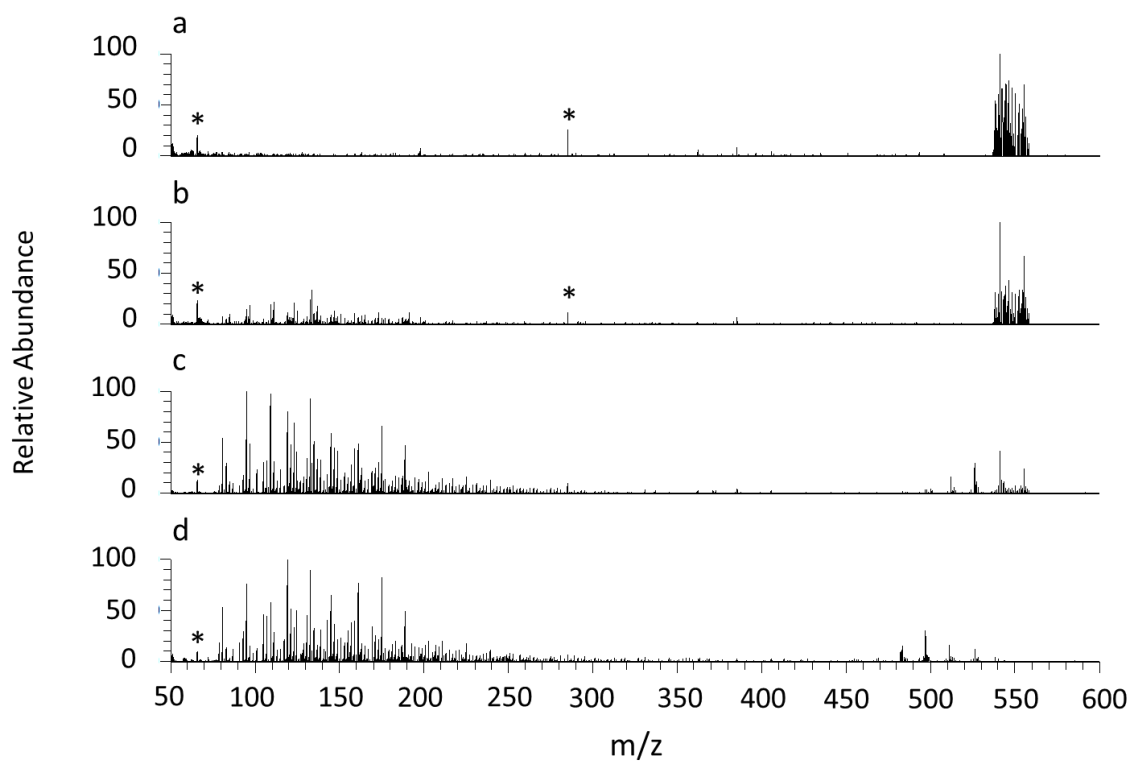


Figure 3.13 (a) (+)APCI CS₂ mass spectrum showing molecular ions of m/z 550 ± 10 derived from Rose asphaltenes and MCAD mass spectra of the molecular ions of m/z 550 ± 10 measured at collision energies of (b) 20 eV, (c) 40 eV and (d) 60 eV. *Instrument or chemical noise.

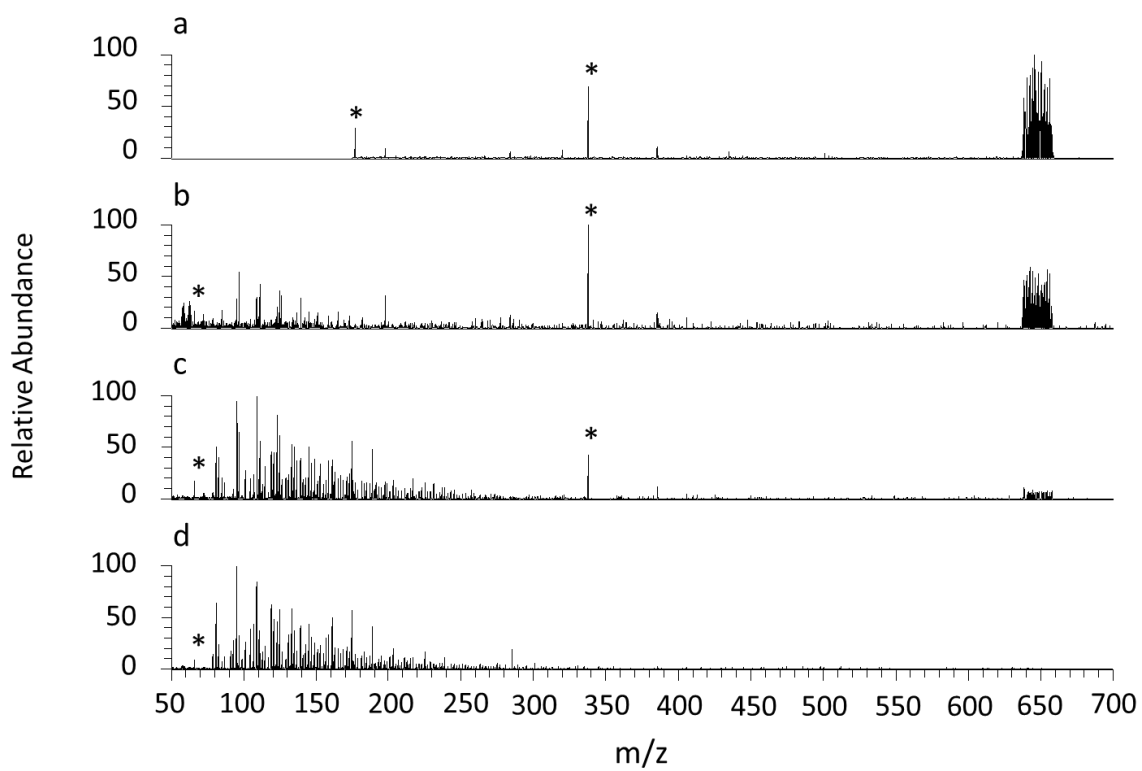


Figure 3.14 (a) (+)APCI CS₂ mass spectrum of molecular ions of m/z 650 ± 10 derived from Rose asphaltenes and MCAD mass spectra of the molecular ions of m/z 650 ± 10 measured at collision energies of (b) 20 eV, (c) 40 eV and (d) 60 eV. *Instrument or chemical noise.

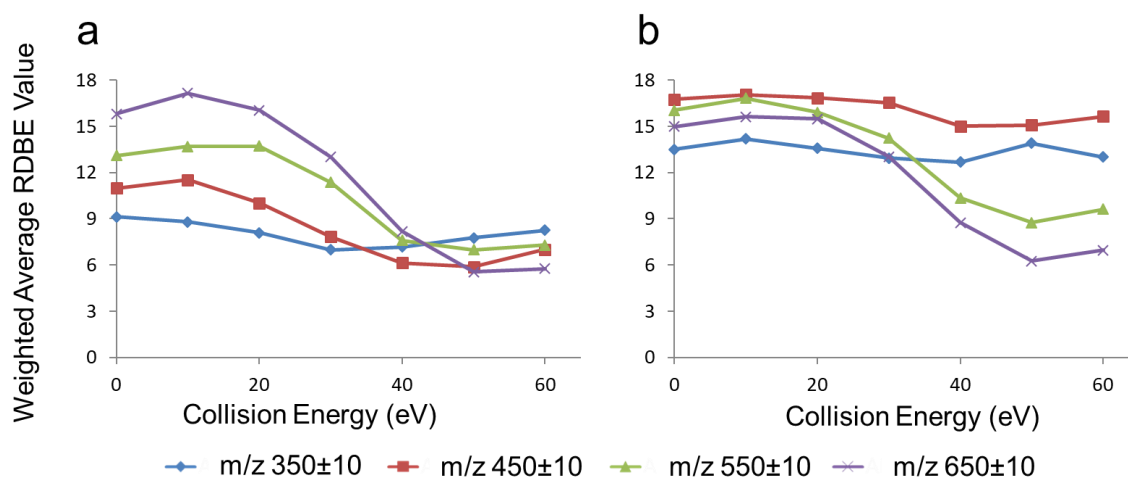


Figure 3.15 The weighted average RDBE values as a function of collision energy upon MCAD for five groups of ions (molecular ions of m/z 350±10, 450±10, 550±10, 650±10, and all of these ions combined, indicated by lines of different colors) derived from (a) Rose asphaltenes and (b) Montana asphaltenes.

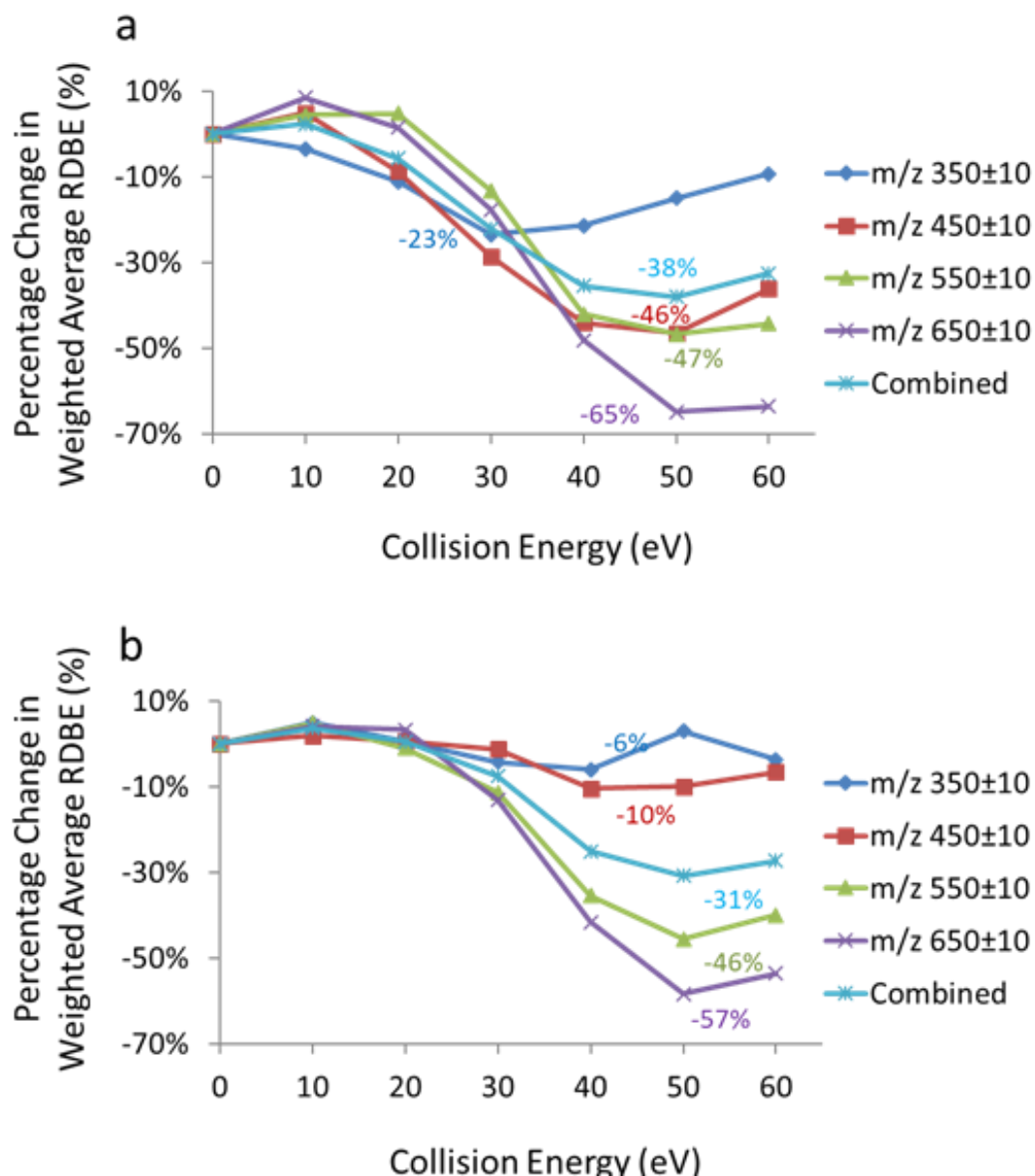


Figure 3.16 Percent change in the weighted average RDBE values as a function of collision energy after MCAD for five groups of ions (molecular ions of m/z 350±10, 450±10, 550±10, 650±10, and total, indicated by different colors) derived from (a) Rose asphaltenes and (b) Montana asphaltenes. The %RDBE_{min} values are indicated below the curve.

MCAD of ions of m/z 350 ± 10 , 450 ± 10 , 550 ± 10 and 650 ± 10 derived from Rose asphaltenes at different collision energies resulted in $\%RDBE_{\min}$ values of 23 %, 47 %, 47 %, and 65 %, respectively (Figure 3.16a), and the same values for the Montana sample were 6 %, 10 %, 46 %, and 57 %, respectively (Figure 3.16b). These observations suggest not only that the abundance of multicore compounds is greater for higher molecular weight compounds in both asphaltene samples, which implies that the abundances of single- and multicore compounds are not constant throughout the entire MW range. These findings also suggest the relative abundances of single- and multicore compounds in asphaltenes cannot accurately be determined with narrow ranges of m/z -values. This is well demonstrated by Montana and Rose asphaltenes: molecular ions of m/z 450 ± 10 derived from Rose and Montana asphaltenes showed $\%RDBE_{\min}$ values of $\sim 47\%$ (Figure 3.16a, red line) and $\sim 10\%$ (Figure 3.16b, red line), respectively, suggesting that Rose asphaltenes contain more multicore compounds than Montana asphaltenes. However, ions of m/z 550 ± 10 derived from Rose and Montana asphaltenes showed $\%RDBE_{\min}$ values of $\sim 46\%$ (Figure 3.16a, green line) and $\sim 47\%$ (Figure 3.16b, green line), respectively, which would lead to the conclusion that the multicore compound abundances are nearly identical. These observations clearly demonstrate that sampling bias can lead to contradictory and biased conclusions. Therefore, statistical considerations must be included when designing sampling methods.

As discussed above, ions of m/z 350 ± 10 , 450 ± 10 , 550 ± 10 and 650 ± 10 provide a reasonable representation of the asphaltene samples. Therefore, to avoid the sampling bias, I determined the $\%RDBE_{\min}$ value for the sum of these ions. The $\%RDBE_{\min}$ values for these samples are 38 % and 31 %, respectively (Figure 3.16, cyan lines labeled “combined”). Consequently, I conclude that the Rose asphaltene sample contains slightly more multicore compounds than the Montana asphaltene sample. Based on the calibration plot (Figure 3.6b), Rose and Montana asphaltenes contain $\sim 81\%$ and $\sim 65\%$ multicore compounds, respectively.

It should be noted that the calibration plot was generated for simple model compound mixtures containing only compounds with one or two aromatic cores. However, asphaltenes mixtures could contain compounds with more than two aromatic cores. Ions of m/z 650 ± 10 derived from Rose and Montana asphaltenes showed $\%RDBE_{\min}$ values of 65 %

and 57 %, respectively (Figure 3.6). As discussed in the above model compound mixture studies (Figure 3.6), the mixture containing 100 % multicore compounds with two aromatic cores showed a %RDBE_{min} value of 44 %. This suggests that %RDBE_{min} values larger than 44 % imply that a significant portion of multicore compounds in genuine asphaltenes contain more than two aromatic cores. On one hand, this significantly limits my approach, to comparisons between abundances of multicore compounds between different asphaltene samples. On the other hand, this observation is arguably the first MS evidence for the presence of multicore compounds with more than two aromatic cores in asphaltenes.

3.3.5 ISCAD Patterns Measured for Molecular Ions Derived from Mixtures of Single-core and Multicore Model Compounds

As discussed above, proper statistical considerations should be included when designing MS/MS experiments. However, it is impossible to completely remove statistical sampling biases without looking at the entire sample. In this section, I explored ISCAD as an alternative to MCAD. In ISCAD, all ions formed in the ion source are accelerated by the same DC voltage to collide with molecules, which results in fragmentation. Because the ions are not isolated and are accelerated by the same voltage, ISCAD is not susceptible to the sampling biases of traditional CAD and is a relatively common feature in commercial mass spectrometers.³⁹

In this section, the ISCAD-MS approach is evaluated using the five model compound mixtures discussed previously. All the mixtures were ionized and subjected to ISCAD at different collision energies. Figure 3.17a shows the percent changes in the weighted average RDBE values upon ISCAD as a function of collision energy. Upon ISCAD, the 0, 17, 50, 83, and 100% multicore mixtures exhibited %RDBE_{min} values of 0, 2, 21, 37, and 39%, respectively (Figure 3.17a). These values are slightly different from those obtained using MCAD for the same mixtures (%RDBE_{min} values were 0, 8, 26, 37, and 43 %, respectively). Nevertheless, the similar %RDBE_{min} values observed at the same collision energies indicates that ISCAD can also be used for similar comparisons as MCAD. Figure 3.17b shows the %RDBE_{min} values as a function of multicore compound concentration. Overall, the %RDBE_{min} values during ISCAD showed good linear relationship with the multicore compound concentration in the mixture ($R^2=0.9764$). However, I must point out that although ISCAD does not suffer from sampling bias, the

absence of ion isolation makes it more sensitive to matrix effects. As a result, the calibration plot obtained from MCAD has a slightly better R^2 value (Figure 3.6b; $R^2 = 0.9944$) than that obtained from ISCAD (Figure 3.17b; $R^2 = 0.9764$).

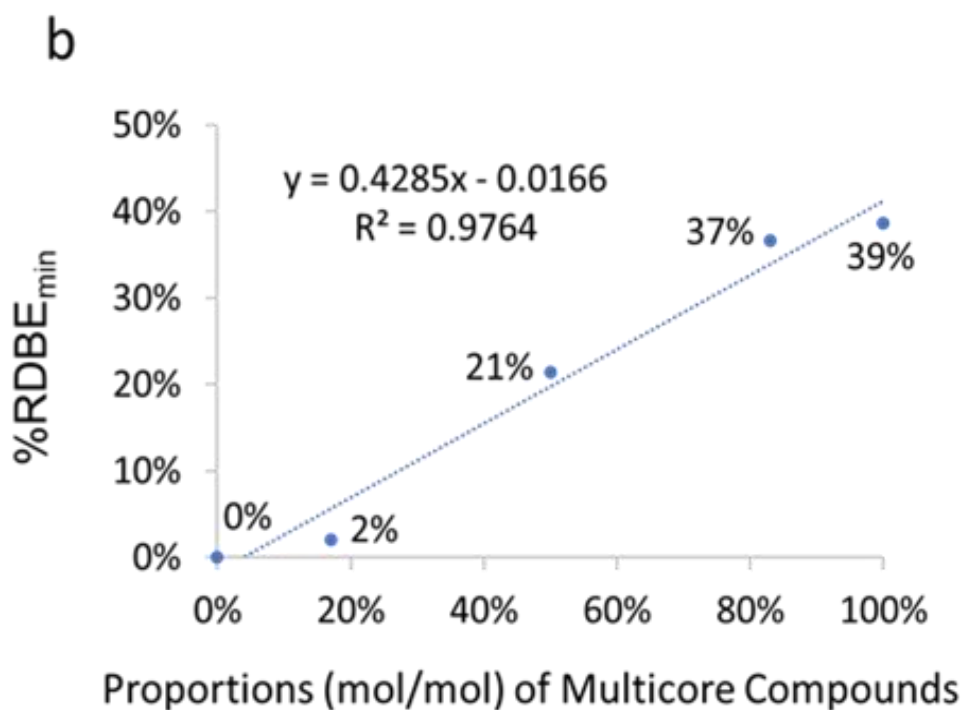
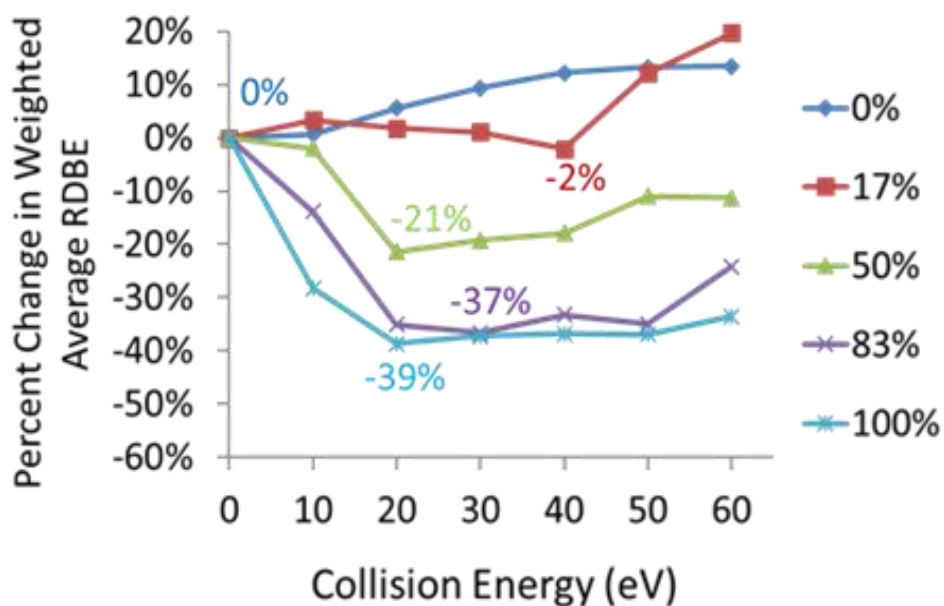


Figure 3.17 (a) Percent changes in the weighted average RDBE values upon ISCAD as a function of collision energy for the five ionized model compound mixtures with different multicore molar percentages (0 %, 17 %, 50 %, 83 %, and 100 %, indicated by lines of different colors) and (b) %RDBE_{min} values as proportions (mol/mol) of multicore compounds in the mixture.

3.3.6 ISCAD Patterns of Molecular Ions Derived from Asphaltenes

As with the earlier MCAD approach, I employed ISCAD to examine the relative abundances of single-core and multicore compounds in the Rose and Montana asphaltene samples. Figure 3.18 shows the percent changes in the weighted average RDBE values versus the ISCAD collision energies. Rose and Montana asphaltenes showed %RDBE_{min} values of 23 % and 15 %, respectively (Figure 3.18). Overall, the results imply that Rose asphaltenes contain more multicore compounds than Montana asphaltenes because Rose asphaltenes showed 8 % larger %RDBE_{min}. Based on the semi-quantitative calibration plot in Figure 3.17b, Rose and Montana asphaltenes contain approximately 57% and 39% multicore compounds, respectively.

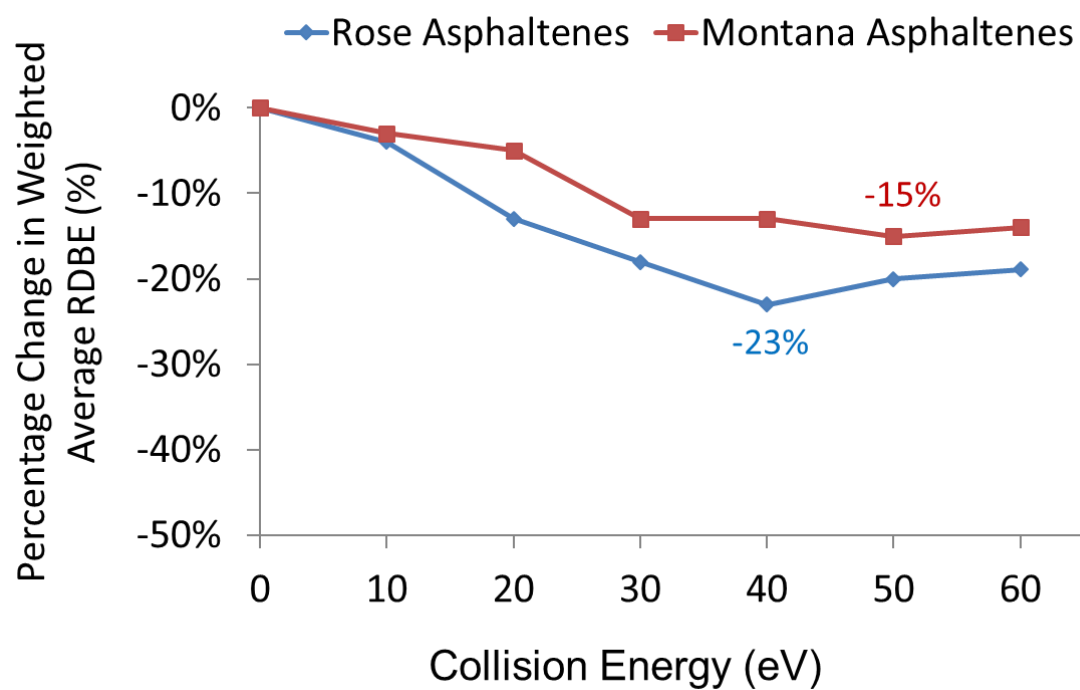


Figure 3.18 Percent changes in the weighted average RDBE values as a function of collision energy after ISCAD for ionized Rose and Montana asphaltene samples. %RDBE_{min} values are labeled.

3.4 Conclusions

In many earlier studies, ions of only one up to a few m/z values were isolated and used to compare the relative abundances of single-core and multicore compounds in asphaltenes. This approach essentially assumed that the relative abundances of single-core and multicore compounds are uniform across the entire asphaltene sample. The present study discussed statistical sampling issue and demonstrated that the assumption behind these studies is invalid for both asphaltene samples tested. This statistical sampling issue can be addressed by either including more samples (ions) or employing methods that are less susceptible to sampling biases.

In this study, a high-resolution MS/MS approach based on MCAD was tested for the semi-quantitative comparison of single- and multicore compounds in model compound mixtures. Additionally, this method was extended to two asphaltene samples. The %RDBE_{min} values showed a good linear relationship with multicore compound abundance in the model compound mixture. In addition, molecular ions of m/z 350 ± 10 , 450 ± 10 , 550 ± 10 , and 650 ± 10 derived from Montana and Rose asphaltenes were investigated. These molecular ions were chosen because they provided a reasonable statistical representation of the entire asphaltene sample. The relative abundances of single-core and multicore compounds in these two asphaltenes were compared based on the %RDBE_{min} values of these ions after MCAD. The relative abundances of multicore compounds and single-core compounds were found to vary across the MW range of asphaltenes. As a result, contradictory conclusions would be reached if only limited numbers of ions were considered. To address this issue, all of the molecular ions of m/z 350 ± 10 , 450 ± 10 , 550 ± 10 and 650 ± 10 derived from Montana and Rose asphaltenes were summed together and examined. The comparison revealed that Rose asphaltenes contain a higher multi- to single-core compound ratio than Montana asphaltenes.

ISCAD was proposed as an alternative approach for the comparison of the relative abundances of single-core and multicore compounds in asphaltenes. ISCAD involves fragmentation of all ions without isolation. Therefore, ISCAD is not susceptible to the same sampling biases as MCAD. The ISCAD study yielded an 8% larger %RDBE_{min} value for Rose asphaltenes. On the other hand, the %RDBE_{min} value of Rose asphaltenes was found to be 7% larger than for Montana asphaltenes when using MCAD and the increased,

statistically representative samples. The two methods reached similar conclusions on the relative abundances of multicore compounds in Rose and Montana asphaltenes. Such agreement indicates that the MCAD sampling method provides a reasonable statistical representation of the ionized asphaltene samples.

To properly optimize crude oil refining processes and minimize problems associated with asphaltenes, determination of the relative abundances of the single-core and multicore compounds is required. This study provides critical insights into how to obtain a statistically unbiased semi-quantitative evaluation of the relative abundances of single-core and multicore compounds in asphaltenes. However, it must be noted that the approach employed in this study only addresses statistical sampling issues in MS-based asphaltene analysis. The analysis presented here is still subject to the ionization bias for single-core compounds, which cannot be addressed by the approaches presented in this study.

3.5 References

- (1) Rana, M. S.; Samano, V.; Ancheyta, J.; Diaz, J. A Review of Recent Advances on Process Technologies for Upgrading of Heavy Oils and Residua. *Fuel*. **2007**, *86*, 1216-1231.
- (2) Mullins, O. C.; Sheu, E. Y.; Hammami, A.; Marshall, A. G. *Asphaltenes, Heavy Oils, and Petroleomics*; Springer Science & Business Media: New York, 2007.
- (3) Mamin, G.; Gafurov, M.; Yusupov, R.; Gracheva, I.; Ganeeva, Y. M.; Yusupova, T.; Orlinkii, S. Toward the Asphaltene Structure by Electron Paramagnetic Resonance Relaxation Studies at High Fields (3.4 T). *Energy Fuels*. **2016**, *30*, 6942-6946.
- (4) Strausz, O. P.; Mojelsky, T. W.; Lown, E. M. The Molecular Structure of Asphaltene: An Unfolding Story. *Fuel*. **1992**, *71*, 1355-1363.
- (5) Strausz, O. P.; Peng, P. a.; Murgich, J. About the Colloidal Nature of Asphaltenes and the Mw of Covalent Monomeric Units. *Energy Fuels*. **2002**, *16*, 809-822.
- (6) Alvarez-Ramírez, F.; Ruiz-Morales, Y. Island Versus Archipelago Architecture for Asphaltenes: Polycyclic Aromatic Hydrocarbon Dimer Theoretical Studies. *Energy Fuels*. **2013**, *27*, 1791-1808.
- (7) Wittrig, A. M.; Fredriksen, T. R.; Qian, K.; Clingenpeel, A. C.; Harper, M. R. Single Dalton Collision-Induced Dissociation for Petroleum Structure Characterization. *Energy Fuels*. **2017**.
- (8) Jaffe, S. B.; Freund, H.; Olmstead, W. N. Extension of Structure-Oriented Lumping to Vacuum Residua. *Ind. Eng. Chem. Res.* **2005**, *44*, 9840-9852.
- (9) Quann, R. J.; Jaffe, S. B. Structure-Oriented Lumping: Describing the Chemistry of Complex Hydrocarbon Mixtures. *Ind. Eng. Chem. Res.* **1992**, *31*, 2483-2497.
- (10) Karimi, A.; Qian, K.; Olmstead, W. N.; Freund, H.; Yung, C.; Gray, M. R. Quantitative Evidence for Bridged Structures in Asphaltenes by Thin Film Pyrolysis. *Energy Fuels*. **2011**, *25*, 3581-3589.
- (11) Mullins, O. C. The Modified Yen Model. *Energy Fuels*. **2010**, *24*, 2179-2207.
- (12) Mullins, O. C.; Sabbah, H.; Eyssautier, J.; Pomerantz, A. E.; Barré, L.; Andrews, A. B.; Ruiz-Morales, Y.; Mostowfi, F.; McFarlane, R.; Goual, L. Advances in Asphaltene Science and the Yen–Mullins Model. *Energy Fuels*. **2012**, *26*, 3986-4003.
- (13) Chacón-Patiño, M. L.; Rowland, S. M.; Rodgers, R. P. Advances in Asphaltene Petroleomics. Part 1: Asphaltenes Are Composed of Abundant Island and Archipelago Structural Motifs. *Energy Fuels*. **2017**, *31*, 13509-13518.

- (14) Chacón-Patiño, M. L.; Rowland, S. M.; Rodgers, R. P. Advances in Asphaltene Petroleomics 2. A Selective Separation Method That Reveals Fractions Enriched in Island and Archipelago Structural Motifs by Mass Spectrometry. *Energy Fuels*. **2017**, *32*, 314-328.
- (15) Sabbah, H.; Morrow, A. L.; Pomerantz, A. E.; Mullins, O. C.; Tan, X.; Gray, M. R.; Azyat, K.; Tykwinski, R. R.; Zare, R. N. Comparing Laser Desorption/Laser Ionization Mass Spectra of Asphaltenes and Model Compounds. *Energy Fuels*. **2010**, *24*, 3589-3594.
- (16) Groenzin, H.; Mullins, O. C. Molecular Size and Structure of Asphaltenes from Various Sources. *Energy Fuels*. **2000**, *14*, 677-684.
- (17) Schuler, B.; Meyer, G.; Peña, D.; Mullins, O. C.; Gross, L. Unraveling the Molecular Structures of Asphaltenes by Atomic Force Microscopy. *J. Am. Chem. Soc.* **2015**, *137*, 9870-9876.
- (18) Gray, M. R.; Tykwinski, R. R.; Stryker, J. M.; Tan, X. Supramolecular Assembly Model for Aggregation of Petroleum Asphaltenes. *Energy Fuels*. **2011**, *25*, 3125-3134.
- (19) Dickie, J. P.; Yen, T. F. Macrostructures of the Asphaltic Fractions by Various Instrumental Methods. *Anal. Chem.* **1967**, *39*, 1847-1852.
- (20) Groenzin, H.; Mullins, O. C. Asphaltene Molecular Size and Structure. *J. Phys. Chem. A*. **1999**, *103*, 11237-11245.
- (21) Sharma, A.; Groenzin, H.; Tomita, A.; Mullins, O. C. Probing Order in Asphaltenes and Aromatic Ring Systems by Hrtm. *Energy Fuels*. **2002**, *16*, 490-496.
- (22) Schuler, B.; Meyer, G.; Peña, D.; Mullins, O. C.; Gross, L. Unraveling the Molecular Structures of Asphaltenes by Atomic Force Microscopy. *J. Am. Chem. Soc.* **2015**, *137*, 9870-9876.
- (23) Jarrell, T. M.; Jin, C.; Riedeman, J. S.; Owen, B. C.; Tan, X.; Scherer, A.; Tykwinski, R. R.; Gray, M. R.; Slater, P.; Kenttämä, H. I. Elucidation of Structural Information Achievable for Asphaltenes Via Collision-Activated Dissociation of Their Molecular Ions in Msn Experiments: A Model Compound Study. *Fuel*. **2014**, *133*, 106-114.
- (24) DeCanio, S. J.; Nero, V. P.; DeTar, M. M.; Storm, D. A. Determination of the Molecular Weights of the Ratawi Vacuum Residue Fractions—a Comparison of Mass Spectrometric and Vapour Phase Osmometry Techniques. *Fuel*. **1990**, *69*, 1233-1236.

- (25) Karaca, F.; Morgan, T.; George, A.; Bull, I.; Herod, A.; Millan, M.; Kandiyoti, R. Molecular Mass Ranges of Coal Tar Pitch Fractions by Mass Spectrometry and Size-Exclusion Chromatography. *Rapid Commun. Mass Spectrom.* **2009**, *23*, 2087-2098.
- (26) Ha, J.; Cho, E.; Kim, S. Interpreting Chemical Structures of Compounds in Crude Oil Based on the Tandem Mass Spectra of Standard Compounds Obtained at the Same Normalized Collision Energy. *Energy Fuels.* **2017**, *31*, 6960-6967.
- (27) Nyadong, L.; Lai, J.; Thompsen, C.; LaFrancois, C. J.; Cai, X.-h.; Song, C.; Wang, J.; Wang, W. High-Field Orbitrap Mass Spectrometry and Tandem Mass Spectrometry for Molecular Characterization of Asphaltenes. *Energy Fuels.* **2017**, *32*, 294-305.
- (28) Ha, J.; Cho, E.; Kim, S. Interpreting Chemical Structures of Compounds in Crude Oil Based on the Tandem Mass Spectra of Standard Compounds Obtained at the Same Normalized Collision Energy. *Energy Fuels.* **2017**, *31*, 6960-6967.
- (29) Sabbah, H.; Morrow, A. L.; Pomerantz, A. E.; Zare, R. N. Evidence for Island Structures as the Dominant Architecture of Asphaltenes. *Energy Fuels.* **2011**, *25*, 1597-1604.
- (30) Wittrig, A. M.; Fredriksen, T. R.; Qian, K.; Clingenpeel, A. C.; Harper, M. R. Single Dalton Collision-Induced Dissociation for Petroleum Structure Characterization. *Energy Fuels.* **2017**, *31*, 13338-13344.
- (31) Podgorski, D. C.; Corilo, Y. E.; Nyadong, L.; Lobodin, V. V.; Bythell, B. J.; Robbins, W. K.; McKenna, A. M.; Marshall, A. G.; Rodgers, R. P. Heavy Petroleum Composition. 5. Compositional and Structural Continuum of Petroleum Revealed. *Energy Fuels.* **2013**, *27*, 1268-1276.
- (32) Nyadong, L.; Lai, J.; Thompsen, C.; LaFrancois, C. J.; Cai, X.; Song, C.; Wang, J.; Wang, W. High-Field Orbitrap Mass Spectrometry and Tandem Mass Spectrometry for Molecular Characterization of Asphaltenes. *Energy Fuels.* **2017**, *32*, 294-305.
- (33) Owen, B. C.; Gao, J.; Borton, D. J.; Amundson, L. M.; Archibold, E. F.; Tan, X.; Azyat, K.; Tykwinski, R.; Gray, M.; Kenttämaa, H. I. Carbon Disulfide Reagent Allows the Characterization of Nonpolar Analytes by Atmospheric Pressure Chemical Ionization Mass Spectrometry. *Rapid Commun. Mass Spectrom.* **2011**, *25*, 1924-1928.
- (34) Tan, X.; Fenniri, H.; Gray, M. R. Pyrene Derivatives of 2, 2'-Bipyridine as Models for Asphaltenes: Synthesis, Characterization, and Supramolecular Organization. *Energy Fuels.* **2007**, *22*, 715-720.

- (35) Lynch, K.; Hood, R.; Gomez, O.; Aquino, L. In *Proceedings of the 6th UNITAR/UNDP International Conference of Heavy Crude and Tar Sands*, 1995, pp 245-252.
- (36) Marshall, A. G.; Rodgers, R. P. Petroleomics: The Next Grand Challenge for Chemical Analysis. *Acc. Chem. Res.* **2004**, *37*, 53-59.
- (37) Wittrig, A. M.; Fredriksen, T. R.; Qian, K.; Clingenpeel, A. C.; Harper, M. R. Single Dalton Collision-Induced Dissociation for Petroleum Structure Characterization. *Energy Fuels.* **2017**, *31*, 13338-13344.
- (38) Kerry, S. M.; Bland, J. M. Statistics Notes: The Intracluster Correlation Coefficient in Cluster Randomisation. *BMJ.* **1998**, *316*, 1455.
- (39) Parcher, J. F.; Wang, M.; Chittiboyina, A. G.; Khan, I. A. In-Source Collision-Induced Dissociation (Is-Cid): Applications, Issues and Structure Elucidation with Single-Stage Mass Analyzers. *Drug Test Anal.* **2018**, *10*, 28-36.

CHAPTER 4. DETERMINATION OF AROMATIC CORE SIZES AND THE NUMBER OF CARBONS IN ALKYL CHAINS FOR ISOBARIC IONS DERIVED FROM ASPHALTENES BY USING HIGH-RESOLUTION TANDEM MASS SPECTROMETRY

4.1 Introduction

Asphaltenes are the heaviest fraction of crude oil and are defined as compounds that are insoluble in *n*-alkanes but soluble in toluene.^{1,2} Due to the rapid depletion of light crude oils, petroleum industries are increasingly dependent on heavy petroleum which is rich in asphaltenes.³ However, asphaltenes introduce significant and costly problems in the petroleum industry because they poison catalysts during upgrading and clog transportation pipelines.⁴ In order to develop solutions to these problems and to discover the means to utilize asphaltenes, an in-depth understanding of the structures of asphaltene molecules is of critical importance.⁵⁻⁹ Currently, asphaltene molecular structures are proposed to fall into two broad categories: single-core (island) and multicore (archipelago) structures.^{10,11} A single-core structure is composed of one aromatic core with attached alkyl chains⁶ while a multicore structure is composed of multiple aromatic cores connected by alkyl bridges.¹²

Investigating the molecular structures in asphaltenes is challenging due to their tremendous complexity.¹³ Various analytical methods have been used, but have only been able to determine the bulk properties of asphaltenes. Time-resolved fluorescence depolarization has revealed the molecular weight of the asphaltenes.¹⁴ Nuclear magnetic resonance has provided relative abundances of aliphatic and aromatic carbons in asphaltenes.¹⁵ Infrared spectroscopy has shed light on the relative abundances of different functional groups in asphaltenes.¹⁶ However, these methods cannot provide detailed structures for individual molecules. Atomic force microscopy and high resolution transmission electron microscopy have revealed the structures of a few hundred molecules derived from asphaltenes.^{17,18} However, several hundred molecules accounts for only a very small portion of the compounds in an asphaltene sample and cannot be used to describe the asphaltene sample as a whole. MS/MS can provide rapid characterization of a large number of compounds by isolating ionized compounds followed by CAD.^{4,19} MS/MS analysis of asphaltenes has significantly advanced the understanding of asphaltenes'

molecular structures²⁰⁻²⁴, such as potential aromatic building blocks²⁵, the possible relative abundances of single-core and multicore compounds¹⁹, the maximum numbers of carbons in alkyl chains, and the sizes of the smallest aromatic cores.²³

Unfortunately, asphaltenes contain many isobars and isomers. As a result, during MS/MS, isolated ions of a given nominal m/z value are inevitably composed of a group of isobaric and isomeric ions. This presents a huge challenge in the interpretation of MS/MS spectra because the fragment ions cannot be associated with one fragmenting ion.²³⁻²⁶ When performing MS/MS on asphaltene ions, CAD can be used to remove all alkyl chains, leaving a fragment ion corresponding to the smallest aromatic core present in the initial ion. The difference in m/z between the starting ion and the final fragment ion represents the combined mass of all the alkyl chains and can be used to calculate the maximum number of carbons present in the alkyl chains.^{23,24} This approach (referred to from here on as the conventional approach) has been employed to reveal the difference in sizes of aromatic cores size and alkyl chains in petroleum and coal asphaltenes by using low-resolution MS.^{23,24}

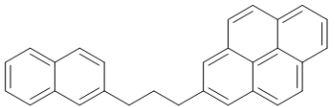
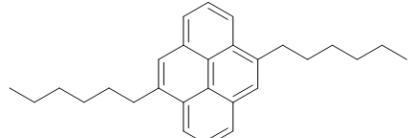
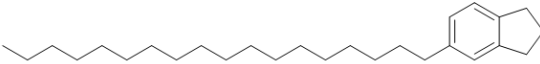
In this study, the conventional approach is further developed for the analysis of high-resolution MS/MS spectra. An asphaltene sample was ionized using APCI with CS_2 as an ionization reagent to generate stable molecular ions and analyzed using a linear-quadrupole ion trap/orbitrap mass spectrometer.²⁷ The ionized samples were fragmented via MCAD.²⁸ Instead of analyzing the MS/MS spectra directly, the ions obtained after MCAD are clustered into multiple groups based on their similar RDBE values. Then a MS/MS spectrum is reconstructed for each group of ions of similar RDBE (referred to as reconstructed spectrum) and each reconstructed spectrum is analyzed individually. This approach (referred to here as the new approach) reveals the smallest aromatic core sizes and the carbon numbers in alkyl chains in each reconstructed spectrum and thus reveals more details on aromatic core sizes and carbon numbers in alkyl chains.

4.2 Materials and Methods

CS₂ (>99% purity) was purchased from Sigma-Aldrich. Claire asphaltene sample (from United Kingdom) was obtained from ConocoPhillips. Model compounds 2-(3-(Naphthalen-2-yl)propyl)pyrene, 4,9-dihexylpyrene, 2,4,7,9-tetrakis(decyl)pyrene, 1,4-di(pyren-1-yl)butane, and 5-octadecyl-2,3-dihydro-1H-indene were synthesized in-house according to published methods.^{29,30}

10 mg of asphaltene sample was dissolved in 1 mL of CS₂. 10 mg of single-core model compound 2,4,7,9-tetrakis(decyl)pyrene was dissolved in 1 mL of CS₂. 10 mg of multicore model compound 1,4-di(pyren-1-yl)butane was dissolved in 1 mL of CS₂. 3 mg of each isobaric model compound 2-(3-(Naphthalen-2-yl)propyl)pyrene (370.17 Da), 4,9-dihexylpyrene (370.27 Da), and 5-octadecyl-2,3-dihydro-1H-indene (370.36 Da) were added into 1 mL of CS₂. The structures of the isobaric model compounds are shown in Table 4.1. 10 mg of the dissolved samples were introduced into a linear-quadrupole ion trap/orbitrap hybrid mass spectrometer through direct infusion at 5 μ L/min rate. The samples were ionized using positive mode APCI with CS₂ as ionization reagent to generate stable molecular ions.²⁴ Nitrogen gas was used as the auxiliary and sheath gas (flow rate set to 5 and 10 arbitrary units, respectively). Vaporizer and capillary temperatures were set to 300 °C and 275 °C, respectively. Molecular ions of m/z 400 \pm 0.5, 500 \pm 0.5, 600 \pm 0.5, and 700 \pm 0.5 were isolated in the linear quadrupole ion trap for MCAD fragmentation in the octopole collision cell located behind the C-trap. The ions fragment via their collisions with nitrogen gas in the octupole collision cell. Because the larger ions fragment slower than the smaller ions during CAD, the larger ions require more collision energy than the smaller ion to achieve similar extent of fragmentation. Hence, the molecular ions of 400 \pm 0.5, 500 \pm 0.5, 600 \pm 0.5, and 700 \pm 0.5 were fragmented at MCAD collision energies of 32 eV, 40 eV, 48 eV and 56 eV, respectively. The ions were detected using the high-resolution orbitrap mass analyzer at a resolution of 100,000. The RDBE plots and reconstructed MS/MS spectra were generated using Origin software.

Table 4.1 List of isobaric model compounds

	<p>2-(3-(naphthalen-2-yl)propyl)pyrene Chemical Formula: $C_{29}H_{22}$ Exact Mass: 370.17</p>
	<p>4,9-dihexylpyrene Chemical Formula: $C_{28}H_{34}$ Exact Mass: 370.27</p>
	<p>5-octadecyl-2,3-dihydro-1<i>H</i>-indene Chemical Formula: $C_{27}H_{46}$ Exact Mass: 370.36</p>

4.3 Results and Discussion

4.3.1 Conventional Methods for Analysis of an MS/MS Spectra

In an earlier study, a data analysis method was employed to study the maximum number of carbons in alkyl chains and the sizes of the smallest aromatic cores of isobaric ions based on low-resolution MS/MS spectra.^{23,24} The conventional method is employed here for analysis of an MCAD mass spectrum as a brief demonstration. The mass spectrum of molecular ions of m/z 400 ± 0.5 derived from the asphaltene sample and the MCAD mass spectrum of these ions measured at a collision energy of 30 eV is shown in Figure 4.1.

Due to the enormous complexity of the asphaltene samples, even ions of one nominal m/z value contain multiple isobaric and isomeric ions. This is demonstrated in the mass spectrum of molecular ions of m/z 400 ± 0.5 derived from the asphaltene sample (Figure 4.1a). As a result, the MS/MS spectrum of these ions measured at an MCAD collision energy of 30 eV are derived from multiple fragmenting ions (Figure 4.1b). Consequently, it is impossible to associate fragment ions with their respective fragmenting ions. However, the sizes of the smallest aromatic cores can be determined based on the lowest m/z ions observed (m/z 315 in Figure 4.1b). The maximum size of alkyl chains can be also determined to be 75 Da based on the mass difference between ions of the smallest aromatic cores (m/z 315) and the precursor ion (m/z 400). Overall, based on this data analysis approach, the maximum number of carbons in the alkyl chains is approximately six and the smallest aromatic core is 315 Da in the asphaltene compounds of 400 ± 0.5 Da. This data analysis method is referred to as the conventional method in this article.

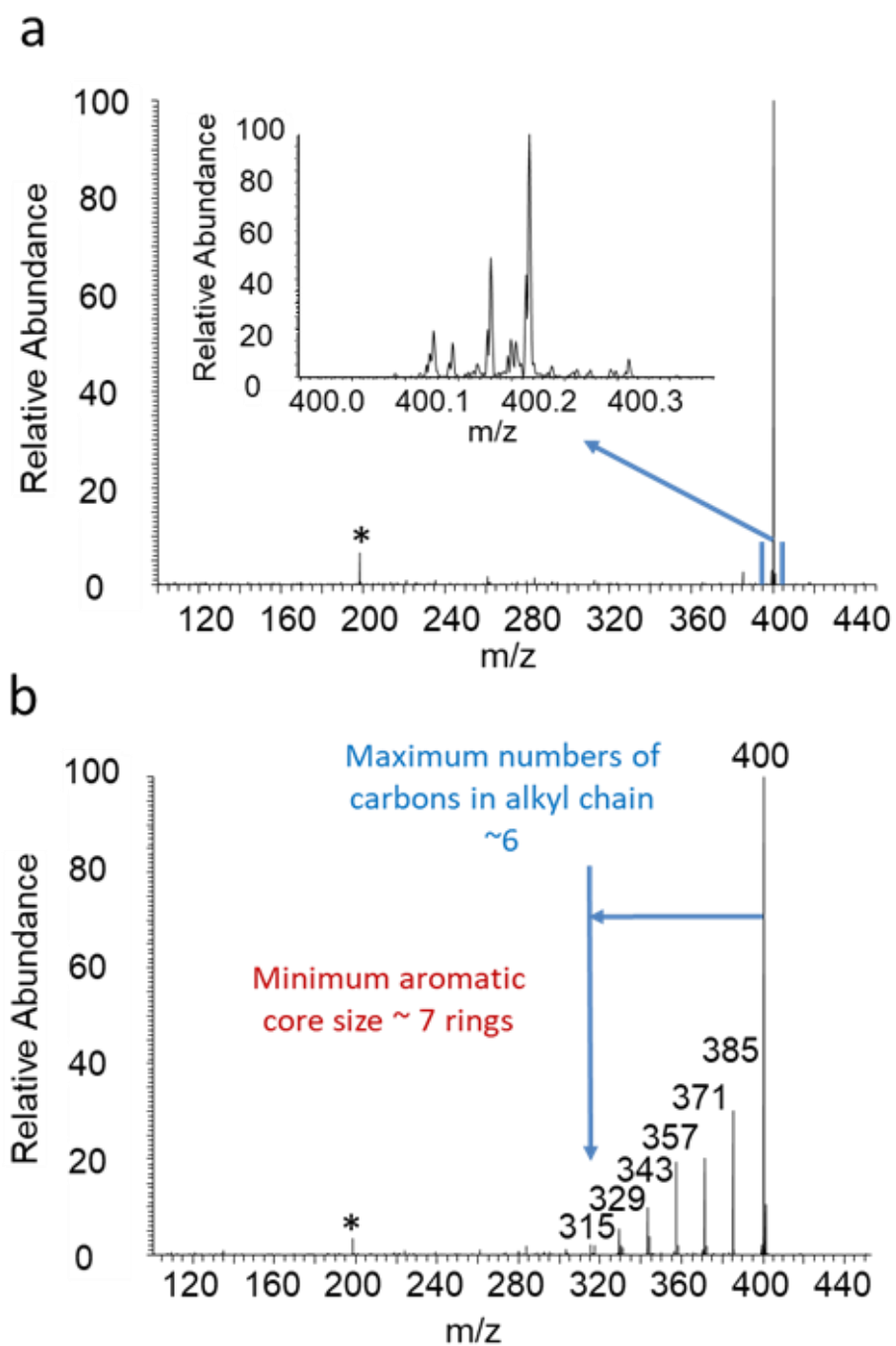


Figure 4.1 A mass spectrum of molecular ions of $m/z 400 \pm 0.5$ derived from the asphaltene sample (a), and a MS/MS spectrum of ions of ions of $m/z 400 \pm 0.5$ derived from the asphaltene sample measured at a MCAD collision energy of 30 eV (b). * indicates instrumental noise.

4.3.2 MCAD Fragmentation Patterns of Molecular Ions of Single-core and Multicore Model Compounds

To employ the conventional approach for analysis of high-resolution MS/MS data from asphaltenes, it is necessary to explore the fragmentation patterns of asphaltene model compounds. In earlier studies, the fragmentation patterns of a wide range of ionized asphaltene model compounds upon ion-trap CAD have been revealed.^{7,31} MCAD fragmentation patterns have been also reported for several ionized asphaltene model compounds.^{32,33} In general, fragmentation of ionized single core compounds results in the loss of only one alkyl group during ion-trap CAD^{7,31} and multiple alkyl groups during MCAD^{32,33}, generating fragment ions with similar RDBE values with their fragmenting ions. In comparison, fragmentation of ionized multicore compounds results in the loss of aromatic cores and thus generated fragment ions with a lower RDBE and lower m/z-value compared to the fragmenting ions.

The MCAD of two ionized model compounds is discussed here for a brief demonstration. MCAD mass spectra of an ionized model single-core compound, 2,4,7,9-tetrakis(decyl)pyrene, and an ionized multicore model compound, 1,4-di(pyren-1-yl)butane, are shown in Figure 4.2a and 4.2b, respectively. In Figure 4.2a, MCAD of the single-core (2,4,7,9-tetrakis(decyl)pyrene) ion resulted in the loss of multiple alkyl groups and generated fragment ions with the same RDBE as the precursor ion. As a result, a “horizontal streak” (indicated by arrow) can be observed in the plot of RDBE values as a function of carbon number (referred to as RDBE plot, Figure 4.2c). By comparison, MCAD of the multicore (1,4-di(pyren-1-yl)butane) ions resulted in the loss of a pyrene core and thus generated fragment ions with a significantly lower RDBE and m/z-values compared to the fragmenting ions. As a result, a “diagonal streak” (indicated by an arrow) can be observed in the RDBE plot (Figure 4.2d).

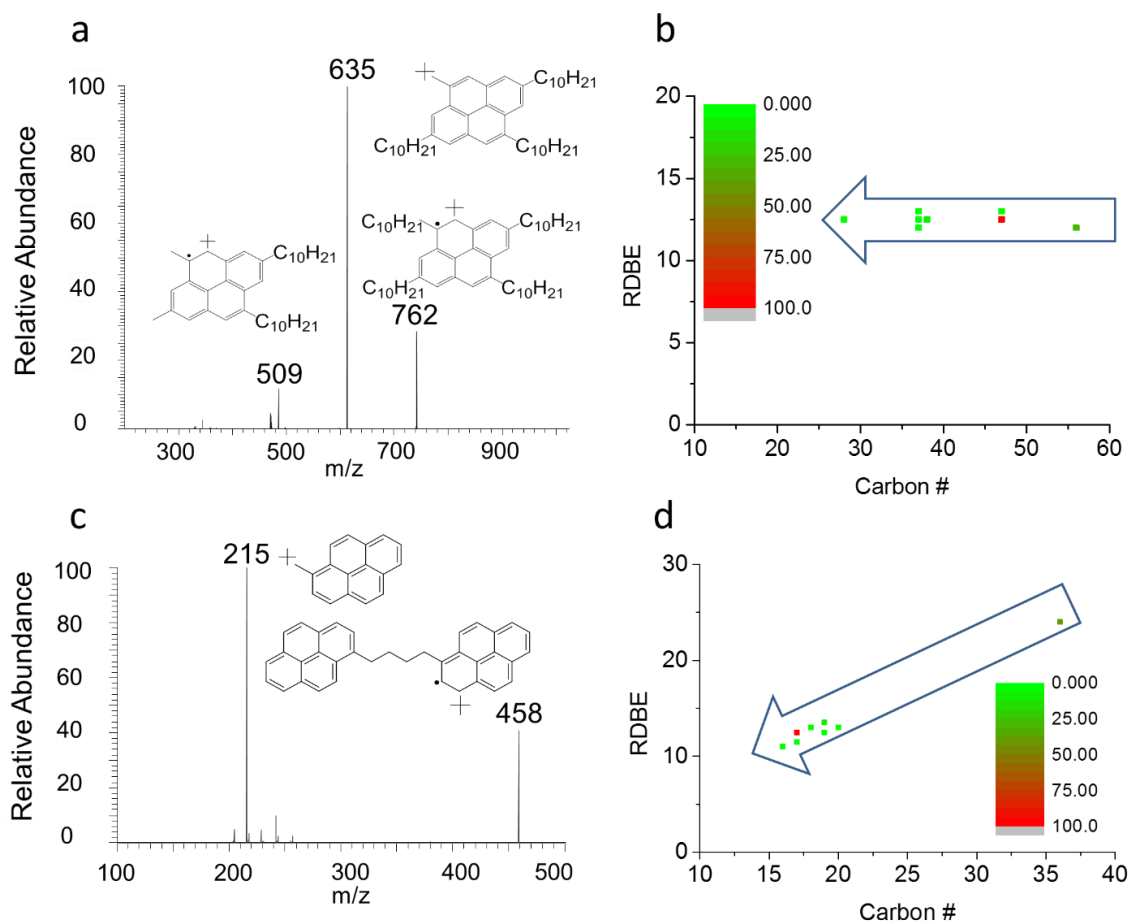


Figure 4.2 An MCAD spectrum (a) and a plot of RDBE values as a function of the number of carbons (b) of an ionized single-core compound measured at MCAD at a collision energy of 30 eV. An MCAD spectrum (c) and a plot of RDBE values as a function of the number of carbons (d) of an ionized multicore compound measured at MCAD at a collision energy of 60 eV. The ions are represented by the dots in the RDBE plot. The ions' relative signal intensities are indicated by the color of the dots.

Based on the model compound studies, the molecular ions of single-core compounds and their fragment ions can be associated based on their similar RDBE values.^{7,31-33} Consequently, instead of analyzing all the ions together in one MS/MS spectrum, it is possible to analyze the fragmenting and fragment ions derived from single-core compounds of different RDBE values separately in a mixture predominately composed of single-core compounds. This approach (referred to as the new approach) may allow more information over aromatic core and alkyl chains to be revealed compared to the conventional approach. However, the ions of multicore compounds and their fragments cannot be associated based on their RDBE values. This limitation will be discussed further in the next few result sections.

The possibility of applying the new approach is explored using a model compound mixture composed of three isobaric compounds (Table 1): 2-(3-(naphthalen-2-yl)propyl)pyrene (370.17 Da), 4,9-dihexylpyrene (370.27 Da), and 5-octadecyl-2,3-dihydro-1H-indene (370.36 Da). An RDBE plot of the molecular ions derived from model compound mixtures before fragmentation and an RDBE plot of the molecular ions and the fragment ions derived from model compound mixtures measured at an MCAD collision energy 30 eV are shown Figure 4.3. The fragment ions and the fragmenting ions derived from the two single-core compounds have similar RDBE values (indicated by red dashed lines, Figure 4.3b). As a result, ions of similar RDBE values are derived from the same group of fragmenting ions. Consequently, a mass spectrum can be re-constructed (referred to as reconstructed spectrum) for each group of ions in “horizontal streak” 1, and 2 (Figures 4.3c and 4.3d, respectively). These reconstructed spectra allow determination of the aromatic core sizes and the total number of carbons in alkyl chains of the two single-core model compounds when they are presented in the same mixture. However, the “diagonal streak” is still observed during MCAD of molecular ion of the multicore compound (Figure 4.3b). The fragment ions derived from the multicore model compound have different RDBE values than their fragmenting ion. Consequently, the size of the aromatic core and the total number of carbons cannot be determined for multicore compounds in a mixture using this method. Overall, the model compound mixture study suggests that the conventional method is suitable for mixtures that are predominantly single-core

compounds and is not expected to provide accurate information for mixtures that contain a significant abundance of multicore compounds.

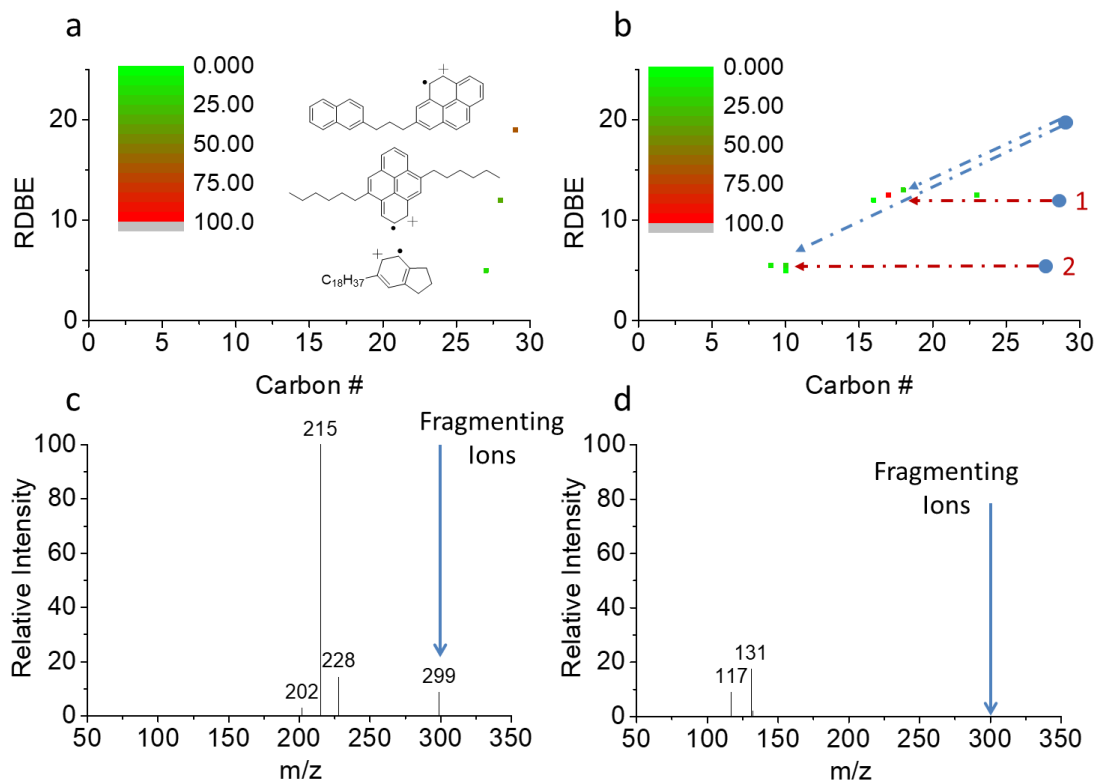


Figure 4.3 Plots of RDBE values as a function of the number of carbons in the molecular ions of three isobaric model compounds (a) and their fragment ions obtained upon MCAD at a collision energy of 30 eV (b) with the “horizontal streaks” 1 and 2 labeled. Reconstructed spectra of ions in “horizontal streak” 1 and 2 are shown in (c) and (d), respectively. The ions are represented by the dots in the RDBE plot. The ions’ relative signal intensities are indicated by the color of the dots. The horizontal and diagonal streaks are indicated by red arrow and blue arrows.

4.3.3 Interpretation of MS Data via the Reconstructed Mass Spectrum

Based on the fragmentation patterns of ionized single-core model compounds, their molecular ions and fragment ions can be associated based on the similar RDBE values. This is observable as “horizontal streaks” in the RDBE plots of ionized model compound mixtures. The sizes of the smallest aromatic cores and the maximum numbers of carbons in alkyl chains of the single-core compounds in a model compound mixture can be determined for each “horizontal streak” based on the the approach described earlier. In this section, the new approach is employed for analysis of the MCAD mass spectra of ions derived from an asphaltene sample. RDBE vs carbon number plots of ions of m/z 400 ± 0.5 derived from the full mass spectrum of the asphaltene sample and after MCAD with a collision energy of 32 eV are shown in Figure 4.4.

The molecular ions of m/z 400 ± 0.5 derived from the asphaltene samples fall into three groups based on the RDBE values (colored circles, Figure 4.4a), and have RDBE values of ~ 12 , ~ 18 , and ~ 25 , respectively. Three “horizontal streaks” were observed for each group of fragmenting ions upon MCAD fragmentation (colored arrows, Figure 4.4b). The weighted (signal intensity) average RDBE value of the molecular ions of m/z 400 ± 0.5 is 18.6 and the weighted average RDBE values of the ions of m/z 400 ± 0.5 measured at a MCAD collision energy 32 eV is 19.9. As discussed above in the model compound study, MCAD of ions derived from multicore compounds generate fragment ions of lower RDBE values than their precursor ions. In comparison, MCAD of ions derived from single-core compounds introduce fragment ions with slightly higher RDBE values due to loss of hydrogen atoms. This causes a slight increase in the weighted average RDBE values of the ions upon MCAD. Therefore, the absence of decrease in the average RDBE values upon MCAD fragmentation indicates that the single-core structure is predominant in these ions.³⁴ Overall, these observations suggest that the fragment ions in each “horizontal streak” are generated by MCAD of fragmenting ions of similar RDBE values. Therefore, the new approach can be employed to analyze these ions. As demonstrated in the above model compound analysis, a reconstructed spectrum can be obtained for the ions within each “horizontal streak”.

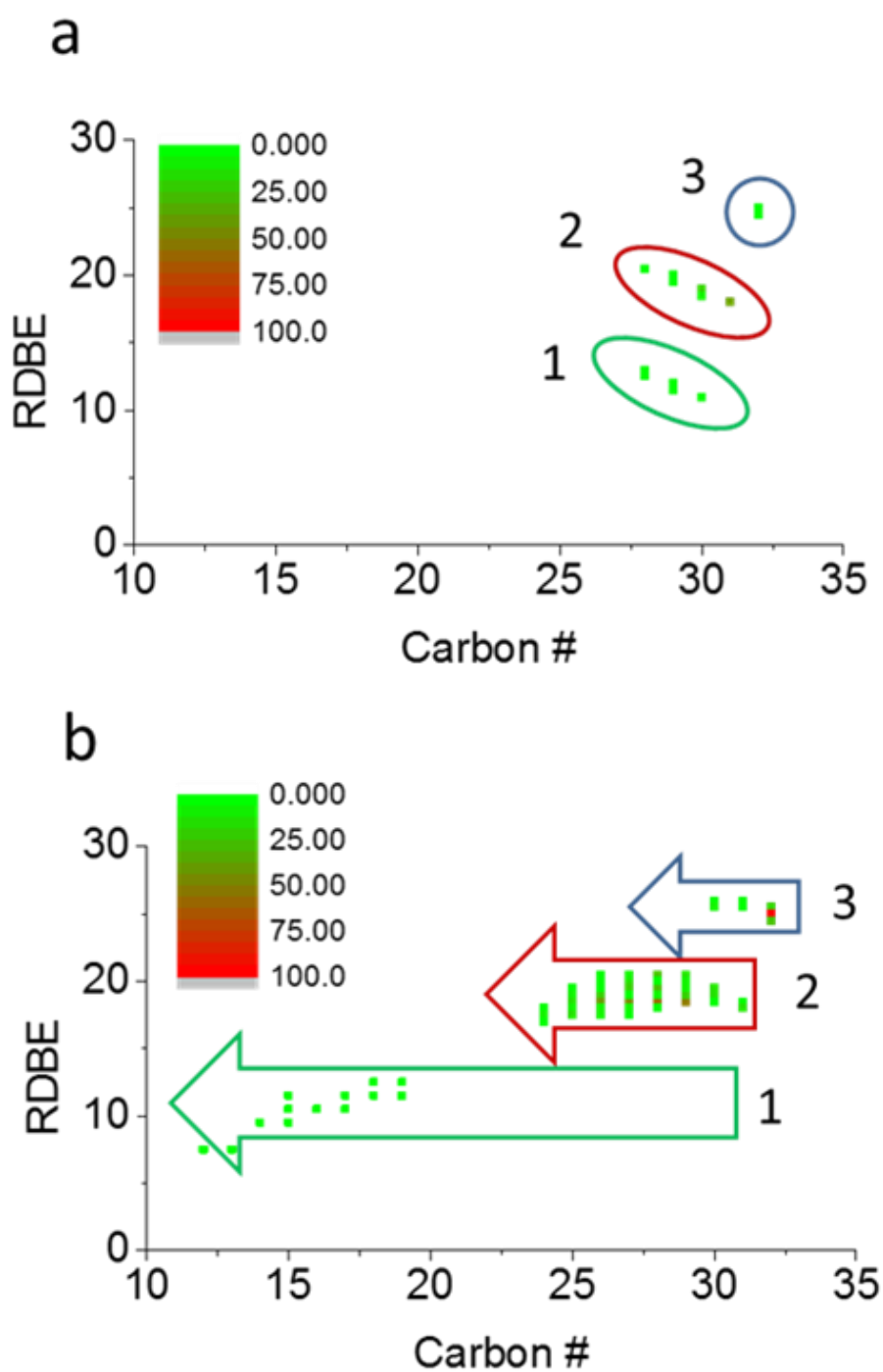


Figure 4.4. Plots of RDBE values as a function of the number of carbons in molecular ions of $m/z 400 \pm 0.5$ derived from the asphaltene sample (a) and their fragment ions obtained upon MCAD at a collision energy of 32 eV (b). The ions are represented by the dots in the RDBE plot. The ions' relative signal intensities are indicated by the color of the dots.

The re-constructed MS/MS spectra for “horizontal streaks” 1, 2, and 3 are shown in Figures 4.5a, 4.5b, and 4.5c, respectively. In Figure 4.5a, the re-constructed MS/MS spectrum for ions of m/z 400 and an RDBE of ~ 12 showed maximum loss of 13 carbons. This suggests that the ions are derived from compounds with smallest aromatic core of ~ 170 Da and with alkyl chains containing a maximum of 13 carbons. In Figure 4.5b, the re-constructed MS/MS spectrum showed a maximum loss of a heptyl group from ions of m/z 400 and of RDBE value ~ 20 . This suggests that the ions are derived from compounds with a smallest aromatic core of ~ 300 Da and with alkyl chains containing maximum seven carbons. Interestingly, the re-constructed MS/MS spectrum in Figure 4.5c showed a maximum loss of ethyl groups from fragmenting ions of m/z 400 and RDBE ~ 25 . This observation suggests that these ions are derived from single-core compounds with large aromatic cores (~ 370 Da) and only two carbons in the alkyl chains. It worth noting that single-core compounds with large aromatic cores have been previously observed in asphaltene using AFM.³⁵ However, the AFM findings have raised concerns since ions of similar structures have not been observed in conventional MS/MS spectra. In this regard, this reconstructed MS/MS spectrum provides a mass spectrometric support for the presence of such molecules.

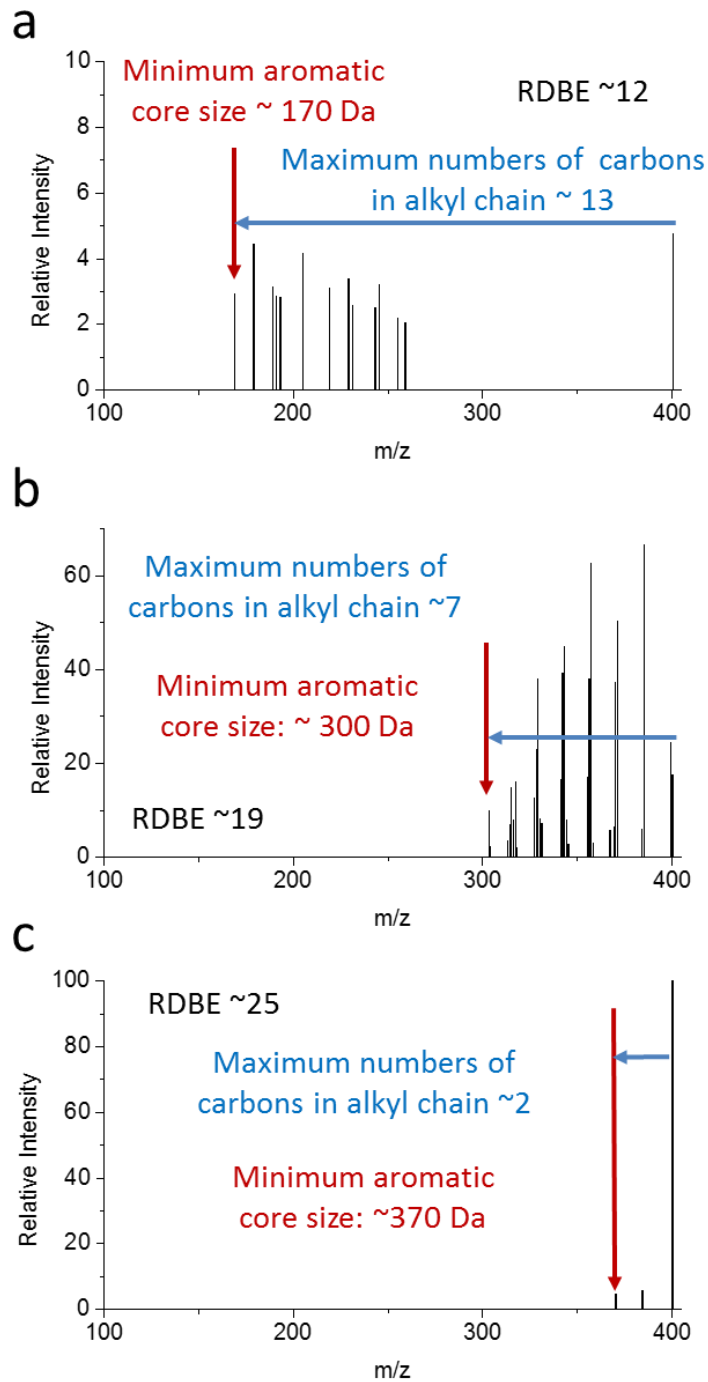


Figure 4.5 The re-constructed spectra that correspond to ions in fragmentation series 1 (a), fragmentation series 2 (b), and fragmentation series 3 (c) that are highlighted in figure 4b, respectively

4.3.4 Investigation of Ions of m/z 400 ± 0.5 , 500 ± 0.5 , 600 ± 0.5 , and 700 ± 0.5 Derived from an Asphaltene Sample

To provide a better overview of the molecular structure of the asphaltene sample, the new approach is employed to explore the molecular structure of ions of m/z 400 ± 0.5 , 500 ± 0.5 , 600 ± 0.5 , and 700 ± 0.5 derived from the asphaltene sample. The RDBE plots of ions of m/z 400 ± 0.5 , 500 ± 0.5 , 600 ± 0.5 , and 700 ± 0.5 derived from the asphaltene sample are shown in Figure 4.6. The weighted (signal intensity) average RDBE values for ions of m/z 400 ± 0.5 , 500 ± 0.5 , 600 ± 0.5 , and 700 ± 0.5 are 18.6, 18.9, 18.1, and 18.4, respectively. The RDBE plots of ions of m/z 400 ± 0.5 , 500 ± 0.5 , 600 ± 0.5 , and 700 ± 0.5 measured at after MCAD are shown in Figure 4.7. The weighted average RDBE values for ions of m/z 400 ± 0.5 , 500 ± 0.5 , 600 ± 0.5 , and 700 ± 0.5 are 19.9, 20.4, 18.2, and 14.3 respectively. Upon MCAD, the weighted average RDBE values changed by +1.3, +1.5, +0.1, and -4.1 for ions of m/z 400 ± 0.5 , 500 ± 0.5 , 600 ± 0.5 , and 700 ± 0.5 , respectively (Table 2). Overall, these observations suggest that single-core compounds are predominant in ions of m/z 400 ± 0.5 and 500 ± 0.5 , multicore compounds are more significant in ions of m/z 600 ± 0.5 , and multicore compounds are most significant in ions of m/z 700 ± 0.5 . As a result, the new approach is suitable for analysis of ions of m/z 400 ± 0.5 and 500 ± 0.5 , reasonably suitable for analysis of ions of m/z 600 ± 0.5 but should not be employed in analysis of ions of m/z 700 ± 0.5 .

In Figure 4.6, molecular ions of m/z 400 ± 0.5 contain three groups of ions of RDBE ~ 12 , ~ 20 , and ~ 26 ; molecular ions of m/z 500 ± 0.5 contain four groups of ions of RDBE ~ 11 , ~ 18 , ~ 25 , and ~ 32 ; molecular ions of m/z 600 ± 0.5 contain four groups of ions of RDBE ~ 10 , ~ 17 , ~ 24 , and ~ 31 ; and molecular ions of m/z 700 ± 0.5 contain five groups of ions of RDBE ~ 9 , ~ 16 , ~ 23 , ~ 30 , and ~ 37 . Although RDBE values differ slightly for each group, overall the molecular ions can be clustered into five groups based on their RDBE values: group 1 (RDBE ~ 11), group 2 (RDBE ~ 18), group 3 (RDBE ~ 25), group 4 (RDBE ~ 31 , not observed in ions of m/z 300 ± 0.5) and group 5 (RDBE ~ 37 , only observed in ions of m/z 700 ± 0.5). For each group observed in the RDBE plots of ionized asphaltenes of m/z 400 ± 0.5 , 500 ± 0.5 , 600 ± 0.5 , and 700 ± 0.5 without fragmentation (Figure 4.6), a “horizontal streak” of similar RDBE values can be observed in RDBE plots of these ions after fragmentation (Figure 4.7).

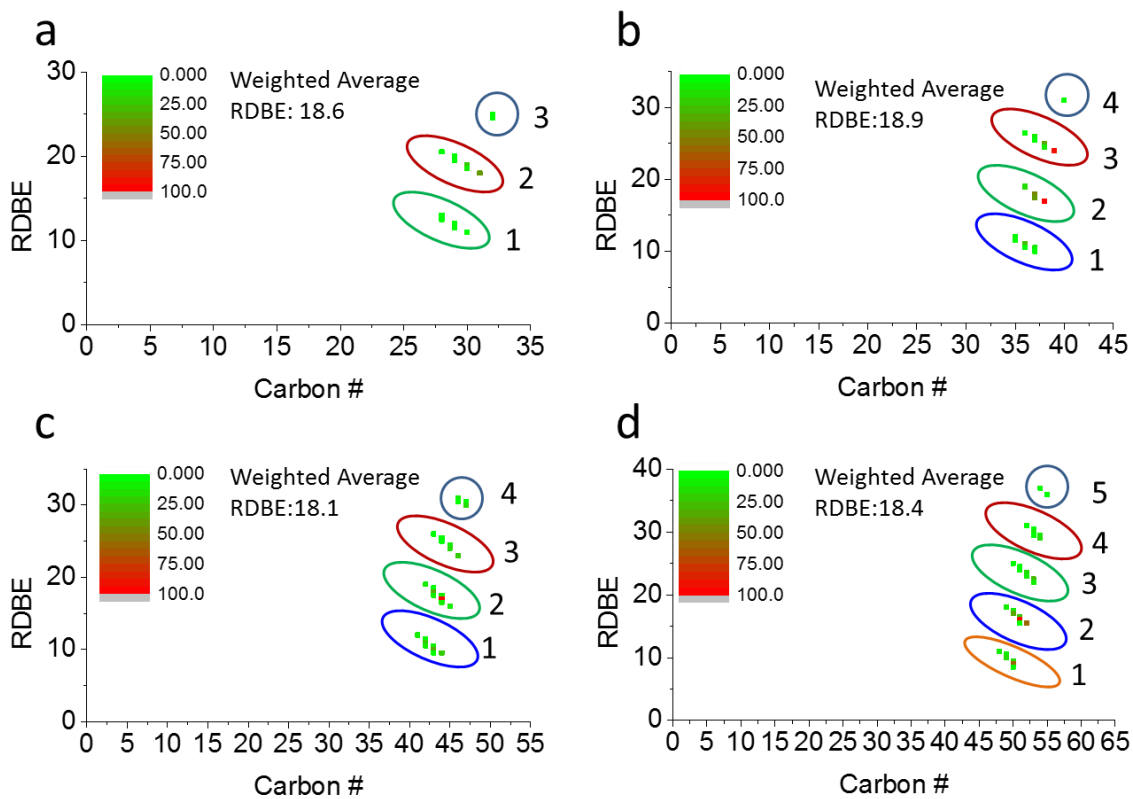


Figure 4.6 Plots of RDBE values as a function of the number of carbons in molecular ions of m/z 400±0.5 (a), 500±0.5 (b), 600±0.5 (c), and 700±0.5 (d) derived from the asphaltene sample. The ions are clustered into 5 groups and is indicated by the numbers next to the circle. The ions are represented by the dots in the RDBE plot. The ions' relative signal intensities are indicated by the color of the dots.

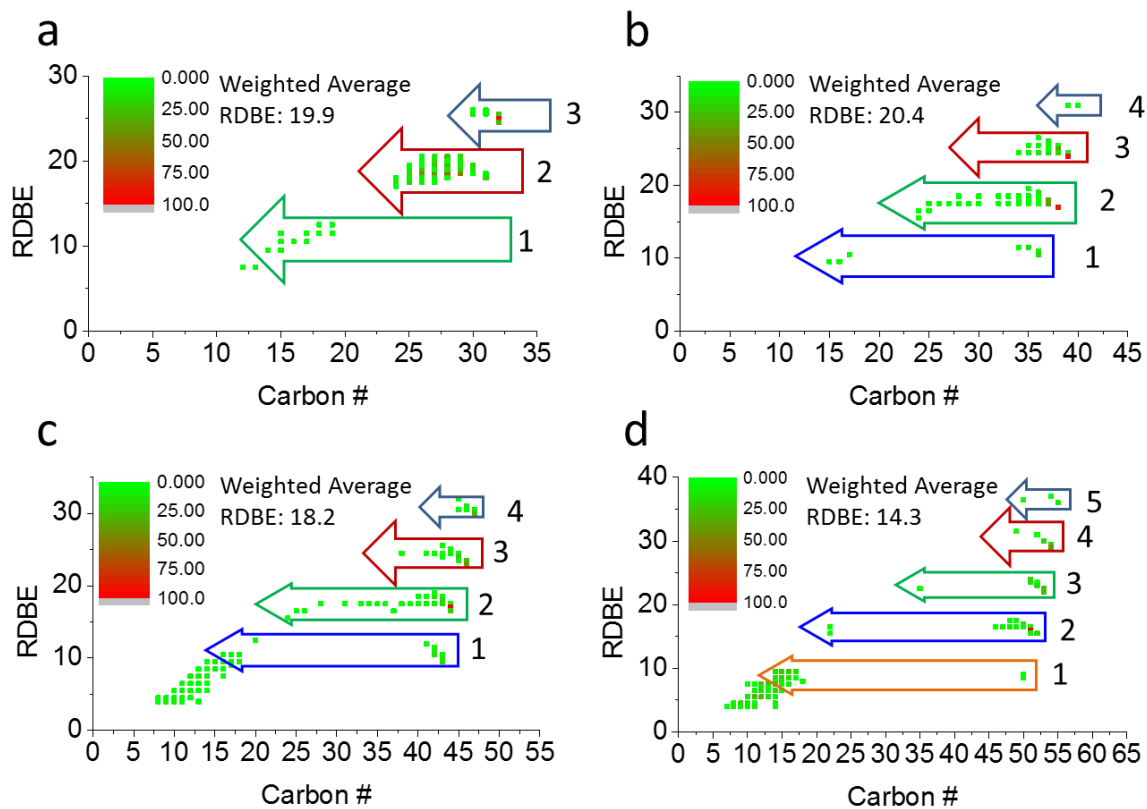


Figure 4.7 Plots of RDBE values as a function of the number of carbons in molecular ions of m/z 400 ± 0.5 (a), 500 ± 0.5 (b), 600 ± 0.5 (c), and 700 ± 0.5 (d) derived from the asphaltene sample measured at MCAD collision energy 32 eV, 40 eV, 48 eV, and 56 eV, respectively. The ions are clustered into 5 groups, indicated by the numbers next to each cluster. The ions are represented by the dots in the RDBE plot and the relative signal intensities are indicated by the color of the dots.

The reconstructed spectra derived from MCAD mass spectrum for ions of m/z 400 ± 0.5 derived from the asphaltene sample have been discussed above (Figure 4.4). Those for ions of m/z 500 ± 0.5 , 600 ± 0.5 , and 700 ± 0.5 derived from the asphaltene sample are shown in Figures 4.8 to S4.10. The information on the smallest size of aromatic cores, maximum number of carbons in the alkyl chains, and relative abundance of single-core and multicore compounds in ions of different m/z derived from the asphaltene sample are summarized in Table 4.2. Due to the significant abundances of multicore ions present at m/z 700 ± 0.5 , the information derived from these ions is expected to be inaccurate and is not discussed further in this study.

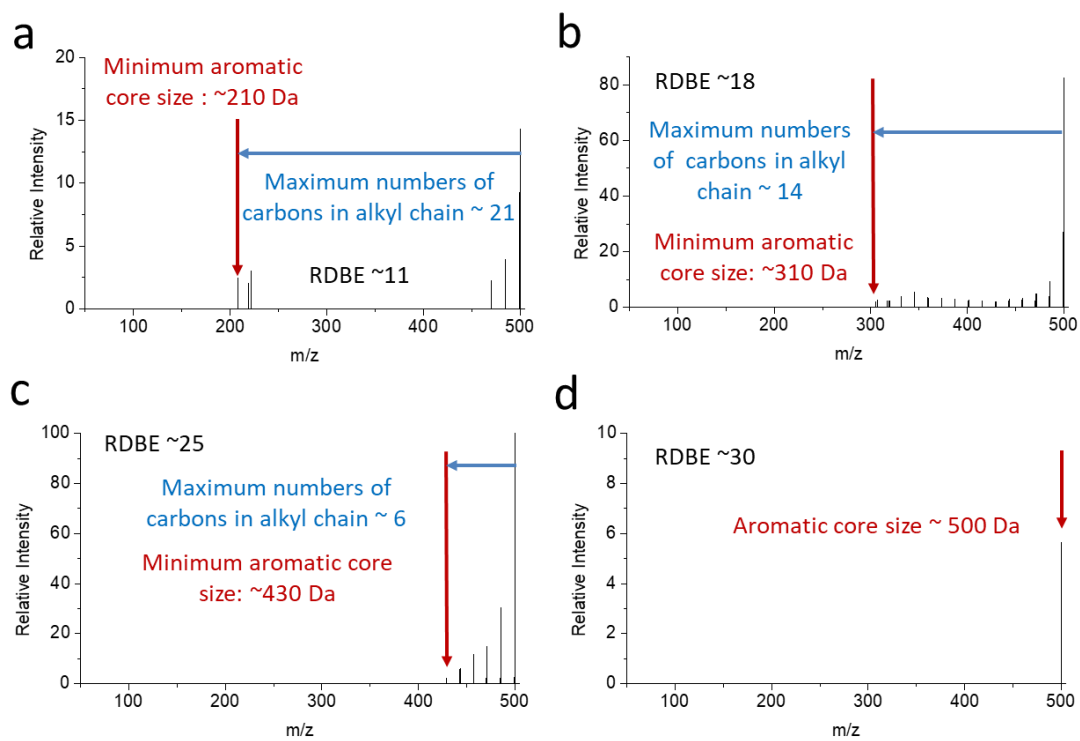


Figure 4.8 Re-constructed spectra that correspond to ions in fragmentation series 1 (a), fragmentation series 2 (b), fragmentation series 3 (c), and fragmentation series 4 (d) that are highlighted in figure 7b, respectively

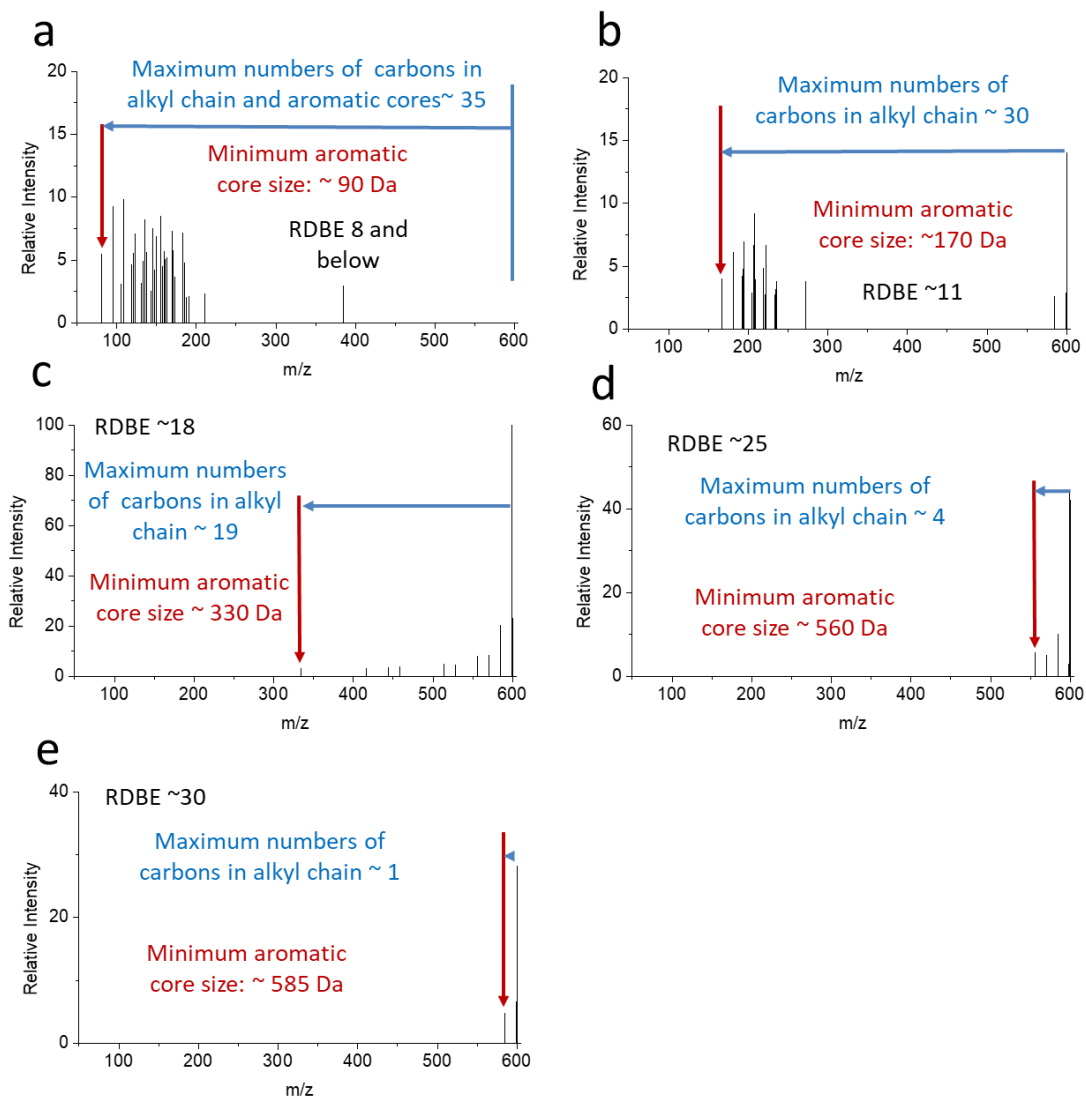


Figure 4.9 Re-constructed spectra that correspond to ions in fragmentation series 1 (a), fragmentation series 2 (b), fragmentation series 3 (c), fragmentation series 4 (d) and fragmentation series 5 (e) that are highlighted in figure 7c, respectively

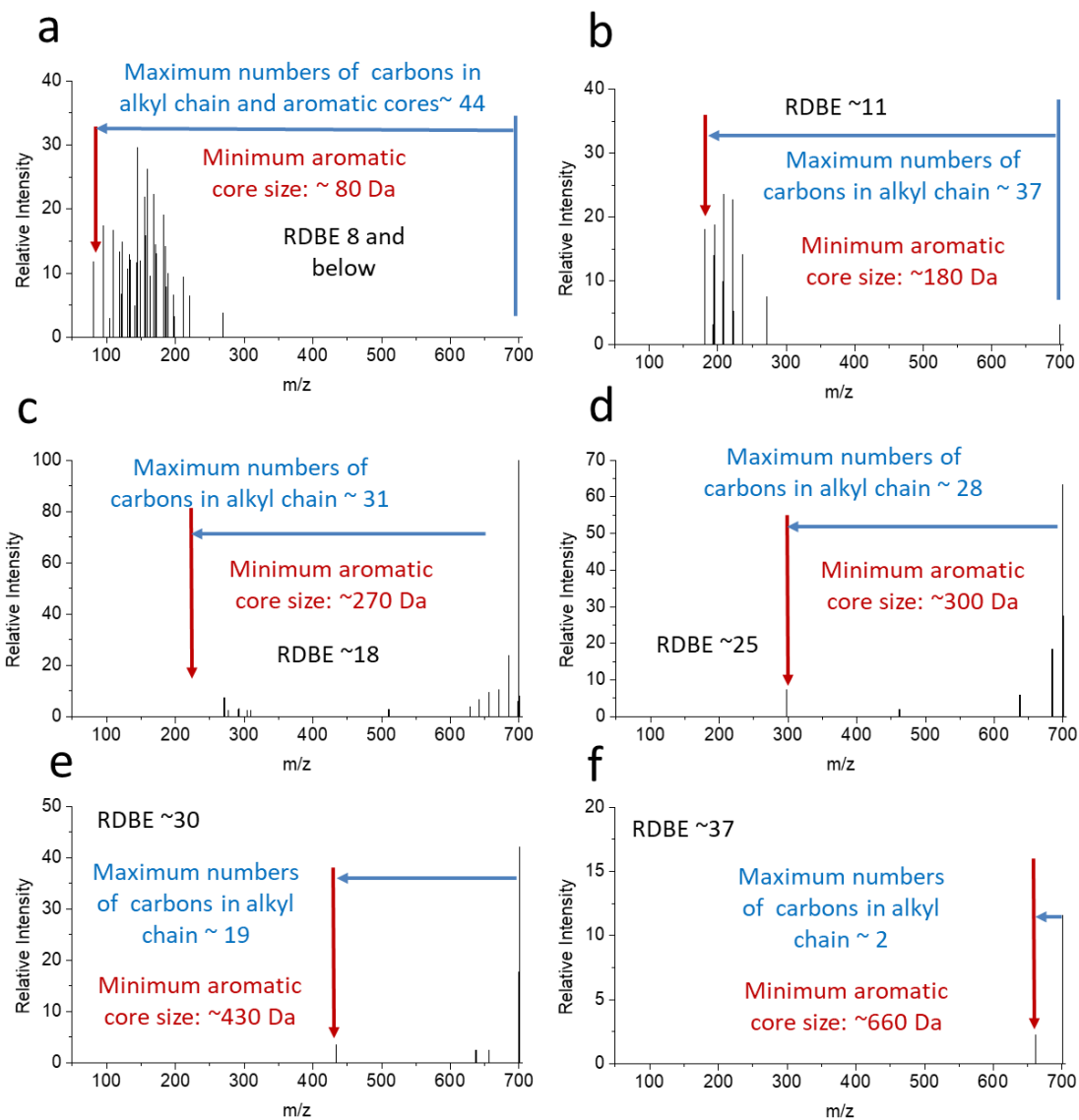


Figure 4.10 Re-constructed spectra that correspond to ions in fragmentation series 1 (a), fragmentation series 2 (b), fragmentation series 3(c), fragmentation series 4(d), fragmentation series 5 (e), and fragmentation series 6 (f) that are highlighted in figure 7d, respectively.

Ions of RDBE ~ 11 (group 1) from ions of m/z 400 ± 0.5 , 500 ± 0.5 , and 600 ± 0.5 have similar smallest aromatic cores sizes (~ 200 Da) but the maximum number of carbons in the alkyl chains increases significantly as the m/z values of the ions increase (13, 21, and 30, respectively). In ions of RDBE ~ 18 (group 2) from ions of m/z 400 ± 0.5 , 500 ± 0.5 , and 600 ± 0.5 , the sizes of the smallest aromatic cores increase slightly (300 Da, 310 Da, and 330 Da, respectively) and the maximum number of carbons in the alkyl chains significantly increases (7, 14, and 19, respectively) as the m/z values of the fragmenting ions increases. In comparison, in ions of RDBE ~ 25 (group 3) from ions of m/z 400 ± 0.5 , 500 ± 0.5 , and 600 ± 0.5 , the sizes of the smallest aromatic cores significantly increases (370 Da, 430 Da, and 560 Da, respectively) as the m/z values of the fragmenting ions increases, while the maximum numbers of carbons in alkyl chains remain small (2, 6, and 4, respectively). Similar trends were also observed in ions of RDBE ~ 31 (group 4) from ions of m/z 500 ± 0.5 and 600 ± 0.5 : the sizes of the smallest aromatic cores increase significantly (500 Da and 585 Da, respectively) while the total numbers of carbons in the alkyl chains increases slightly (0 and 1, respectively) as the m/z values of the ions increase. Overall, for the ions investigated in this study, the smallest size of the aromatic cores increases as the m/z value and the RDBE values of the ions increases in the. The maximum numbers of carbons in alkyl chains increase as the m/z values of the ions increase but decrease as the RDBE values of the ion increases. In addition, the relative abundance of multicore compounds increases as the m/z values of the ions increase. Nevertheless, due to the limited numbers of ions and asphaltene samples investigated in this study, these observations should not be generalized to asphaltene molecular structures as a whole.

Table 4.2 Comparison of the size of the smallest aromatic cores, maximum numbers of carbons in alkyl chains, and relative abundances of single-core and multicore compounds in ions of different m/z derived from the asphaltene sample.

		m/z 400	m/z 500	m/z 600	m/z 700
Group 1 RDBE ~ 11	size of the smallest aromatic cores	170 Da	210 Da	170 Da	180 Da
	maximum numbers of carbons in alkyl chains	13	21	30	37
Group 2 RDBE ~ 18	size of the smallest aromatic cores	300 Da	310 Da	330 Da	270 Da
	maximum numbers of carbons in alkyl chains	6	14	19	31
Group 3 RDBE ~ 25	size of the smallest aromatic cores	370 Da	430 Da	560 Da	300 Da
	maximum numbers of carbons in alkyl chains	2	6	4	28
Group 4 RDBE ~ 31	size of the smallest aromatic cores	N. A	500 Da	585 Da	430 Da
	maximum numbers of carbons in alkyl chains	N. A	0	1	19
Group 5 RDBE ~ 37	size of the smallest aromatic cores	N. A	N. A	N. A	660 Da
	maximum numbers of carbons in alkyl chains	N. A	N. A	N. A	2
single-core vs. multicore	change in weighted average RDBE	1.3 (single-core dominant)	1.5 (single-core dominate)	0.1 (insignificant multicore)	-4.1 (significant multicore)

4.4 Conclusions

In this study, a new method for in-depth analysis of MS/MS spectrometric data derived from asphaltene sample is introduced and employed for analysis of an asphaltene sample. This method allows the association of fragmented ions with their respective single-core precursor ions based on the RDBE value. Because of the association of fragment ions and their corresponding fragmenting ions, the original MS/MS spectrum can be simplified into several reconstructed spectra. Each reconstructed spectrum corresponds to a group of island ions and their fragment ions with similar RDBE values. The reconstructed spectra provide in-depth analysis that reveals more structural information concerning the aromatic cores and alkyl chains compared to the conventional approach.

Ions of m/z 400 ± 0.5 , 500 ± 0.5 , 600 ± 0.5 , and 700 ± 0.5 derived from the asphaltene sample were analyzed by using the new approach. As summarized in Figure 4.11, the size of the smallest aromatic cores increases with both the m/z value and RDBE values of the ions; the maximum number of carbons in the alkyl chains increases with the m/z value of the ions but decreases with the RDBE values of the ions. In addition, the relative abundance of multicore compounds increases with the m/z value of the ions. Overall, the new approach employed in this study provides in-depth structural information for mixtures dominated by single-core compounds. However, due to the lack of knowledge of the fragmentation patterns of multicore ions in the mixtures, this approach is not expected to perform well in mixtures containing significant amounts of multicore compounds. In addition, this analysis, like many MS-based methods, is inevitably affected by the ionization bias derived from the ionization method employed. As a result, this analysis only provides qualitative information.

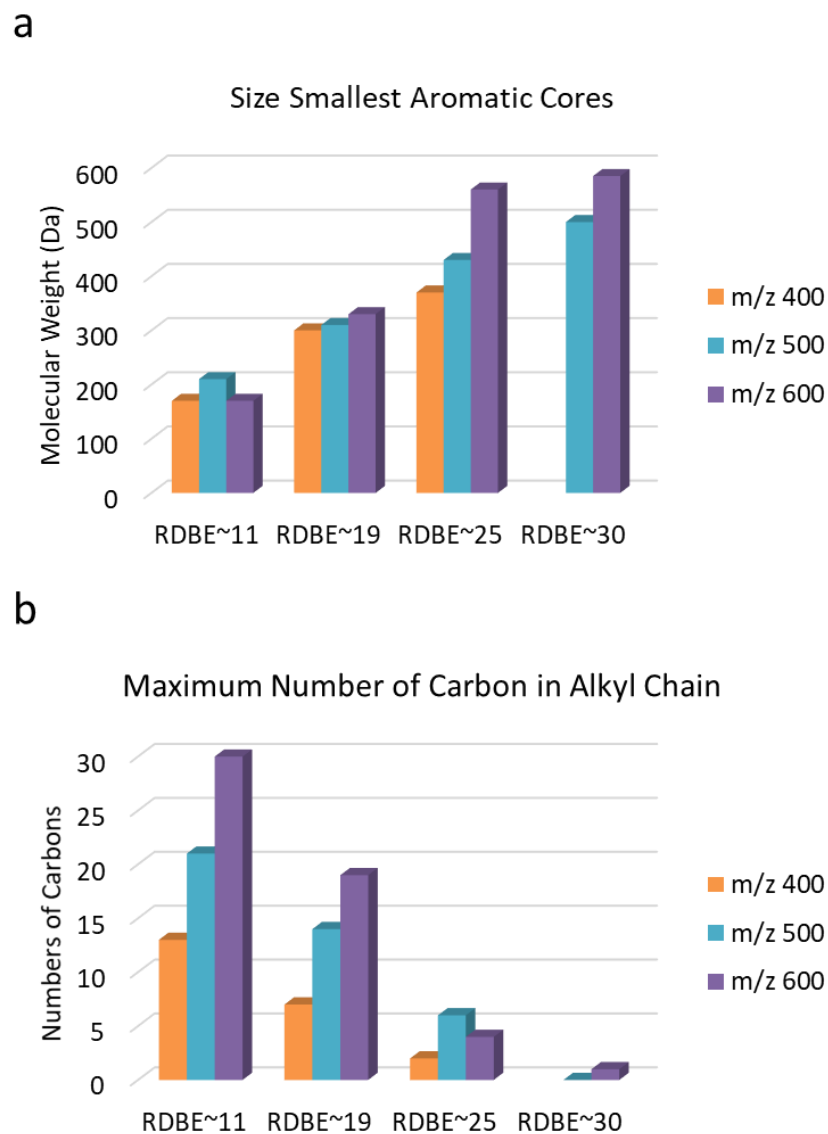


Figure 4.11 A summary of the sizes of smallest aromatic core (a) and maximum numbers of carbon in alkyl chains (b) in the ions of m/z 400, 500, and 600 derived from the asphaltene samples.

4.5 References

- (1) Mullins, O. C. The Asphaltenes. *Annu. Rev. Anal. Chem.* **2011**, *4*, 393-418.
- (2) Trbovich, M.; King, G. In *SPE International Symposium on Oilfield Chemistry*; Society of Petroleum Engineers, 1991.
- (3) Hubbert, M. K. Energy from Fossil Fuels. *Science.* **1949**, *109*, 103-109.
- (4) Mullins, O. C.; Sabbah, H.; Eyssautier, J.; Pomerantz, A. E.; Barré, L.; Andrews, A. B.; Ruiz-Morales, Y.; Mostowfi, F.; McFarlane, R.; Goual, L. Advances in Asphaltene Science and the Yen–Mullins Model. *Energy Fuels.* **2012**, *26*, 3986-4003.
- (5) Marshall, A. G.; Rodgers, R. P. Petroleomics: Chemistry of the Underworld. *Proc. Natl. Acad. Sci.* **2008**, *105*, 18090-18095.
- (6) Mullins, O. C.; Sheu, E. Y.; Hammami, A.; Marshall, A. G. *Asphaltenes, Heavy Oils, and Petroleomics*; Springer Science & Business Media: New York, 2007.
- (7) Sabbah, H.; Morrow, A. L.; Pomerantz, A. E.; Zare, R. N. Evidence for Island Structures as the Dominant Architecture of Asphaltenes. *Energy Fuels.* **2011**, *25*, 1597-1604.
- (8) Sabbah, H.; Morrow, A. L.; Pomerantz, A. E.; Mullins, O. C.; Tan, X.; Gray, M. R.; Azyat, K.; Tykwinski, R. R.; Zare, R. N. Comparing Laser Desorption/Laser Ionization Mass Spectra of Asphaltenes and Model Compounds. *Energy Fuels.* **2010**, *24*, 3589-3594.
- (9) Quann, R. J.; Jaffe, S. B. Structure-Oriented Lumping: Describing the Chemistry of Complex Hydrocarbon Mixtures. *Ind. Eng. Chem. Res.* **1992**, *31*, 2483-2497.
- (10) Strausz, O. P.; Mojelsky, T. W.; Lown, E. M. The Molecular Structure of Asphaltene: An Unfolding Story. *Fuel.* **1992**, *71*, 1355-1363.
- (11) Strausz, O. P.; Peng, P. a.; Murgich, J. About the Colloidal Nature of Asphaltenes and the Mw of Covalent Monomeric Units. *Energy Fuels.* **2002**, *16*, 809-822.
- (12) Alvarez-Ramírez, F.; Ruiz-Morales, Y. Island Versus Archipelago Architecture for Asphaltenes: Polycyclic Aromatic Hydrocarbon Dimer Theoretical Studies. *Energy Fuels.* **2013**, *27*, 1791-1808.
- (13) Marshall, A. G.; Rodgers, R. P. Petroleomics: The Next Grand Challenge for Chemical Analysis. *Acc. Chem. Res.* **2004**, *37*, 53-59.
- (14) Badre, S.; Goncalves, C. C.; Norinaga, K.; Gustavson, G.; Mullins, O. C. Molecular Size and Weight of Asphaltene and Asphaltene Solubility Fractions from Coals, Crude Oils and Bitumen. *Fuel.* **2006**, *85*, 1-11.

- (15) Majumdar, R. D.; Montina, T.; Mullins, O.; Gerken, M.; Hazendonk, P. Insights into Asphaltene Aggregate Structure Using Ultrafast Mas Solid-State 1h Nmr Spectroscopy. *Fuel*. **2017**, *193*, 359-368.
- (16) Carvalho, V. V.; Vasconcelos, G. A.; Tose, L. V.; Santos, H.; Cardoso, F. M.; Fleming, F.; Romão, W.; Vaz, B. G. Revealing the Chemical Characterization of Asphaltenes Fractions Produced by N-Methylpyrrolidone Using Ftir, Molecular Fluorescence, 1 H Nmr, and Esi (\pm) Ft-Icr Ms. *Fuel*. **2017**, *210*, 514-526.
- (17) Sharma, A.; Groenzin, H.; Tomita, A.; Mullins, O. C. Probing Order in Asphaltenes and Aromatic Ring Systems by Hrtem. *Energy Fuels*. **2002**, *16*, 490-496.
- (18) Schuler, B.; Meyer, G.; Peña, D.; Mullins, O. C.; Gross, L. Unraveling the Molecular Structures of Asphaltenes by Atomic Force Microscopy. *J. Am. Chem. Soc.* **2015**, *137*, 9870-9876.
- (19) Chacón-Patiño, M. L.; Rowland, S. M.; Rodgers, R. P. Advances in Asphaltene Petroleomics. Part 1: Asphaltenes Are Composed of Abundant Island and Archipelago Structural Motifs. *Energy Fuels*. **2017**, *31*, 13509-13518.
- (20) Kaiser, N. K.; Savory, J. J.; McKenna, A. M.; Quinn, J. P.; Hendrickson, C. L.; Marshall, A. G. Electrically Compensated Fourier Transform Ion Cyclotron Resonance Cell for Complex Mixture Mass Analysis. *Anal. Chem.* **2011**, *83*, 6907-6910.
- (21) Mao, Y. Application of Ft-Icr Mass Spectrometry in Study of Proteomics, Petroleomics and Fragmentomics. **2016**.
- (22) McLafferty, F. W. Tandem Mass Spectrometry. *Science*. **1981**, *214*, 280-287.
- (23) Tang, W.; Hurt, M. R.; Sheng, H.; Riedeman, J. S.; Borton, D. J.; Slater, P.; Kenttämäa, H. I. Structural Comparison of Asphaltenes of Different Origins Using Multi-Stage Tandem Mass Spectrometry. *Energy Fuels*. **2015**, *29*, 1309-1314.
- (24) Hurt, M. R.; Borton, D. J.; Choi, H. J.; Kenttämäa, H. I. Comparison of the Structures of Molecules in Coal and Petroleum Asphaltenes by Using Mass Spectrometry. *Energy Fuels*. **2013**, *27*, 3653-3658.
- (25) Qian, K.; Edwards, K. E.; Mennito, A. S.; Freund, H.; Saeger, R. B.; Hickey, K. J.; Francisco, M. A.; Yung, C.; Chawla, B.; Wu, C. Determination of Structural Building Blocks in Heavy Petroleum Systems by Collision-Induced Dissociation Fourier Transform Ion Cyclotron Resonance Mass Spectrometry. *Anal. Chem.* **2012**, *84*, 4544-4551.
- (26) Wittrig, A. M.; Fredriksen, T. R.; Qian, K.; Clingenpeel, A. C.; Harper, M. R. Single Dalton Collision-Induced Dissociation for Petroleum Structure Characterization. *Energy Fuels*. **2017**.

- (27) Owen, B. C.; Gao, J.; Borton, D. J.; Amundson, L. M.; Archibold, E. F.; Tan, X.; Azyat, K.; Tykwinski, R.; Gray, M.; Kenttämä, H. I. Carbon Disulfide Reagent Allows the Characterization of Nonpolar Analytes by Atmospheric Pressure Chemical Ionization Mass Spectrometry. *Rapid Commun. Mass Spectrom.* **2011**, *25*, 1924-1928.
- (28) Olsen, J. V.; Macek, B.; Lange, O.; Makarov, A.; Horning, S.; Mann, M. Higher-Energy C-Trap Dissociation for Peptide Modification Analysis. *Nat. Methods.* **2007**, *4*, 709.
- (29) Niko, Y.; Kawauchi, S.; Otsu, S.; Tokumaru, K.; Konishi, G.-i. Fluorescence Enhancement of Pyrene Chromophores Induced by Alkyl Groups through Σ - Π Conjugation: Systematic Synthesis of Primary, Secondary, and Tertiary Alkylated Pyrenes at the 1, 3, 6, and 8 Positions and Their Photophysical Properties. *J. Org. Chem.* **2013**, *78*, 3196-3207.
- (30) Bailey, W. F.; Luderer, M. R.; Jordan, K. P. Effect of Solvent on the Lithium-Bromine Exchange of Aryl Bromides: Reactions of N-Butyllithium and Tert-Butyllithium with 1-Bromo-4-Tert-Butylbenzene at 0° C. *J. Org. Chem.* **2006**, *71*, 2825-2828.
- (31) Jarrell, T. M.; Jin, C.; Riedeman, J. S.; Owen, B. C.; Tan, X.; Scherer, A.; Tykwinski, R. R.; Gray, M. R.; Slater, P.; Kenttämä, H. I. Elucidation of Structural Information Achievable for Asphaltenes Via Collision-Activated Dissociation of Their Molecular Ions in Msn Experiments: A Model Compound Study. *Fuel.* **2014**, *133*, 106-114.
- (32) Nyadong, L.; Lai, J.; Thompsen, C.; LaFrancois, C. J.; Cai, X.; Song, C.; Wang, J.; Wang, W. High-Field Orbitrap Mass Spectrometry and Tandem Mass Spectrometry for Molecular Characterization of Asphaltenes. *Energy Fuels.* **2017**, *32*, 294-305.
- (33) Ha, J.; Cho, E.; Kim, S. Interpreting Chemical Structures of Compounds in Crude Oil Based on the Tandem Mass Spectra of Standard Compounds Obtained at the Same Normalized Collision Energy. *Energy Fuels.* **2017**, *31*, 6960-6967.
- (34) Wittrig, A. M.; Fredriksen, T. R.; Qian, K.; Clingenpeel, A. C.; Harper, M. R. Single Dalton Collision-Induced Dissociation for Petroleum Structure Characterization. *Energy Fuels.* **2017**, *31*, 13338-13344.
- (35) Schuler, B.; Meyer, G.; Peña, D.; Mullins, O. C.; Gross, L. Unraveling the Molecular Structures of Asphaltenes by Atomic Force Microscopy. *J. Am. Chem. Soc.* **2015**, *137*, 9870-9876.

CHAPTER 5. COMPARING ENERGY-RESOLVED MEDIUM-ENERGY COLLISION-ACTIVATED DISSOCIATION AND ENERGY-RESOLVED ION-TRAP COLLISION-ACTIVATED DISSOCIATION FOR DIFFERENTIATING AROMATIC ISOMERIC IONS

5.1 Introduction

CAD of isolated ions sometimes fails to differentiate them because it generates fragment ions with the same m/z values with similar abundances. In such challenging cases, ion-molecule reactions have been employed to successfully differentiate ionized isomers with different functionalities.¹ Alternatively, ion-mobility MS can be used to differentiate isomeric ions with significantly different shapes.² However, even with the help of these techniques, differentiating isomers with the same functionalities and similar shapes, such as isomers of small aromatic compounds still remains a major challenge.

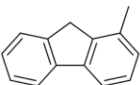
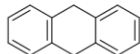
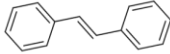
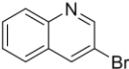
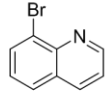
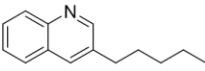
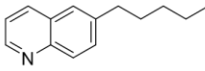
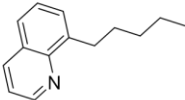
In this study, the use of energy-resolved CAD mass spectrometry (ERMS CAD) was explored to address the challenging situation of distinguishing isomers of small aromatic compounds. ERMS CAD is a relatively old technique originally developed to study the energetics of ion fragmentation processes.³⁻⁵ ERMS CAD involves measuring a series of mass spectra at different collision energies.⁶

Traditionally, ERMS ITCAD has been employed to differentiate isomers where conventional ITCAD methods have failed.⁷⁻¹⁰ However, studies on using ERMS MCAD for differentiating ionized isomers, particularly isomers of small organic molecules, are scarce. Compared to ITCAD, MCAD does not suffer from low-mass cutoff,¹¹ meaning that during ITCAD, the ion trap cannot store fragment ions with m/z -values lower than ~30% of the m/z -value of the fragmenting ions.¹² In addition, MCAD can cause fragmentation of the fragment ions without additional isolation/fragmentation steps.¹³ Furthermore, earlier investigations of biological molecules have provided many insights into the mechanisms of ITCAD and MCAD.^{14,15} One of the major differences between the two is that the fragment ions can be further fragmented in MCAD but not in ITCAD.

In this study, ERMS MCAD was compared to ERMS ITCAD for differentiating four sets of isomeric aromatic molecular ions (Table 5.1).

The isomeric aromatic compounds were ionized with APCI in the positive ion mode. CS₂ was used as the solvent and ionization reagent to generate stable molecular ions from the analytes.¹⁶ All experiments were performed in the linear quadrupole ion trap/orbitrap high-resolution mass spectrometer described above.

Table 5.1 Names and structures of the four isomeric sets of compounds studied.

Isomer Set	Name	Structure	Name	Structure
1	1-Methylfluorene		9,10-Dihydroanthracene	
2	9,10-Dihydrophenanthrene		<i>Trans</i> -stilbene	
3	3-Bromoquinoline		8-Bromoquinoline	
4	3-Pentylquinoline		6-Pentylquinoline	
4	8-Pentylquinoline			

5.2 Materials and Methods

1-Methylfluorene (purity $\geq 98\%$), 9,10-dihydroanthracene (purity $\geq 97\%$), 9,10-dihydrophenanthrene (purity $\geq 94\%$), and *trans*-stilbene (purity $\geq 96\%$) were purchased from Sigma-Aldrich and used as received. 1,6-Hexylpyrene and 3-, 6-, and 8-pentylquinolines were synthesized in-house via Negishi coupling by Mr. Yuyang Zhang.¹⁷ The compounds were dissolved in carbon disulfide (purity $\geq 99\%$, purchased from Alfa Aesar) to form solutions with a concentration of 1 mg/mL unless otherwise stated. These solutions were introduced into a Thermo LTQ-Orbitrap XL mass spectrometer via direct infusion at a flow rate of 10 μ L/min.

The compounds were ionized using positive-ion mode APCI with carbon disulfide as the ionization reagent to form stable molecular ions.¹⁸ The ions were transferred into the linear quadrupole ion trap and isolated with an isolation window of 1 m/z. The ions were then subjected to ITCAD using the He buffer gas as the target gas at varying collision energies. The collision energy for the isomer set 1 and 2 in Table 5.1 was increased from 0 up to 70 (arbitrary units) at increments of 10. The collision energy for the isomer set 3 and 4 in Table 5.1 was increased from 0 up to 100 (arbitrary units) at increments of 10. Then the ions were then transferred to the orbitrap via the C trap and were detected at a mass resolution of 100,000.

For MCAD, the ions were isolated in the linear quadrupole ion trap as described above and then transferred into the octopole collision cell. For isomer set 1 and 2 in Table 5.1, the collision energy was increased from 0 up to 36 eV at increments of ~ 3.6 eV. For isomer set 3 and 4 in Table 5.1, the collision energy was increased from 0 up to 40 eV at increments of ~ 4 eV. Then the ions were transferred to the orbitrap via the C trap and were detected at a mass resolution of 100,000.

5.3 Results and Discussion

5.3.1 ERMS ITCAD and ERMS MCAD of the Molecular Ions of 1,6-Hexylpyrene

ITCAD mass spectra of the molecular ions of 1,6-hexylpyrene (m/z 370) measured at collision energies of 30, 60, and 100 (arbitrary units) are shown in Figures 5.1a, 5.1b, and 5.1c, respectively. ITCAD of the fragmenting ions (m/z 370) at a collision energy of 30 resulted in the loss of one pentyl radical via a homolytic bond cleavage and produced fragment ions of m/z 299. As the collision energy was increased from 30 to 100, there were no observable changes in fragmentation (Figures 5.1b and 5.1c), suggesting that the fragment ions do not fragment further during ITCAD. This is because only the fragmenting ions are accelerated during ITCAD. Therefore, increasing the collision energy does not cause fragmentation of the fragment ions.

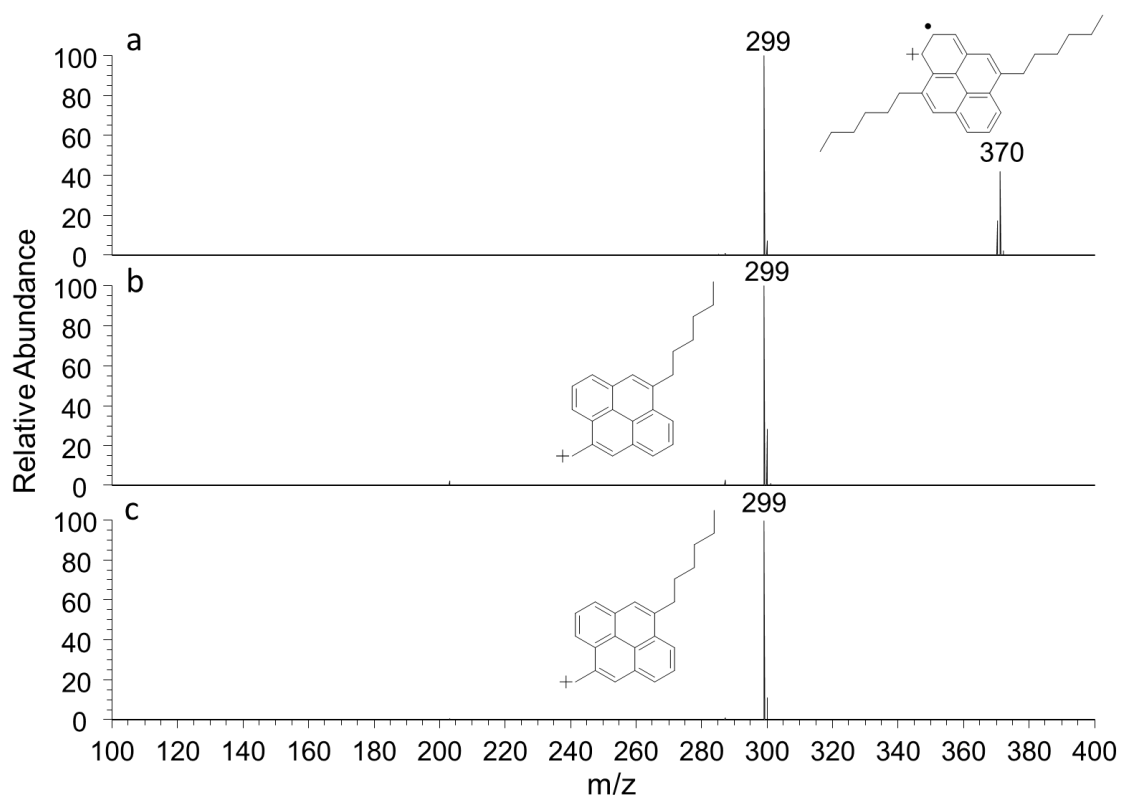


Figure 5.1. ITCAD spectra measured for the molecular ions of 1,6-hexylpyrene (MW 370 Da) at collision energies of (a) 30, (b) 60 and (c) 100 (arbitrary units).

MCAD of the molecular ions of 1,6-hexylpyrene (m/z 370) showed different fragmentation patterns compared to ITCAD (Figures 5.2a, 5.2b and 5.2c). MCAD at a collision energy of 22 eV resulted in the loss of one pentyl radical via homolytic cleavage and produced fragment ions with m/z 299 (Figure 5.2a), just like for ITCAD. However, unlike for ITCAD, MCAD at a collision energy of 44 eV resulted in one as well as two pentyl radical losses (m/z 299 and m/z 228; Figure 5.2b). As the MCAD collision energy was further increased to 74 eV, complete elimination of two pentyl radicals was observed (Figure 5.2c). These observations suggested that MCAD can cause fragmentation to the fragment ions.

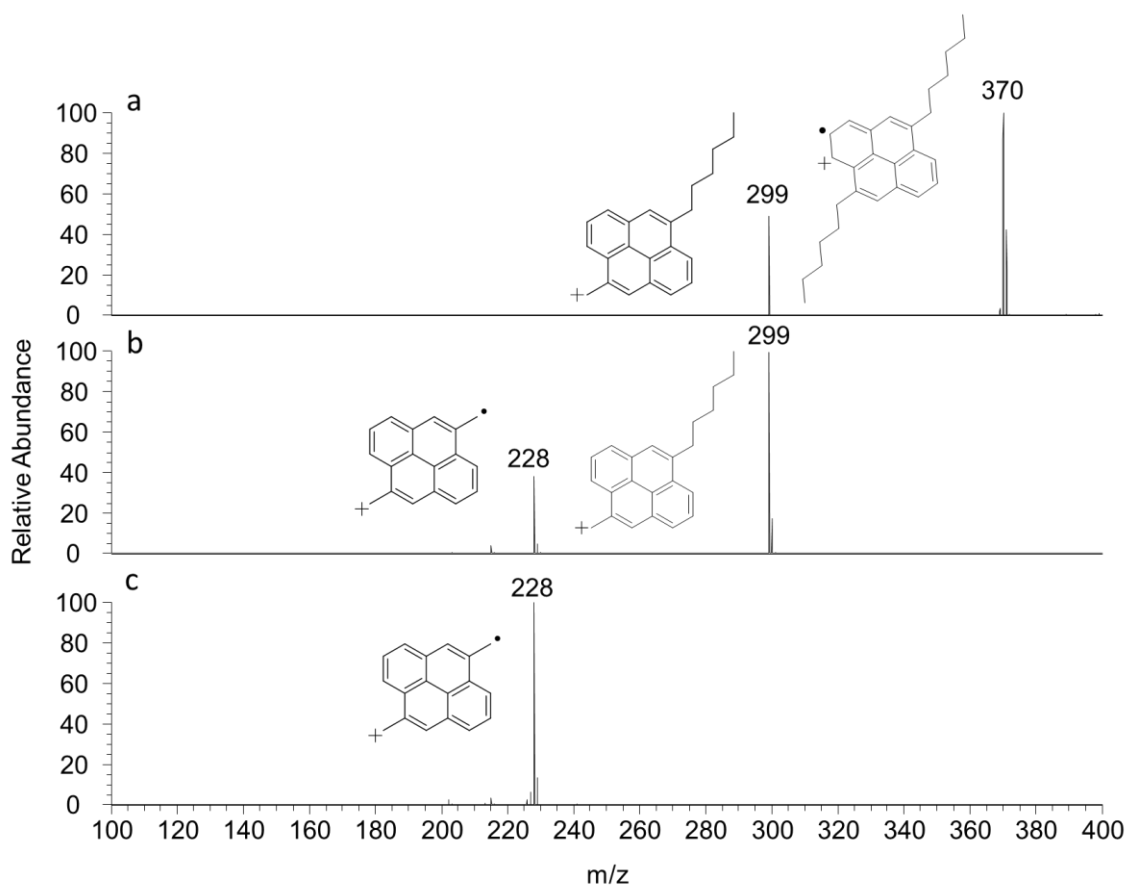


Figure 5.2. MCAD mass spectrum measured for the molecular ions of 1,6-hexylpyrene (MW 370 Da) at a collision energy of (a) 22 eV, (b) 44 eV, and (c) 74 eV.

5.3.2 ERMS ITCAD and ERMS MCAD of the Molecular Ions of 1-Methylfluorene and 9,10-Dihydroanthracene

ERMS ITCAD mass spectra of the isomeric molecular ions of 1-methylfluorene and 9,10-dihydroanthracene (m/z 180) are shown in Figures 5.3a and 5.3b, respectively. ITCAD of 1-methylfluorene molecular ions at collision energies greater than 20 resulted in the loss of methyl radical to generate fragment ions of m/z 165. ITCAD of 9,10-dihydroanthracene molecular ions at collision energies greater than 40 also resulted in the loss of a methyl radical to generate fragment ions of m/z 165. Proposed structures of ions of m/z 165 are shown in Figures 5.3a and 5.3b. Overall, the ERMS ITCAD mass spectra shown in Figures 5.3a and 5.3b are too similar to reliably differentiate the two isomers.

Unlike ERMS ITCAD, ERMS MCAD generated mass spectra for the molecular ions of 1-methylfluorene and 9,10-dihydroanthracene (Figure 5.3c and 5.3d) that are significantly different from each other. MCAD of ionized 1-methylfluorene (m/z 180) resulted in major fragment ions of m/z 165 as a result of methyl radical loss. Minor fragment ions of m/z 179 and m/z 178 (with relative abundances less than 10%) were also generated at collision energy ~ 15 eV and above; these ions correspond to one and two hydrogen atom losses, respectively. The loss of hydrogen atoms suggests that higher energy fragmentations can occur upon MCAD than ITCAD. On the other hand, ERMS MCAD mass spectra of ionized 9,10-dihydroanthracene (m/z 180) showed major fragment ions of m/z 179 at collision energies greater than 30 eV. These fragment ions are generated through hydrogen atom loss. Fragment ions of m/z 165 were formed via loss of a methyl radical.

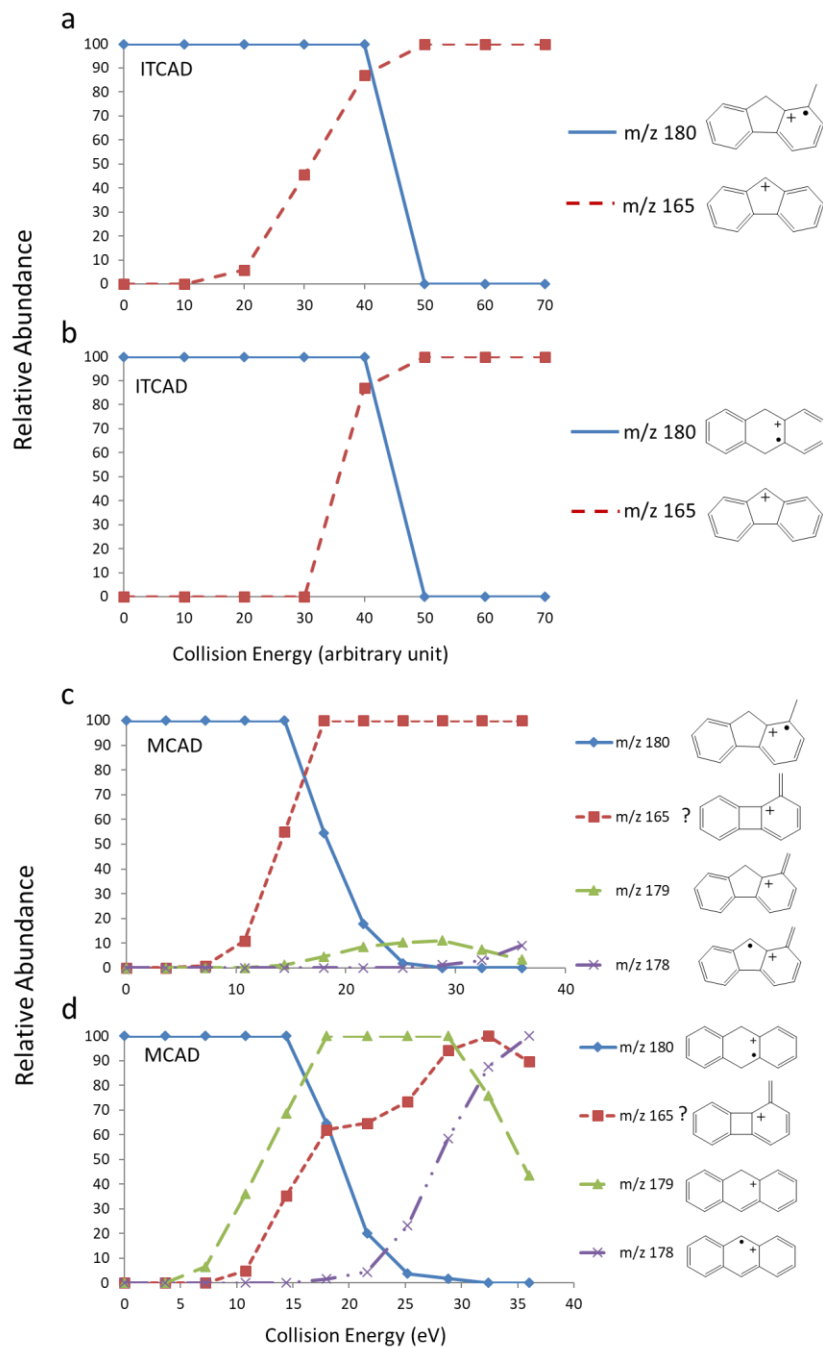


Figure 5.3 ERMS ITCAD mass spectra of the isomeric molecular ions of (a) 1-methylfluorene and (b) 9,10-dihydroanthracene (m/z 180). ERMS MCAD mass spectra of the molecular ions of (c) 1-methylfluorene and (d) 9,10-dihydroanthracene (m/z 180).

5.3.3 ERMS ITCAD and ERMS MCAD of the Molecular Ions of 9,10-Dihydrophenanthrene and *Trans*-Stilbene

ERMS ITCAD mass spectra of the molecular ions of 9,10-dihydrophenanthrene and *trans*-stilbene are shown in Figures 5.4a and 5.4b, respectively. ITCAD of both ions produced exclusively fragment ions of m/z 165 via loss of a methyl radical with similar relative abundances at different collision energies. Although the detailed mechanism for formation of these ions requires additional investigation, we hypothesize that the loss of a methyl radical in both cases involves a These two isomers cannot be differentiated by using ERMS ITCAD.

Significant differences were observed between ERMS MCAD mass spectra of the molecular ions of 9,10-dihydrophenanthrene and *trans*-stilbene (Figures 5.4c and 5.4d). MCAD of the molecular ions of 9,10-dihydrophenanthrene generated fragment ions of m/z 165, 179 and 178 through the loss of a methyl radical, one hydrogen atom, and two hydrogen atoms, respectively (Figure 5.4c). Loss of the methyl radical likely involves rearrangement while the loss of one and two hydrogen atoms likely occurs via simple bond cleavages. MCAD of the molecular ions of *trans*-stilbene generated all the same fragment ions and an additional one, that of m/z 102 via elimination of a benzene radical (Figure 5.4d). The loss of the benzene radical likely occurs via homolytic bond cleavage that is favored in MCAD but not in ITCAD. This difference can be used to differentiate the isomers.

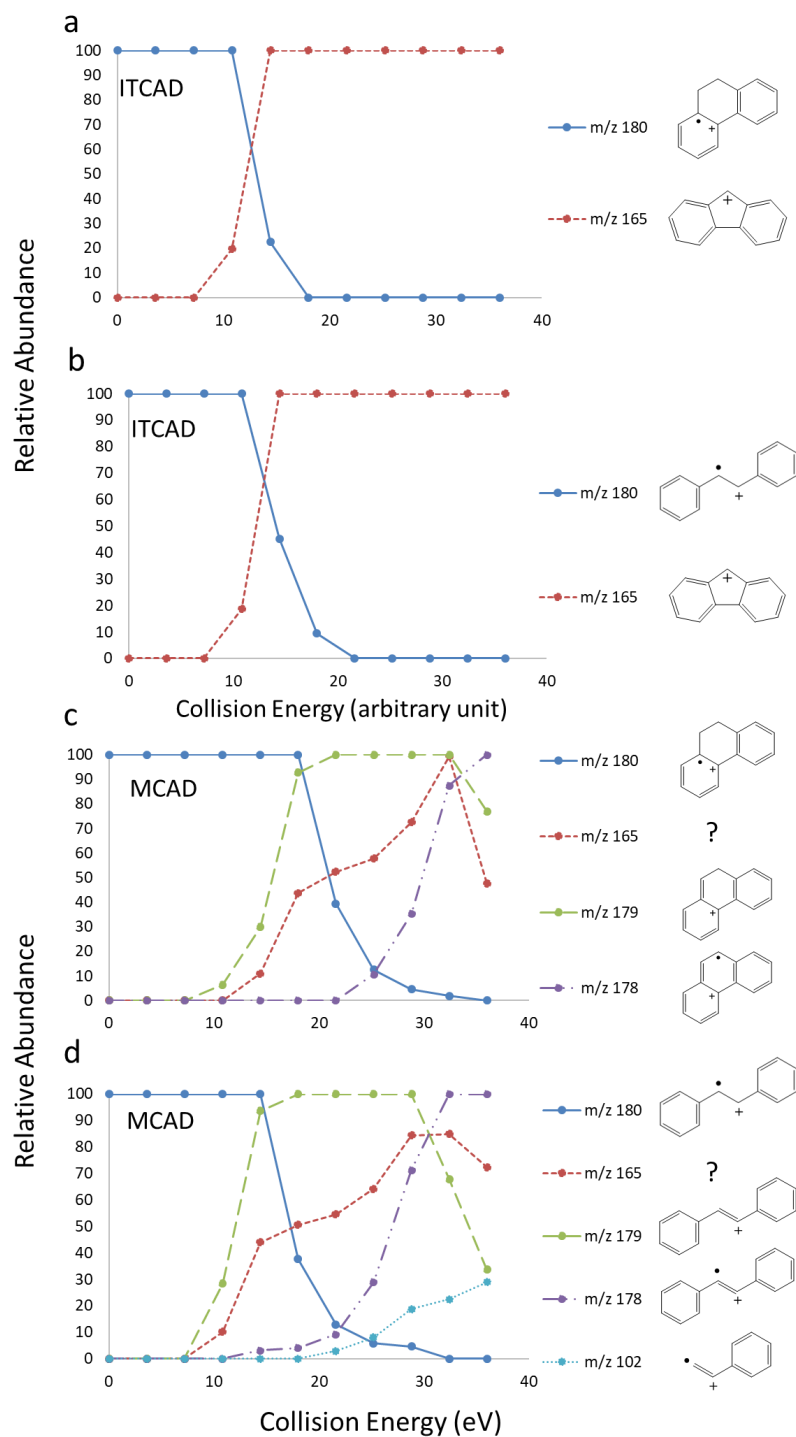


Figure 5.4 ERMS ITCAD mass spectra of the molecular ions of (a) 9,10-dihydrophenanthrene and (b) *trans*-stilbene. The ERMS MCAD mass spectra of the molecular ions of (c) 9,10-dihydrophenanthrene and (d) *trans*-stilbene.

Two fragment ions (Figures 5.5a and 5.5b, m/z 180 and 165) in the ERMS ITCAD mass spectra can be used to differentiate these isomeric ions based on their slight differences in the relative abundances measured at different collision energies. (. On the other hand, four fragment ions (Figures 5.5c and 5.5d m/z 180, 165, 179, 178) in the ERMS MCAD mass spectra can be used to differentiate the analytes based on their slight differences in the relative abundances measured at different collision energies. Overall, differentiation of the molecular ions of 9,10-dihydroanthracene and 9,10-dihydrophenanthrene is easier using ERMS MCAD compared to ERMS ITCAD.

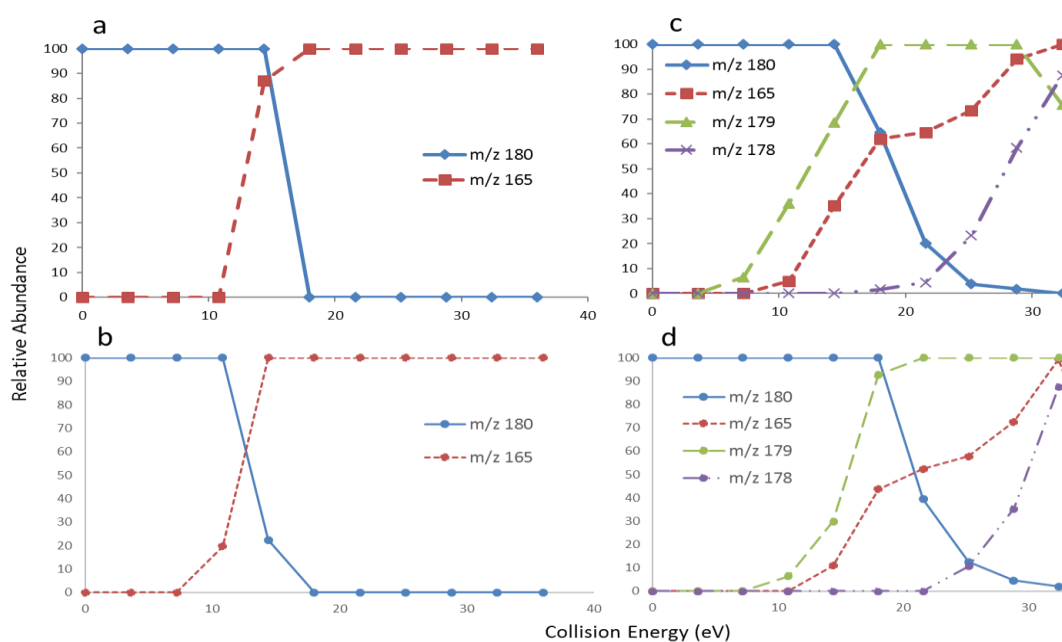


Figure 5.5 ERMS ITCAD mass spectra of the isomeric molecular ions of (a) 9,10-dihydroanthracene and (b) 9,10-dihydrophenanthrene (m/z 180). ERMS MCAD mass spectra of the molecular ions of (c) 9,10-dihydroanthracene and (d) 9,10-dihydrophenanthrene.

5.3.4 ERMS ITCAD and ERMS MCAD of the Molecular Ions of 3-, 6- and 8-Pentylquinolines

The potential of ERMS MCAD was explored in a particularly challenging scenario: differentiating the molecular ions of 3-, 6-, and 8-pentylquinolines. Figure 5.5 shows the ERMS ITCAD and ERMS MCAD mass spectra of the molecular ions of 3-, 6-, and 8-pentylquinolines. ITCAD of 3-, 6- and 8-pentylquinolines only generates fragment ions of m/z 142 through butyl radical loss (Figures 5.6d, 5.6e and 5.6f). Although slight differences in the relative abundances of the ions of m/z 142 were observed in the ERMS ITCAD mass spectra, such differences are insignificant and thus cannot be used to differentiate the three isomers.

MCAD of these molecular ions produced fragment ions of m/z 198, 184, 170, 156, 142, 129, and 115 (Figures 5.6d, 5.6e and 5.6f). These fragment ions showed significant differences in their relative abundances that can be used to differentiate these molecular ions. Fragment ions of m/z 198 were generated via the loss of a hydrogen atom. Fragment ions of m/z 184, 170, 156, 142 and 130 were generated via the loss of a methyl, ethyl, propyl, butyl, or pentyl radical, respectively. Fragment ions of m/z 115 were generated via the loss of a neutral HCN group. Overall, the molecular ions of 3-pentylquinolines can be differentiated from the other based on the ions of m/z 115 with the highest relative abundance observed at a MCAD collision energy larger than 35 eV. The molecular ions of 8-pentylquinoline can be differentiated based on the ions of m/z 156 with the highest relative abundances at a MCAD collision energy larger than 15 eV.

To illustrate the significant differences between the MCAD mass spectra of the molecular ions of pentylquinoline isomers, their MCAD mass spectra obtained at collision energies of 28 eV and 40 eV are shown in Figures 5.7 and 5.8, respectively. Upon MCAD at a collision energy of 28 eV, ions of m/z 156 is the most abundant fragment ions for molecular ions of 8-pentylquinoline (Figure 5.7a) while ions of m/z 156 are much less abundant for molecular ions of 3- and 6-pentylquinolines (Figure 5.7b and 5.7c). Upon MCAD at a collision energy of 40 eV, ions of m/z 115 is the most abundant fragment ions for molecular ions of 3-pentylquinoline (Figure 5.8a) while ions of m/z 115 are less abundant for the others (Figure 5.8b and 5.8c).

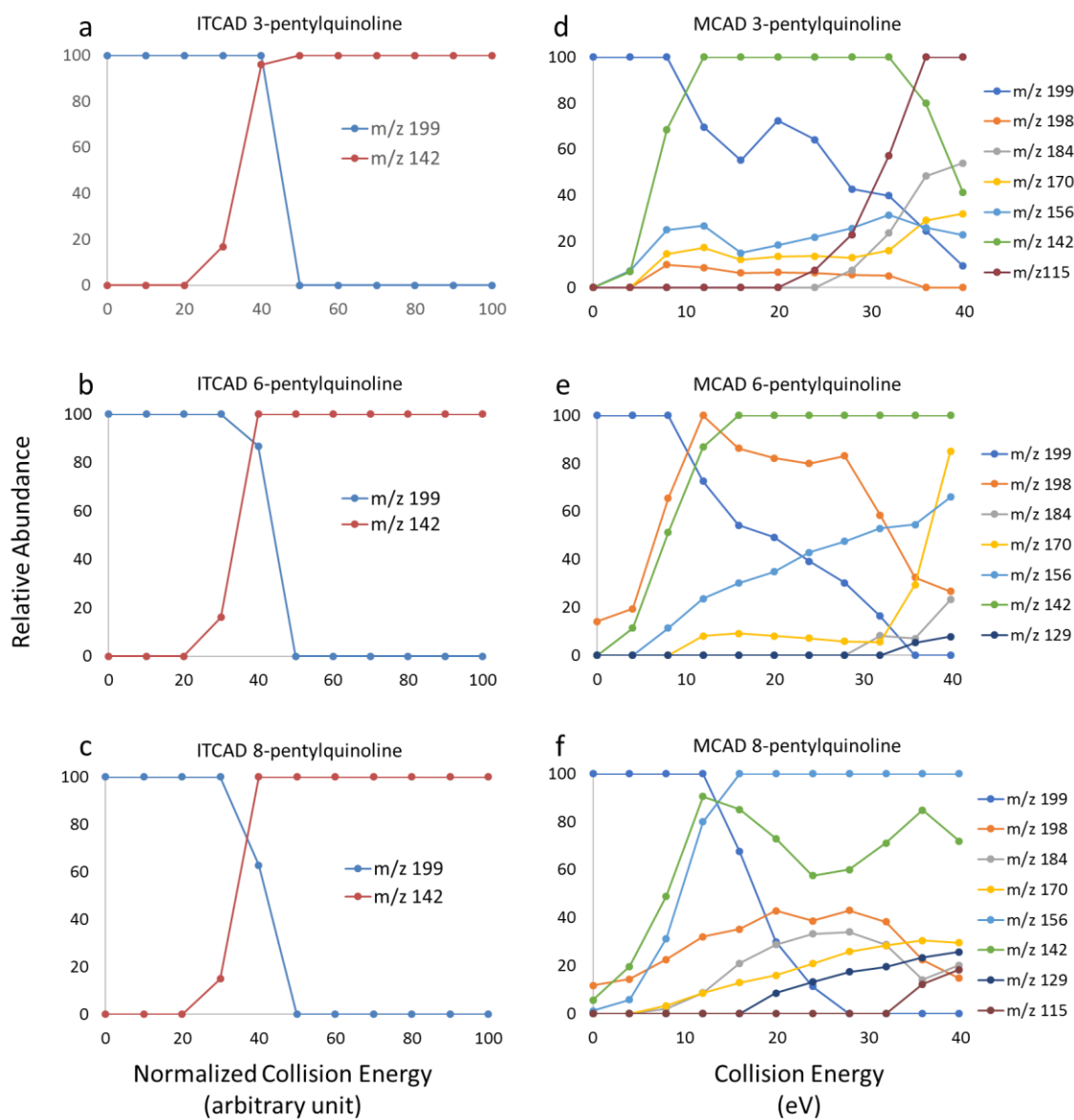


Figure 5.6 ERMS ITCAD mass spectra of the molecular ions of (a) 3-pentylquinoline, (b) 6-pentylquinoline, and (c) 8-pentylquinoline. ERMS MCAD mass spectra of the molecular ions of (d) 3-pentylquinoline, (e) 6-pentylquinoline, and (f) 8-pentylquinoline.

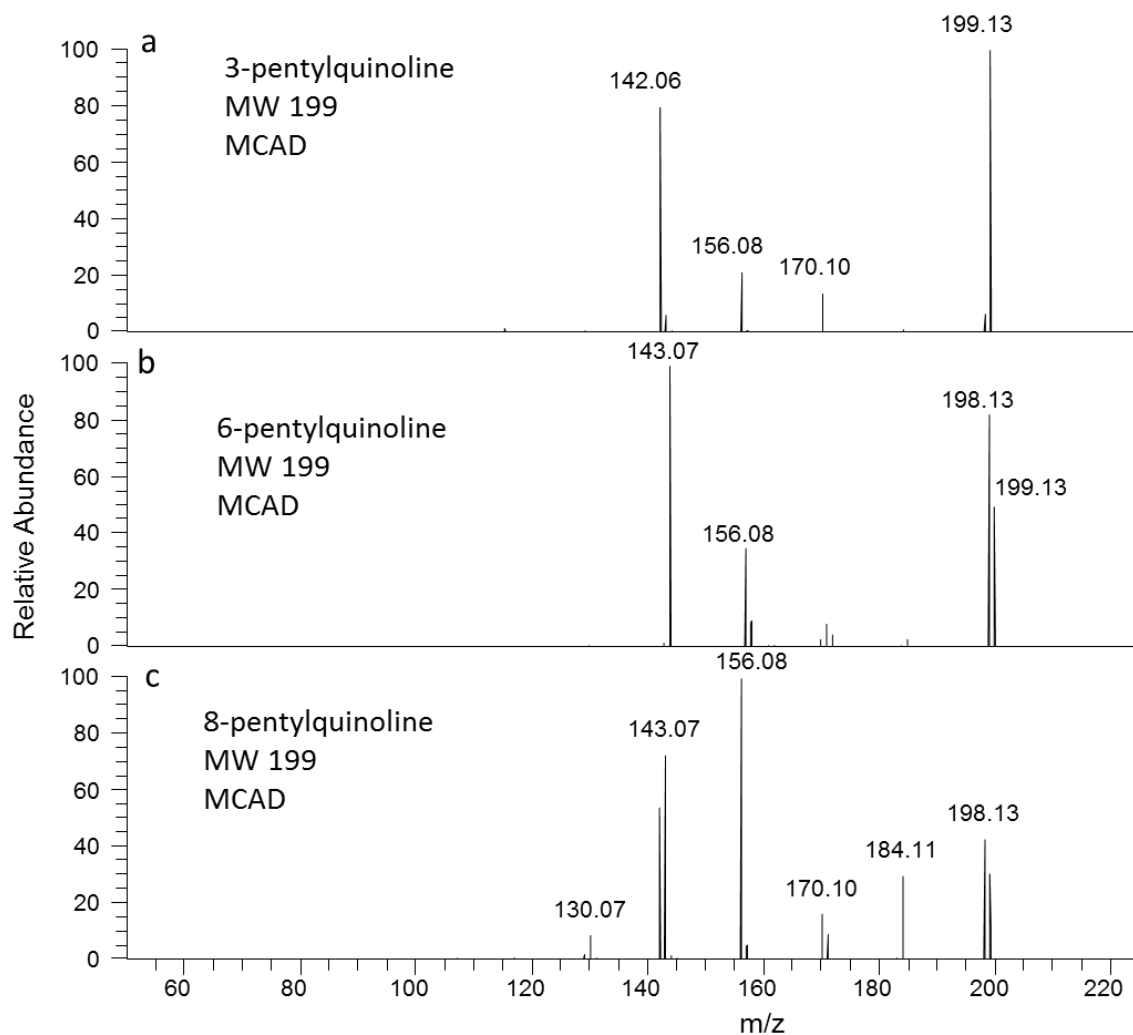


Figure 5.7 MCAD MS/MS spectra of the molecular ions of (a) 8-pentylquinoline, (b) 6-pentylquinoline, and (c) 3-pentylquinoline at a normalized collision energy of 28 eV.

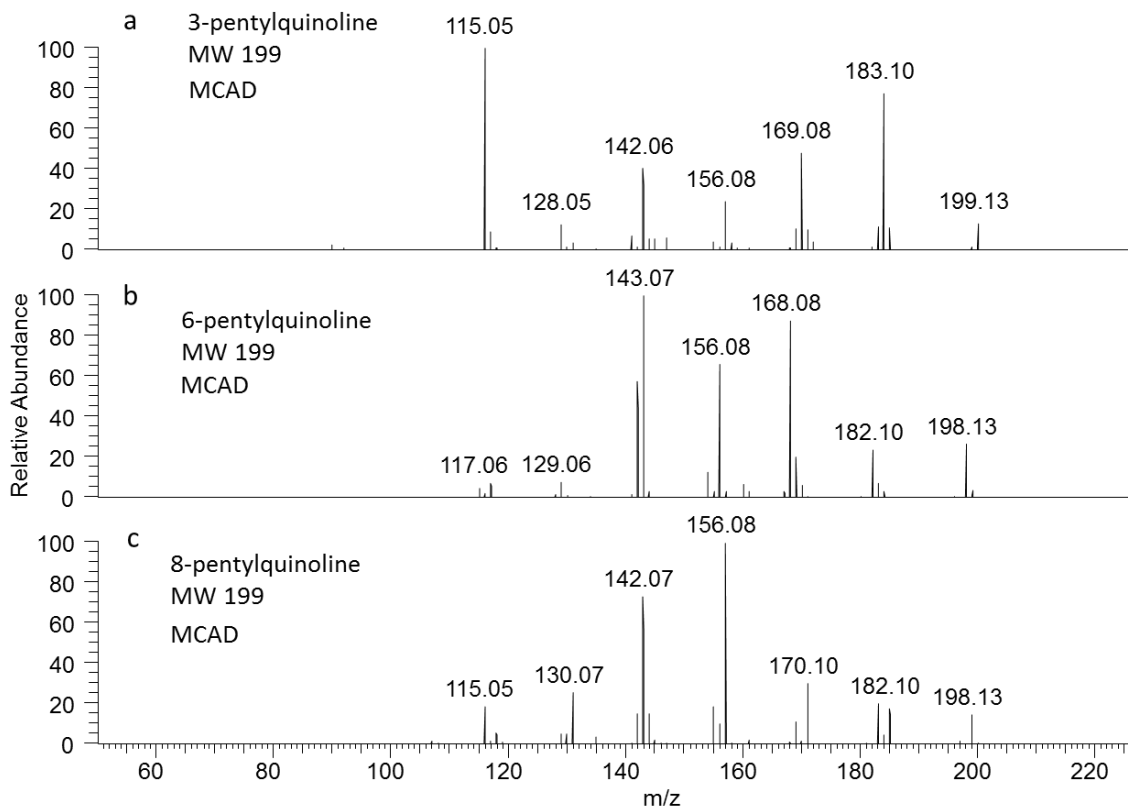


Figure 5.8 MCAD MS/MS spectra of the molecular ions of (a) 8-pentylquinoline, (b) 6-pentylquinoline, and (c) 3-pentylquinoline at a collision energy of 40 eV.

The possible fragmentation pathways of above isomeric ions are shown in Figure 5.9. These fragmentation pathways may be used to rationalize the major differences in the relative abundances of fragment ions of m/z 115 and 156 in the ERMS MCAD mass spectra of the molecular ions of 3-, 6- and 8-pentylquinolines. As discussed above, a high relative abundance of fragment ions of m/z 115 is unique to 3-pentylquinoline at MCAD collision energy larger than 35 eV. A high relative abundance of fragment ions of m/z 156 is unique to 8-pentylquinoline at high MCAD collision energy larger than 15 eV.

The fragment ion of m/z 115 is the dominant fragment ion in the ERMS MCAD mass spectrum of the molecular ions of 3-pentylquinoline (m/z 199) at collision energies greater than 35 eV. However, this fragment ion is absent for the molecular ions of 6-pentylquinoline (Figures 5.6e) and has low abundance in the MCAD mass spectrum measured for the molecular ions of 8-pentylquinoline (Figure 5.6f). The fragment ions of m/z 115 are generated upon elimination of a neutral HCN group from methylquinoline ions of m/z 142 (Figure 5.9, highlighted by red box). Fragmentation of the molecular ions of 3-methylquinoline ions is hypothesized to generate a stable ion, possibly inden-1-ylum. (ion of m/z 115, Figure 5.9a, highlighted in red box)). Meanwhile, fragmentations of the molecular ions of the 6- and 8-methylquinolines likely generated relatively unstable ions, possibly with four-ring structures (ion of m/z 115, Figure 5.9b and 5.9c, highlighted in red box).

Abundant fragment ions of m/z 156 are formed upon ERMS MCAD of the molecular ions of 8-pentylquinoline (m/z 199) but they are less abundant for the molecular ions of 3- and 6-pentylquinolines. The fragment ions of m/z 156 are generated upon elimination of a propyl radical from the molecular ions of m/z 199 (Figure 5.9, highlighted by blue box). Fragmentation of molecular ions of 3- and 6-pentylquinolines generate the fragment ions of m/z 156 that are hypothesized to have unstable four-ring structure (Figure 5.9a and 5.9b) In contrast, for the molecular ions of 8-pentylquinoline, the fragment ions of m/z 156 (Figure 5.9c) might have a stable five-ring structure. Consequently, energy resolved MCAD produced fragment ions of m/z 156 with high abundance for the molecular ions of 8-pentylquinoline but not for those of 3- and 6-pentylquinoline.

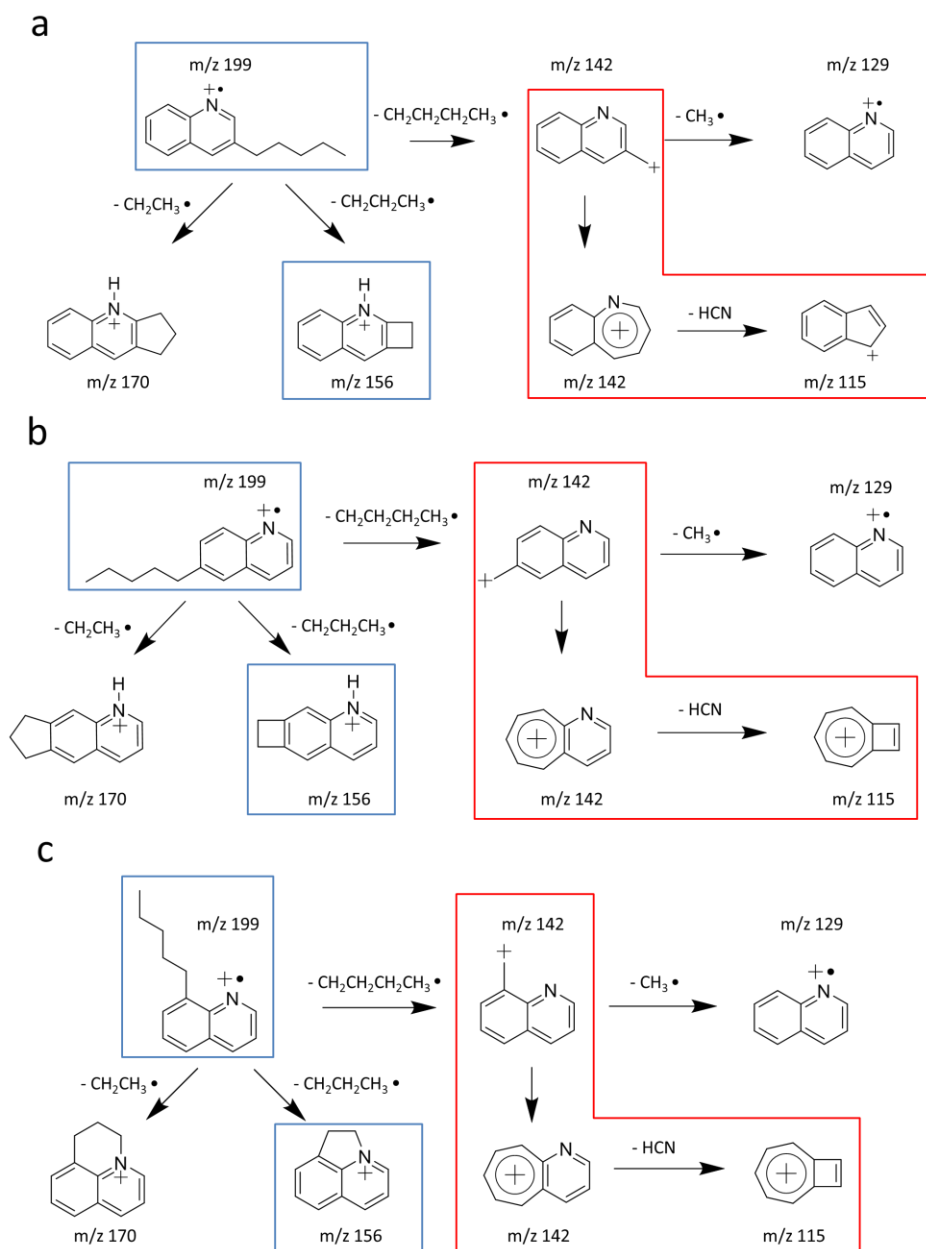


Figure 5.9 Proposed fragmentation pathways for MCAD of the molecular ions of a) 3-pentylquinoline, (b) 6-pentylquinoline, and (c) 8-pentylquinoline.

5.3.5 Comparison of Ion Loss for ERMS MCAD and ERMS ITCAD

Ion loss during CAD is rarely a concern when analyzing pure compounds. However, ion loss significantly affects the signal-to-noise ratio of CAD tandem mass spectra when analyzing complex mixtures. In this section, ion loss during ERMS ITCAD and MCAD of the molecular ions of 1-methylfluorene and 9,10-dihydroanthracene was compared (Figure 5.10). During energy-resolved ITCAD, the total ion current (TIC) decreased by approximately two orders of magnitude for both ions (Figure 5.10a, 5.10b). In contrast, during ERMS MCAD, the TIC remained relatively the same (Figure 5.10c and 5.10d). Therefore, ERMS MCAD will have a better overall signal-to-noise ratio compared to ERMS ITCAD. Overall, the ions loss is significantly larger during ERMS ITCAD than ERMS MCAD.

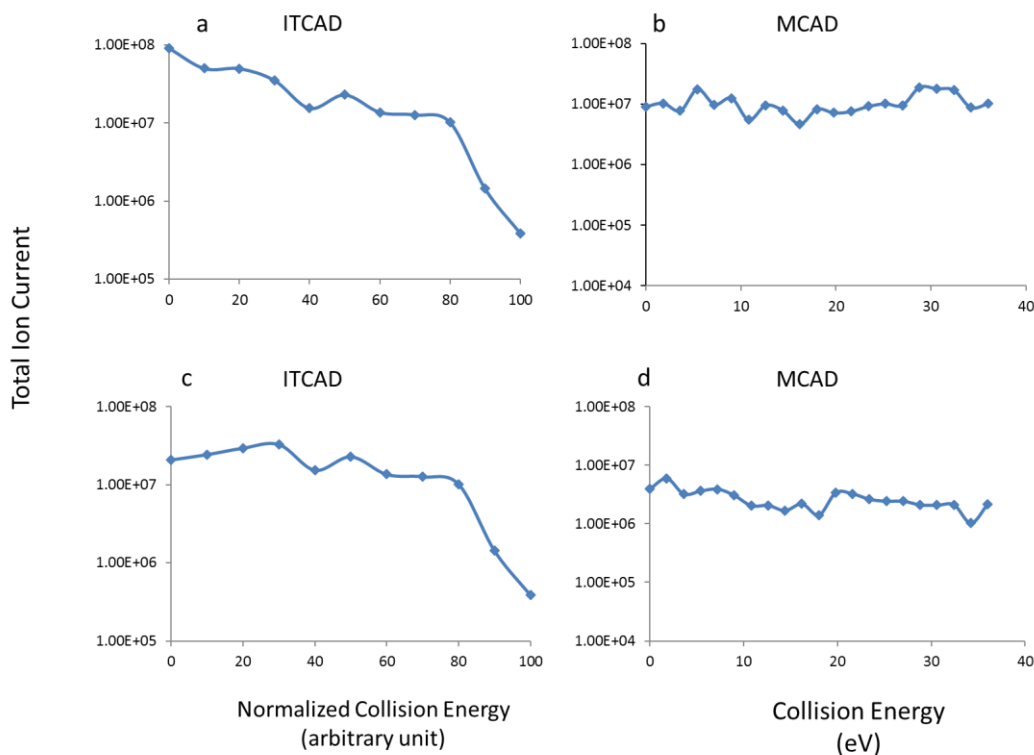


Figure 5.10 The total ion abundance versus the collision energy during ERMS ITCAD and ERMS MCAD. Ion loss during ITCAD-ERMS of molecular ions of (a) 1-methylfluorene, (c) 9,10-dihydroanthracene. Ion loss during ERMS MCAD of molecular ions of (b) 1-methylfluorene, (d) 9,10-dihydroanthracene.

5.4 Conclusions

In this work, the ability of ERMS ITCAD and ERMS MCAD to differentiate between small ionized aromatic isomers was compared. Overall, ERMS ITCAD only generated fragment ions via low-energy fragmentation pathways and could not reliably differentiate the isomers studied here. ERMS MCAD generated fragment ions via both low- and high-energy fragmentation pathways. Some of the fragment ions with unique m/z values or greatly differing abundances generated via high-energy pathways can be used to reliably differentiate the isomeric ions.

In addition, MCAD also suffers from less ion loss at high collision energies compared to ITCAD. This could benefit the analysis of complex mixtures, where the ion abundance is low. Overall, ERMS MCAD MS holds several possible advantages in MS/MS analysis of complex mixtures containing isomeric compounds compared to conventional ERMS ITCAD MS.

5.5 References

- (1) Sheng, H.; Tang, W.; Yerabolu, R.; Max, J.; Kotha, R. R.; Riedeman, J. S.; Nash, J. J.; Zhang, M.; Kenttämä, H. I. Identification of N-Oxide and Sulfoxide Functionalities in Protonated Drug Metabolites by Using Ion–Molecule Reactions Followed by Collisionally Activated Dissociation in a Linear Quadrupole Ion Trap Mass Spectrometer. *J. Org. Chem.* **2015**, *81*, 575-586.
- (2) Kanu, A. B.; Dwivedi, P.; Tam, M.; Matz, L.; Hill, H. H. Ion Mobility–Mass Spectrometry. *Int. J. Mass Spectrom.* **2008**, *43*, 1-22.
- (3) Fetterolf, D.; Yost, R.-A. Energy-Resolved Collision-Induced Dissociation in Tandem Mass Spectrometry. *Int. J. Mass Spectrom. Ion Physic.* **1982**, *44*, 37-50.
- (4) Herman, J. A.; Li, Y.-H.; Lin, M. S.; Harrison, A. G. Energy Dependence of the Fragmentation of the Molecular Ions of Some Branched C₇H₁₄ Olefins. *Int. J. Mass Spectrom. Ion Process.* **1985**, *66*, 75-91.
- (5) McLuckey, S.; Glish, G.; Cooks, R. Kinetic Energy Effects in Mass Spectrometry/Mass Spectrometry Using a Sector/Quadrupole Tandem Instrument. *Int. J. Mass Spectrom. Ion Physic.* **1981**, *39*, 219-230.
- (6) McLuckey, S.; Glish, G.; Cooks, R. Kinetic Energy Effects in Mass Spectrometry/Mass Spectrometry Using a Sector/Quadrupole Tandem Instrument. *Int. J. Mass Spectrom. Ion. Process.* **1981**, *39*, 219-230.
- (7) Menachery, S. P. M.; Laprévotte, O.; Nguyen, T. P.; Aravind, U. K.; Gopinathan, P.; Aravindakumar, C. T. Identification of Position Isomers by Energy-Resolved Mass Spectrometry. *Int. J. Mass Spectrom.* **2015**, *50*, 944-950.
- (8) Kurimoto, A.; Daikoku, S.; Kanie, O. In *Experimental Glycoscience*; Springer, 2008, pp 37-38.
- (9) Daikoku, S.; Ako, T.; Kurimoto, A.; Kanie, O. Anomeric Information Obtained from a Series of Synthetic Trisaccharides Using Energy Resolved Mass Spectra. *Int. J. Mass Spectrom.* **2007**, *42*, 714-723.
- (10) Kurimoto, A.; Daikoku, S.; Mutsuga, S.; Kanie, O. Analysis of Energy-Resolved Mass Spectra at Ms N in a Pursuit to Characterize Structural Isomers of Oligosaccharides. *Anal. Chem.* **2006**, *78*, 3461-3466.
- (11) Olsen, J. V.; Macek, B.; Lange, O.; Makarov, A.; Horning, S.; Mann, M. Higher-Energy C-Trap Dissociation for Peptide Modification Analysis. *Nat. Methods.* **2007**, *4*, 709.

- (12) Yang, Y.-H.; Lee, K.; Jang, K.-S.; Kim, Y.-G.; Park, S.-H.; Lee, C.-S.; Kim, B.-G. Low Mass Cutoff Evasion with Qz Value Optimization in Ion Trap. *Anal. Biochem.* **2009**, *387*, 133-135.
- (13) Nyadong, L.; Lai, J.; Thompsen, C.; LaFrancois, C. J.; Cai, X.; Song, C.; Wang, J.; Wang, W. High-Field Orbitrap Mass Spectrometry and Tandem Mass Spectrometry for Molecular Characterization of Asphaltenes. *Energy Fuels.* **2017**, *32*, 294-305.
- (14) Harrison, A. G. Energy-Resolved Mass Spectrometry: A Comparison of Quadrupole Cell and Cone-Voltage Collision-Induced Dissociation. *Rapid Commun. Mass Spectrom.* **1999**, *13*, 1663-1670.
- (15) Schuhmann, K.; Herzog, R.; Schwudke, D.; Metelmann-Strupat, W.; Bornstein, S. R.; Shevchenko, A. Bottom-up Shotgun Lipidomics by Higher Energy Collisional Dissociation on Ltq Orbitrap Mass Spectrometers. *Anal. Chem.* **2011**, *83*, 5480-5487.
- (16) Owen, B. C.; Gao, J.; Borton, D. J.; Amundson, L. M.; Archibold, E. F.; Tan, X.; Azyat, K.; Tykwinski, R.; Gray, M.; Kenttämaa, H. I. Carbon Disulfide Reagent Allows the Characterization of Nonpolar Analytes by Atmospheric Pressure Chemical Ionization Mass Spectrometry. *Rapid Commun. Mass Spectrom.* **2011**, *25*, 1924-1928.
- (17) Baba, S.; Negishi, E. A Novel Stereospecific Alkenyl-Alkenyl Cross-Coupling by a Palladium-or Nickel-Catalyzed Reaction of Alkenylalanes with Alkenyl Halides. *J. Am. Chem. Soc.* **1976**, *98*, 6729-6731.
- (18) Owen, B. C.; Gao, J.; Borton, D. J.; Amundson, L. M.; Archibold, E. F.; Tan, X.; Azyat, K.; Tykwinski, R.; Gray, M.; Kenttämaa, H. I. Carbon Disulfide Reagent Allows the Characterization of Nonpolar Analytes by Atmospheric Pressure Chemical Ionization Mass Spectrometry. *Rapid Commun. Mass Spectrom.* **2011**, *25*, 1924-1928.

PUBLICATIONS

1. Ravikiran Yerabolu, Raghavendhar R. Kotha, Edouard Niyonsaba, **Xueming Dong**, Jeremy M. Manheim, John Kong, James S. Riedeman, Mark Romanczyk, Cliff T. Johnston, Gozdem Kilaz, Hilikka I. Kenttämäa,* Molecular profiling of crude oil by using Distillation Precipitation Fractionation Mass Spectrometry (DPF-MS), *Fuel* **2018**, 234, 492-501.
2. Xing Fan, Guo-Sheng Li, **Xueming Dong**, Jing Jiang, Xian-Yong Wei, Hilikka I. Kenttämäa,* Tandem mass spectrometric evaluation of core structures of aromatic compounds after catalytic deoxygenation, *Fuel Process. Technol.* **2018**, 176, 119-123.